WAVE MANAGEMENT IN 1D AND 2D GRANULAR SYSTEMS: DESIGNS FOR STRESS WAVE MITIGATION AND CONTROL

BY

ROBERT FRANK WAYMEL

DISSERTATION

Submitted in partial fulfillment of the requirements
for the degree of Doctor of Philosophy in Aerospace Engineering
in the Graduate College of the
University of Illinois at Urbana-Champaign, 2017

Urbana, Illinois

Doctoral Committee:

Professor John Lambros, Chair
Professor Philippe Geubelle
Professor Emeritus Daniel Tortorelli
Professor Ioannis Chasiotis

ABSTRACT

Controlling stress waves during impact beyond merely dissipating their energy through material fracture, fragmentation, yielding etc., has been a significant focus of research in recent years. Materials exhibiting stress wave control characteristics would enable novel applications, such as for example stress wave focusing, deflection, annihilation, etc. that otherwise may not be present. Ordered granular media are one material group that has shown promise in this respect as they have been shown, at least in the elastic range, to possess very different wave propagation properties than continuous solids, such as the ability to sustain solitary waves – constant width and shape but variable speed waves. This dissertation investigates several granular systems, based on metallic spherical granules, that have been designed specifically to study certain aspects of wave propagation management. The first portion of this work investigates manipulating wave propagation in 1D granular chains. One design is easily altered between two configurations by a slight tilt in a gravitational field, and acts as a switch for wave propagation with peak amplitude on the order 10s of N: in one configuration, a solitary wave passes through unaltered, while in the other configuration, the travelling wave is significantly attenuated. A second design acts as a low pass force filter for high amplitude solitary waves (10s of kN) which is achieved through the use of preconditioned contacts – a process in which the granule contacts are loaded (beyond yield) to some peak force prior to use such that no further plasticity will occur in situ if the peak amplitude of the propagating wave is less than the peak preconditioning load.

The second portion of this work investigates elasto-plastic wave propagation in 2D granular square and hexagonal packings. The input wave experiences significant dissipation within as few as five contacts due to plastic dissipation at the granule contacts. The wave propagation patterns are determined to be similar to their elastic counterparts. The diameter tolerance is determined to be a primary source of scatter in the data.

The final part of this dissertation suggests designs to tailor the wave propagation within a granular packing. A numerical optimization scheme is utilized to determine the placement of cylindrical intruders at select interstitial locations within a square packing to accomplish momentum or force maximizations/minimizations at certain regions in the packing. The numerical and experimental results are similar with respect to the wave arrival time and peak forces experienced at certain locations within the packing. Several configurations demonstrate the ability to tailor the wave propagation in the granular packing through the use of interstitial cylinders, which laterally couple the square system. For some optimization scenarios, the numerical scheme does not outperform the baseline test cases. Thus, an iterative scheme is developed by forbidding intruders at certain locations, in effect changing the initial conditions of the optimization problem, and rerunning the optimization. The iterative scheme is shown to improve the results of the optimization.

A second method of tailoring elasto-plastic wave propagation is by preconditioning select contacts within a hexagonal packing. Depending on the orientation of the preconditioned contacts, the wave can be laterally deflected or allowed to pass through the packing with less attenuation. Interfacial packings, in which only a portion of the packing has preconditioned contacts, clearly illustrate the effect of the preconditioned contacts on the wave propagation behavior.

To my family, for their love and support.

ACKNOWLEDGEMENTS

I have had the pleasure of working with several collaborators throughout my time at Illinois. I greatly appreciate all the help from and camaraderie I enjoyed with my lab mates, Tommy and Erheng. I would also like to thank Raj, Amnaya, and Miguel for all of their efforts in producing the numerical simulations to enrich this work. Many thanks to the machine shop crew: Greg Milner, Lee Booher, and Steve Mathine. I appreciate the excellent craftsmanship and swift turnaround times as well as the occasional shop tour.

I thank the members of my committee for their time and the advice they have imparted. It has been rewarding to work alongside them in my various roles as student, MURI collaborator, and/or teaching assistant.

I am most grateful to John Lambros for superbly advising and encouraging me the past several years. I am deeply appreciative of the opportunity to work alongside an enthusiastic and decorated researcher and teacher and have learned a great deal from him. I have thoroughly enjoyed his friendship and mentorship over the years.

I would like to thank the Army Research Lab for hosting me for a summer and Oak Ridge Associated Universities for sponsoring me while I was there. I appreciate the time Todd Bjerke dedicated to showing me the various facilities and for guiding me throughout the summer. I would like to thank the researchers that made my work there possible: Jermaine Bradley, Dan Casem, Michael Zellner, and Christopher Meredith.

Finally, I would like to thank the US Army Research Office which generously funded this work through a MURI grant (W911NF-09-1-0436) and the Aerospace Department at UIUC for their support.

TABLE OF CONTENTS

1. INTRODUCTION

A granular medium is a collection of distinct macroscopic (i.e., kinetic motion is unaffected by thermal fluctuations) granules and has many properties that distinguish it from a continuous medium [1]. In fact, the behavior of granular media is sufficiently distinct from a continuous solid or a liquid that Jaeger *et al*. suggest granular media should "be considered an additional state of matter in its own right [2]." Areas of research within granular media include jamming – the transition of a granular medium from a fluid-like to solid-like phase – and the related occurrence of force chains [3–5], i.e., continuous clusters of particles of high stress surrounded by large collections of unloaded particles, splash functions – descriptions of how a packing reacts to an impact [6,7] by considering particles that are ejected from the medium (hence "splash" functions), impact penetration [8,9], and acoustic phenomena within the packing [10–12]. A further distinction can be made between the study of either random (or disordered) granular systems (e.g., sand or soil) or ordered systems (e.g., crystal lattices), and it has been seen that ordered granular systems exhibit many interesting phenomena not present in random granular media. Since this work will primarily concentrate on wave phenomena in ordered granular media, a review of wave propagation in ordered systems follows.

1.1 Elastic Ordered Granular Materials

1.1.1 One-dimensional elastic granular chain

Within the elastic static regime, the contact between spheres is described by the nonlinear Hertzian potential, in which the force, F, between two spheres (denoted by subscripts 1 and 2) whose centers have been compressed a distance δ is dependent on the relative radius R^*

between two spheres with radii R_1 and R_2 and equivalent Young's modulus E^* between two spheres with moduli E_1 and E_2 and Poisson's ratios ν_1 and ν_2:

$$F = \frac{4}{3}E^*\sqrt{R^*\delta^3}\text{ , where} \tag{1.1}$$

$$\frac{1}{R^*} = \frac{1}{R_1} + \frac{1}{R_2} \text{ and } \frac{1}{E^*} = \frac{1-\nu_1^2}{E_1} + \frac{1-\nu_2^2}{E_2} \; .$$

This nonlinear contact force relationship between two spheres is plotted in Figure 1.1a. A close-up of the contact is shown in Figure 1.1b, where the radius of the circular contact area has been denoted as a. As stated in [13], Eq. 1.1 is valid if the following assumptions are satisfied: "(i) The surfaces are continuous and non-conforming $a \ll R^*$; (ii) the strains are small $a << R^*$; (iii) each solid can be considered as an elastic half-space $a \ll R_1, R_2$; (iv) "The surfaces are frictionless." Note that the one-dimensional (1D) chain of spheres cannot support a tensile load in the absence of an adhesive force.

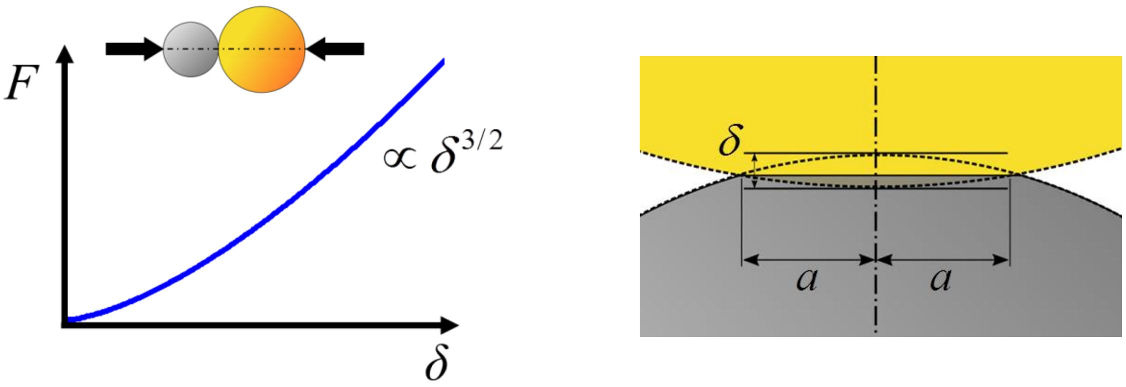

(a) (b)

Figure 1.1: (a) The Hertz contact relationship describes the static compressive force between two elastic spheres in contact, where the contact force, F, has a nonlinear dependence on the displacement between sphere centers, δ. (b) As the two spheres are compressed together, a circular contact area emerges with radius a.

The intrinsically nonlinear force-displacement relationship ($F \propto \delta^{3/2}$) results in a zero slope when no applied force is present. The classical definition [14] of a 1D continuum wave speed as $c=\sqrt{E/\rho}$ (where ρ is the material's density) therefore results in the wave speed of the granular system being zero, a phenomenon known as a "sonic vacuum" [15]. Nesterenko and coworkers [15–18] greatly contributed to the experimental and numerical description of the travelling nonlinearity that occurs in these chains when subjected to an impulse. For the case when the precompression applied to the chain is much less than the exciting force – resulting in a non-zero force in the chain, highly nonlinear solitary waves propagate through the medium. Equations 1.2 and 1.3 describe, respectively, the force amplitude of the solitary wave, F_s, and the solitary wave speed, V_s in a one-dimensional chain of spheres of uniform dimension and material (i.e., the simplest ordered granular medium).

$$F_s = F_m \cos^4\left(\frac{\sqrt{10}}{5D}x\right) \text{ and} \tag{1.2}$$

$$V_s = 0.68\left(\frac{2E}{D\rho^{3/2}(1-\nu^2)}\right)^{1/3} F_m^{1/6}, \tag{1.3}$$

where F_m is the maximum compressive force at the contact between the two identical spheres, D is the diameter, and ρ is the density of the sphere material. Elastic solitary waves, schematically shown in Figure 1.2, are unique when compared to classical continuum linear elastic waves in that the solitary wave speed is dependent on the force amplitude, they have a compact support (i.e., have fixed width of $5D\pi/\sqrt{10}\approx$ 5 sphere diameters), and a fixed $\cos^4$ shape regardless of loading force profile. Of the three solitary waves illustrated in Figure 1.2, the blue curve (dot-dash) is travelling the fastest since it has the highest amplitude while the red curve (dash-dash) has the slowest wave speed since it has the lowest amplitude.

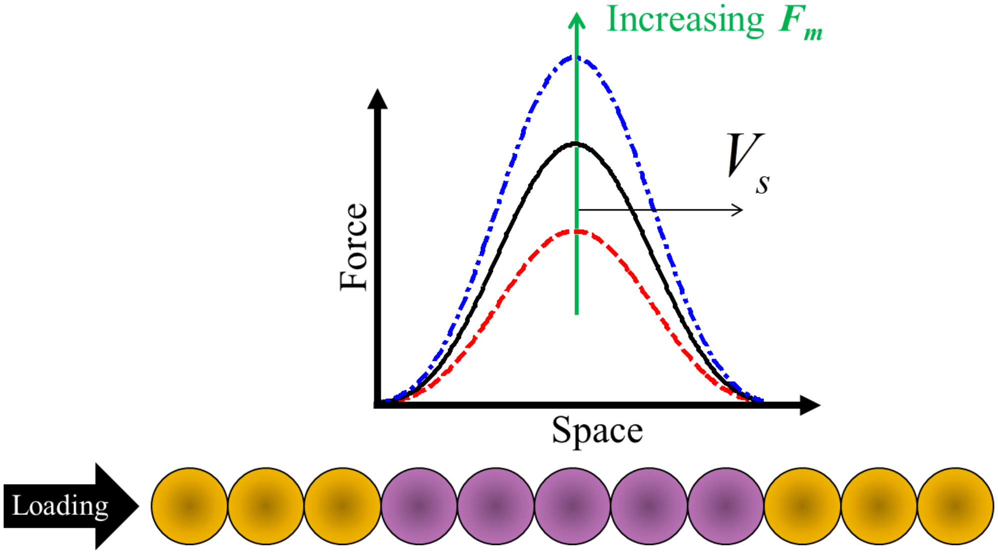

Figure 1.2: Schematic of solitary wave shape ($\cos^4$) and pulse width (~5 sphere diameters). The solitary wave speed, V_s, depends on the force amplitude such that the blue (dot-dash) profile is travelling the fastest and the red (dash-dash) profile is the slowest.

The equations that describe the solitary wave are formulated from the static Hertz contact relation (Eq. 1.1). The formulation is valid since the characteristic time scale of the solitary wave, τ_{sw}, is much longer than the time scale required for sphere homogenization, T, such that wave propagation within individual spheres can be neglected. That is, $\tau_{sw} \gg T \approx 2.5R/c_1$, where R is the radius of the uniform spheres in the 1D chain and c_1 is the velocity of sound in the sphere material [16]. As a typical example, consider that the solitary wave speed in a chain of brass spheres ($d = 9.5\text{ mm}$) is ~290 m/s when the peak force, F_m, is 5 N, whereas the wave speed in brass is 4700 m/s [19]. In this case, τ_{sw} is 164 μs – the pulse width of the solitary wave (the time it takes the 290 m/s wave to travel five sphere diameters) – and is much longer than the time required for homogenization, 2.5 μs.

Extensive literature reviews of wave propagation in 1D granular chains are available in [15,20–22]. Here, we review different arrangements of 1D chains that demonstrate granular medias’ ability to alter the wave speed, prevent certain frequency contents from travelling, and modify the amplitude of the wave. Several applications have been suggested for granular media given their ability to tailor wave propagation and the following introductory review seeks to highlight the design potential of these materials. Several of these traits will be discussed in the configurations examined in this thesis.

Tunability of the wave speed by precompression

Equation 1.3 shows that the solitary wave speed can be altered by changing the amplitude of the applied load. Another parameter than can tune the wave speed is precompression – the placement of a static load on the chain prior to loading [10,15,23]. For the same dynamic contact force, the solitary wave speed was doubled when a chain was precompressed [23]. As the precompression is increased relative to the dynamically applied load, the wave propagation behavior becomes weakly nonlinear and, upon further precompression, linear [15].

Dimers

A dimer chain contains a repeating inhomogeneous unit cell and Figure 1.3 illustrates that unit cells may contain spheres of different materials, different sizes, or both. Dimers still support highly nonlinear solitary waves and the width of the solitary wave is dependent on the mass ratio of the dimer materials [24] while the solitary wave speed depends on the length of the unit cell [25]. Dimers can also be arranged to create band gaps, whereby certain frequencies are prohibited [26–28] from travelling down the chain. Yet, other arrangements permit discrete breathers, or intrinsic localized modes, whereby certain particles can be arranged such that they oscillate with a frequency in the band gap (i.e., forbidden band) [29,30]. Additionally, the resonances and anti-resonances of these systems were explored and it was posited that the anti-resonances in dimer chains could increase the speed of the disturbance within the chain [31] and that the mass ratio between dimers could be adjusted such that the amount of force transmitted through a chain could be tuned from 100% transmission to 65% transmission [32]. Thus, dimers could potentially lead to important engineering applications, such as shock mitigation, sound scrambling, and sound focusing devices.

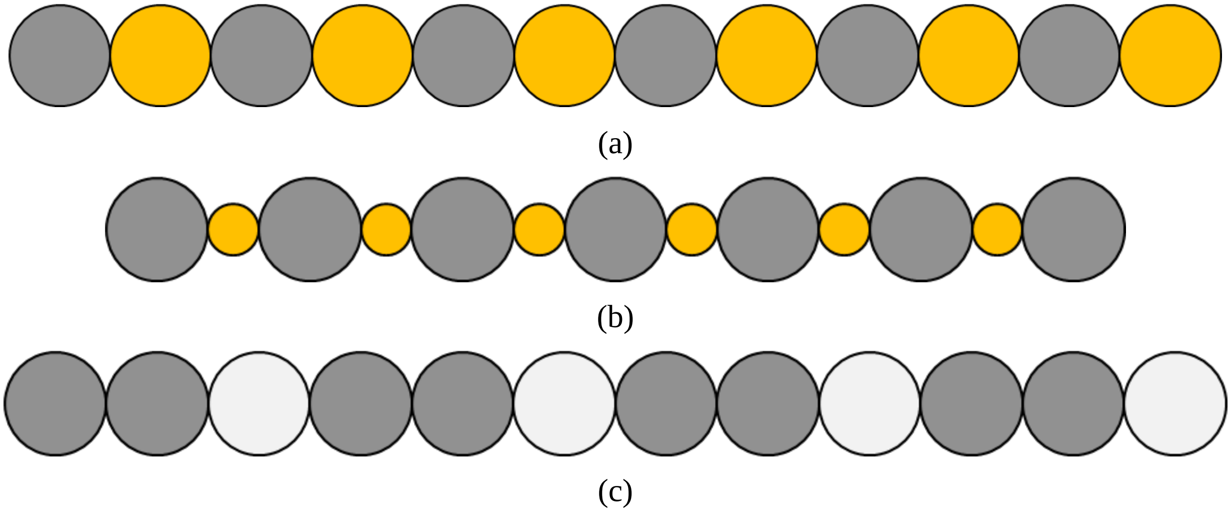

Figure 1.3: Typical dimer chains containing unit cells with spheres of differing (a) material in a 1:1 configuration, (b) material and size in 1:1 pattern, and (c) material in a 2:1 arrangement.

Tapered chains

A simply tapered chain consists of beads with monotonically decreasing or increasing diameter with respect to the impact location, as shown in Figure 1.4a. Such a chain causes the solitary wave to rapidly disperse itself into a collection of smaller impulses due to the inertial mismatches between adjacent beads [33,34]. A binary collision model, which assumes that the collision events by which a pulse propagates involve only two granules at a time, in contrast to a continuum approach, accurately captures the rate of decay of the pulse amplitude and the pulse speed in tapered chains [35–37]. The shock absorption of the chain is further enhanced by placing smaller beads at each contact point in so-called “decorated” chains, as illustrated in Figure 1.4b [38]. These works have been presented as an inexpensive alternative to mitigating unwanted transients, such as ballistic shock, and the tapered chains offer an inherent scalability since the beads can be constructed at diameters appropriate for a given application.

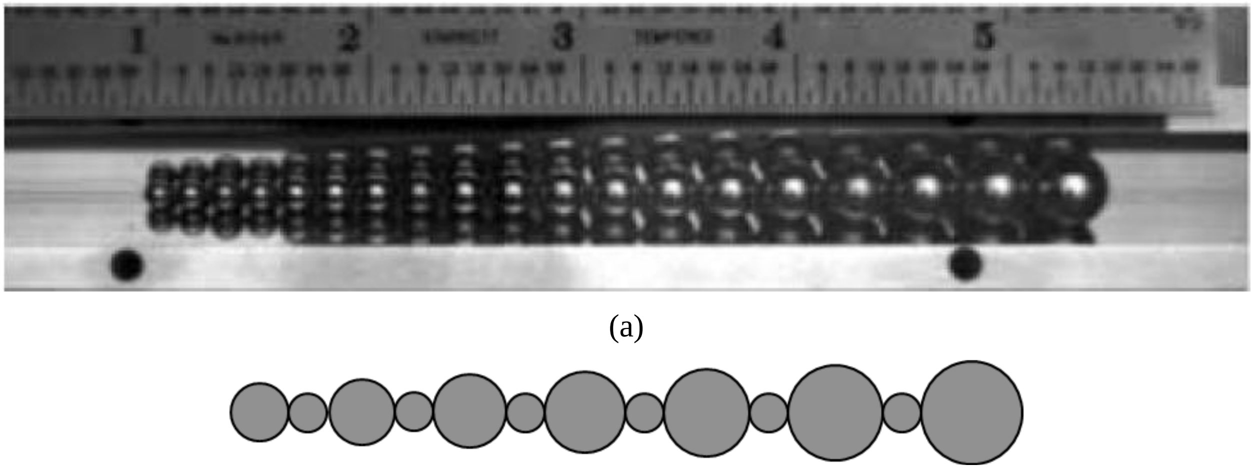

(a)

(b)

Figure 1.4: Tapered chains. (a) Experimental setup of a simply tapered chain (reprinted from [33] with permission of Springer). (b) Schematic of a decorated chain.

Y-chains

One-dimensional chains have also been fashioned into branching networks of chains in what might be considered as a first attempt to alter the path of solitary wave propagation. A solitary wave travelling along a 1D chain can successfully be split at a Y-junction, illustrated in Figure 1.5a. The solitary wave splits at the junction, and if both branches contain identical beads, the two pulses have the same amplitude – about half the pulse amplitude prior to the junction. Continuing along the two branches, the two solitary waves then recombine in the final stem, demonstrating the ability of the solitary waves to travel through the angle in each branch despite energy losses and interaction with the walls [39]. Furthermore, by changing the material in one of the branches, as is shown in Figure 1.5a, different outcomes are achieved such as energy trapping, whereby the solitary wave would reflect back and forth in the more compliant chain until the wave dissipated entirely [39]. The effect of modifying the branching angle and introducing asymmetry in the branching angle was studied in [40,41]. The wave splitting, bending, and recombination was also studied in a branching network in which one chain is eventually split up into four, as shown in Figure 1.5b, and such a network has a higher wave amplitude mitigation rate than comparable continuum materials [42].

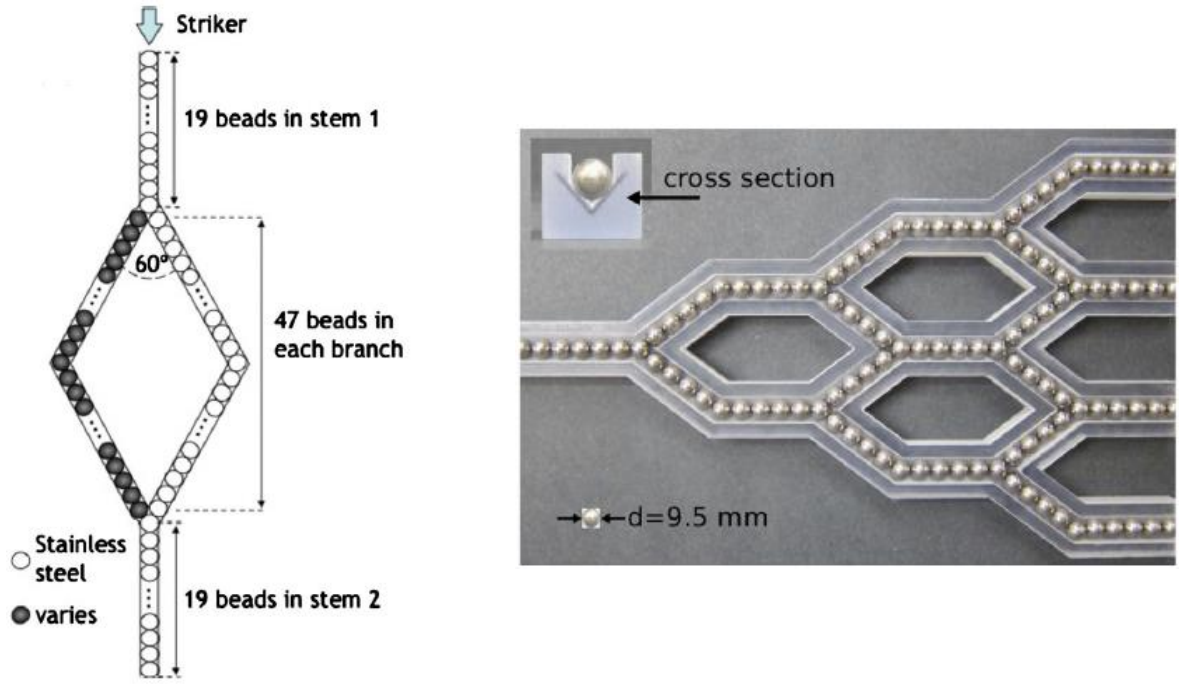

(a) (b)

Figure 1.5: Examples of branching experiments. (a) The 1D chain is split into two chains at a 60° Y-junction and the two branches reconnect at an identical junction (reprinted from [39] by the American Physical Society). (b) An initially 1D chain is branched several times, demonstrating a method of high rate wave amplitude mitigation (reprinted from [42] with permission from Elsevier).

1.1.2 Applications

As discussed above, ordered granular media have the ability to tune the solitary wave speed, filter acoustic frequencies, and reduce the amplitude of the solitary wave. These features have been incorporated into a variety of designs, which highlight the utility of these materials.

Dimers, tapered chains, and branched chains all demonstrated different mechanisms to reduce the amplitude of an input load. Additionally, other chain structures have been shown to reduce the input load by placing lower moduli beads within a chain [43] or by using a magnetic field on a ferrous chain of beads [44]. An optimization scheme was proposed to optimally choose granule sizes, masses, and stiffness to defeat a wave in a 1D granular chain [45]. At a somewhat different length scale granular materials have also been envisioned as being used to protect against earthquakes by dissipating seismic waves with pressurized viscoelastic granules [46] or by placing rings in contact with each other around the foundation of buildings to divert earthquake waves around structures [47,48].

Granular chains have been used to make acoustic switches and logic gates, which can be thought of as mechanical equivalents to their electrical counterparts. Continuously driven chains can allow and forbid (switch on and off) waves of certain frequencies to propagate in the chain and use a dual frequency signal to create AND and OR logic gates [49,50]. Passive designs (not requiring an exciting frequency) for attenuating or switching on and off solitary wave propagation were also explored in [51] and [52]. (The experimental portion of the latter will be discussed in detail in the context of this thesis in Chapter 3.) An acoustic filter was theoretically and experimentally validated within three matrix materials: poly-di-methyl-siloxane (PDMS), polyurethane and a geopolymer, demonstrating the applicablility of these materials as passive dissipaters and passive energy redirectors [53]. The matrix is a necessary step towards practically implementing these materials, as it makes it possible to easily transport, install, and use these systems without disturbing the granular chain.

An acoustic lens is a device that can focus acoustic energy to a specified location. The wave speed is individually tuned in a series of granular chains via precompression such that the waves that emerge in the host medium arrive simultaneously at a focusing point, as shown in Figure 1.6 [54]. The focusing point is determined by appropriately adjusting the precompression levels in each chain. Such a device could be useful for biomedical imaging and other nonintrusive inspections of condensed matter [54] or energy harvesting [55].

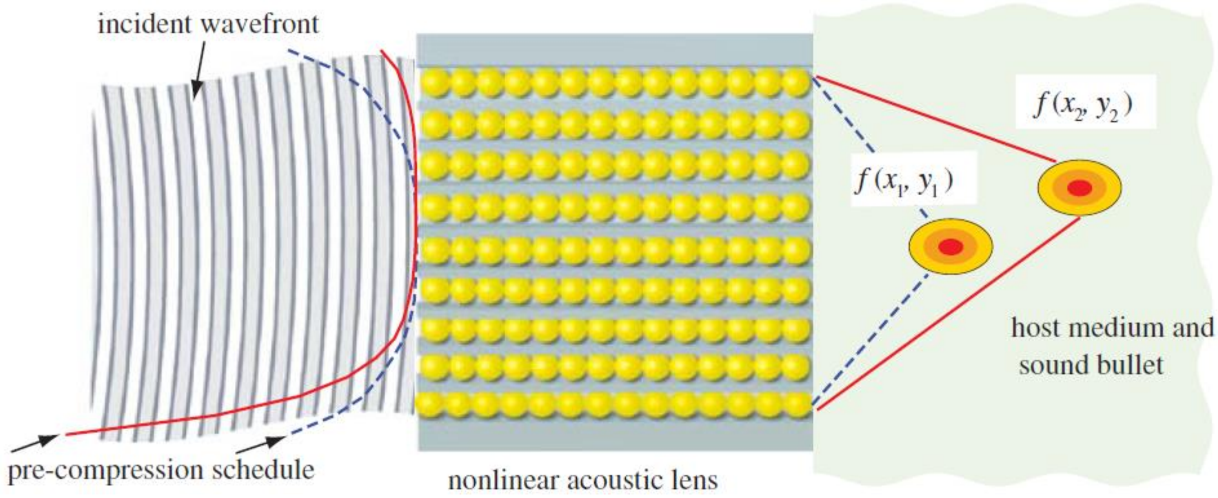

Figure 1.6: Schematic of an acoustic lens, where the time of transit of each acoustic wave through a granular chain is such that focusing occurs in a host medium [54].

Analysis of the transmissions and reflections of highly nonlinear solitary waves generated by 1D crystals into some host material has been utilized in non-destructive evaluation tests. They have been used to detect orthopedic implant stability [56], hydration of cement [57], the impact location in a sandwich structure, delamination in carbon fiber reinforced polymer composite plates [58], and the stresses in thermally loaded beams [59]. These sensors are envisioned as a portable, fast, and relatively simpler (only one transducer required as opposed to two for the ultrasonic pulse velocity method) way of structural health monitoring as compared to other methods.

1.1.3 Two-dimensional ordered elastic arrays

In addition to 1D granular chains, two-dimensional (2D) ordered granular arrays have also been investigated, although to a lesser extent. Experiments and particle dynamics simulations of square packings, in which the beads are considered as point masses connected to each other via nonlinear springs that follow the relationship in Eq. 1.1, have shown that solitary wave propagation occurs only along chains that are in contact with the initial excitation [60,61], i.e., vertically and horizontally only, as shown in Figure 1.7. Thus, this 2D solitary wave propagation is very similar to individual 1D granular chains since there is no coupling between lateral granular chains in a square packing. Further investigations of the square packing have shown that the wave front shape, speed, and magnitude can be highly tailored by modifying the stiffness and mass of intruders placed at every interstitial location [61]. Adding intruders mechanically couples beads that are sited diagonally and thus allows for lateral spreading of the wave. Similar results were observed numerically and experimentally in [62,63], and significant wave redirection was seen to be possible by the presence of just one or two intruders at the interstitial locations [64,65].

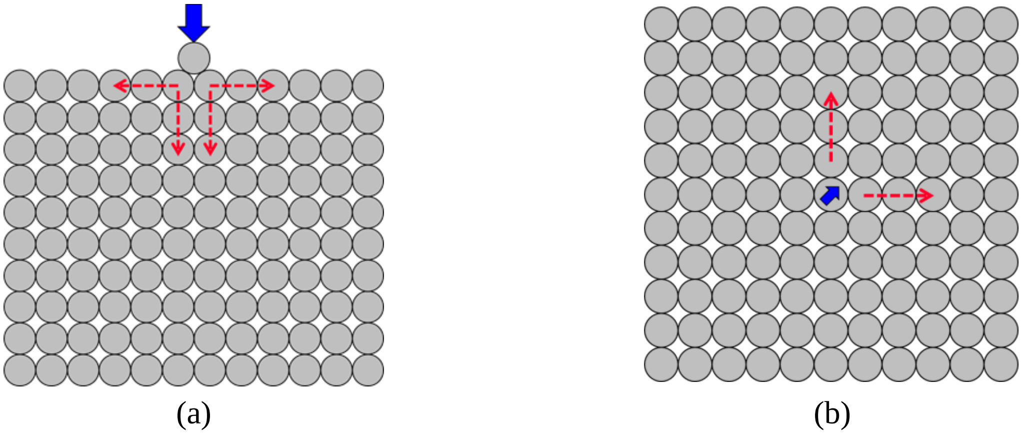
(a) (b)

Figure 1.7: Schematic of a 2D square packing. Solitary wave propagation through a square packing when (a) subjected to a symmetric loading along the top row and (b) the central bead is perturbed at a 45° angle. The red dashed arrows indicate the chains and the direction along which the solitary wave propagates.

Another 2D geometry that is commonly studied is the hexagonal packing, shown in Figure 1.8. Hexagonal packings do not support constant speed travelling waves (unlike the solitary waves in the square packing) since the wave amplitude continuously decays due to wave front spreading through the laterally coupled system [66]. A hexagonal packing consisting of dissimilar material layers reduces the force that is experienced on the opposite side of impact due to the reflection and transmission of contact forces at the material layer interface [67]. Shear loading on a hexagonal system was numerically studied and revealed that the shearing effect attenuates exponentially through the first five layers [68]. Additional studies have been performed on square and hexagonal packings, however, these studies generally focus on the harmonic rather than impact loading and generally have an applied static compressive force greater than the exciting force such that the waves are linear or weakly nonlinear rather than the highly nonlinear waves we study here [69–71].

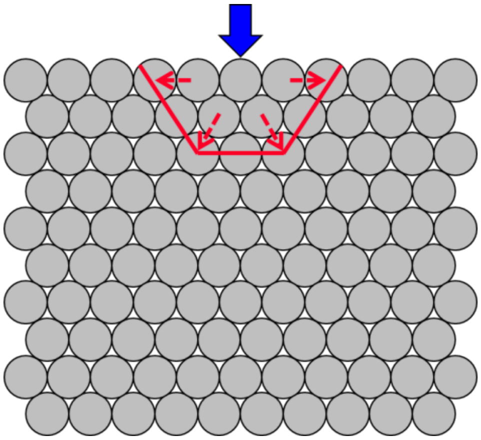

Figure 1.8: Schematic of the 2D hexagonal packing subjected to a point load (blue arrow). The solid line shows the wave front and the dashed arrows indicates the direction of the wave front expansion.

As in the 1D case, potential applications have been crafted from a 2D granular structure such as an acoustic lens [72]. Another application of great interest is a granular material that could "cloak" an impurity or intruder, that is, the granular structure would be configured in such a way that that a probing wave would be redirected around the impurity and detected on the opposite side without any detectable alterations such that it exhibited acoustic transparency. Cloaking designs made from cylinders [73,74] and other metamaterials have been theoretically validated [75].

1.2 Elasto-plastic Granular Materials

The bulk of the literature on the acoustic phenomena that occur within granular media has been conducted in the elastic regime and is therefore valid only for low peak force amplitudes occurring at the stress concentrations at granule contact points. In this work, higher amplitude loading that exceeded the yield force of the granule contacts was utilized to investigate the divergence of the wave behavior from the purely elastic case and the utility of these materials to mitigate impact through plastic dissipation. Of primary interest here are ductile metals which plastically deform when the yield stress is exceeded.

1.2.1 Elasto-plastic contact laws

Classical Hertzian contact theory and the von Mises yield criterion predict that plasticity actually initiates below the contact surface [13]. The critical force for yield initiation for a material with critical yield pressure p_y and uniaxial yield strength σ_y is then:

$$F_y = \frac{1}{6}\left(\frac{R^*}{E^*}\right)^2 \left(\pi p_y\right)^3 \text{, where } p_y = 1.6\sigma_y . \tag{1.4}$$

After this load, the Hertz model is no longer accurate. When a granular medium is loaded beyond yield, a material nonlinearity is introduced by plasticity in addition to the nonlinearity due to the contacts [76].

The Thornton model, shown schematically in Figure 1.9 along with the Hertz model, describes the behavior of an elastic-perfectly plastic bead after yield [77]. After yield, the force-displacement relationship becomes linear and is given by:

$$F = F_y + \pi p_y R^* (\delta - \delta_y), \tag{1.5}$$

where δ_y is the contact displacement at yield. The unloading-reloading is elastic and follows Eq. 1.1, i.e., the Herztian relation. A critical physical value for the Thornton model is p_y, which describes the slope of the linear portion; however, when $p_y = 1.6\sigma_y$, as predicted in the formulation of Eq. 1.4, the Thornton model underestimates the contact force [76,78]. As a way of "salvaging" the Thornton model, studies have experimentally determined the coefficient for σ_y so that they realized good agreement with the functional form of the Thornton model. Typically this fitted parameter is significantly larger than p_y [76,78].

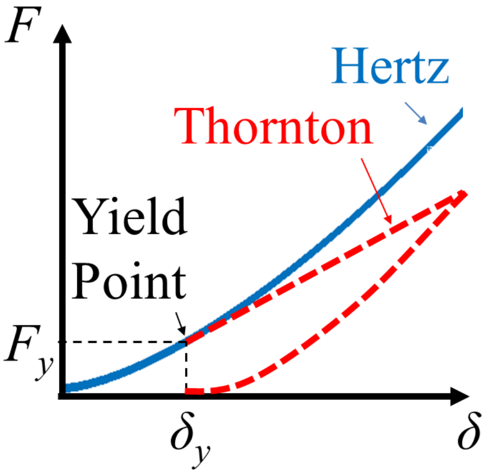

Figure 1.9: Comparison of the Hertz (elastic) and the Thorton (elastic-perfectly plastic) model.

The dynamic contact between two identical granules that deform plastically has also been studied [76] and provided an experimental assessment of an "elasto-plastic contact law" that can be thought of as the plastic equivalent of the Hertzian contact. The same type of studies were also conducted on hemispheres of dissimilar materials and it was found that the dynamic contact behavior in the dissimilar material case is controlled by the material with the lower yield strength [79]. The dynamic contact relations found in [76] then helped create fitting parameters for an elasto-plastic contact law derived from nonlinear finite element analysis that could accurately model initial loading, unloading, and reloading and thus capture the dynamic elasto-plastic properties of a granular medium [80]. The elasto-plastic contact relation proposed in [80] was also used to determine the effect of soft and hard intruders in a 1D chain of particles [81], and will also be used in portions relevant to this study.

1.2.2 Plasticity in ordered granular media

A chain of 5 or more beads loaded above its yield point results in a wave with a primary peak and a trailing pulse, with the primary peak sharing some of the distinctive features of a solitary wave such as requiring ~5 bead lengths to develop and a wave speed that is dependent on peak loading amplitude and scales as $F_m^{1/9.6}$ for brass spheres – slower than the $F_m^{1/6}$ scaling seen in the elastic case [82]. Dimer chains and chains with an intruder particle have also been studied [83]. Further experiments, coupled with a strain rate dependent discrete element method (DEM) model [84], provided a limit for the leading pulse velocity depending on the material properties of the granules as well as the loading amplitude [85].

Granular media have been found to dissipate a larger fraction of energy from an impact load than a comparable continuum medium even though the volume of material involved in the dissipation of input energy is the same between the two systems [86]. Additional work conducted with a drop weight tower demonstrated the feasibility of guiding waves in a 2D packing [87]. Elasto-plastic loading of square and hexagonal packings of spheres were experimentally and numerically studied in [88] and the experimental aspects will be discussed in subsequent

Chapters 4-6 of this work. Optimizing a 2D packing of spheres subjected to elasto-plastic loading was presented in [89] and will motivate the work in Chapter 5.

1.2.3 Preconditioning

Although some aspects of solitary wave propagation are maintained during plastic dynamic loading of 1D metallic chains [82], plastic dissipation dominates the chain's response with the majority of force attenuation taking place because of localized yielding at the granular contact points. Although this can be exploited by increasing the amount of plastic dissipation in a granular medium vs. an equivalent continuum material, as has been numerical studied in [86], suppressing the propagation of solitary waves means that it will be more difficult under plasticity conditions to exploit the type of designs described earlier in Section 1.1.2. Therefore, it is of value to be able to sustain solitary waves at forces higher than those that cause (initial) yield so that material designs based on elastic solitary waves can be used in realistic applications. Note that using empirically determined values of p_y (which are higher than predicted in Eq. 1.4) [76], the yield force for a brass and aluminum bead with diameter 9.5 mm is still only 126 N and 197 N, respectively. If using the von Mises yield, these values are smaller.

Wang *et al.* achieved high amplitude solitary waves (kN) by the use of preconditioned beads [90]. Two metallic spheres can be made to remain elastic during a high-amplitude loading event by initially preloading, or "preconditioning", their contact beyond the expected loading amplitude in the event. Figure 1.10 conceptually illustrates the preconditioning process which takes an as-manufactured bead, compresses it past the yield force, F_y (at deformation δ_y), to some maximum force, F_{max} (at deformation δ_{max}) and then elastically unloads it. At the end of the preconditioning process, there is some residual plastic deformation δ_r and the curvature at the contact is recovered, but now with a much larger radius of curvature than the initial bead radius.

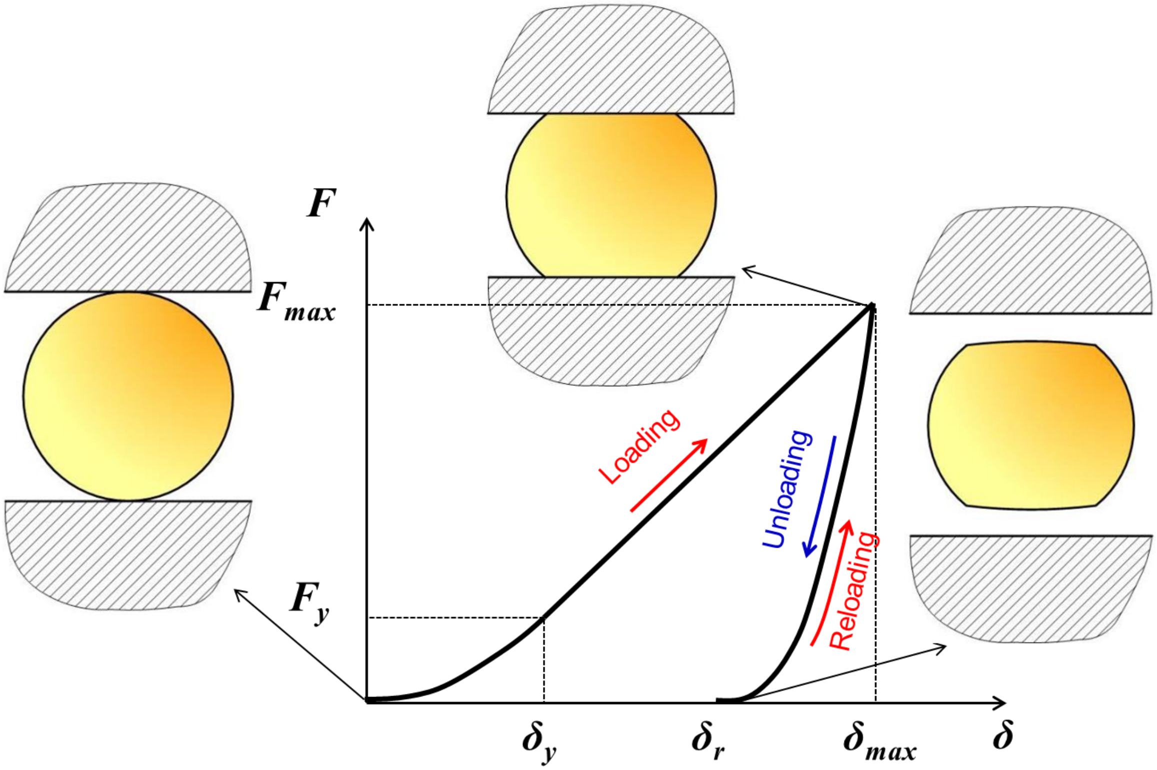

Figure 1.10: Schematic of the preconditioning process beyond yield to a maximum force, F_{max} (at deformation δ_{max}).

Preconditioning effectively increases the contact radius and hardens the bead, consequently increasing the yield load of the contact. Although the preconditioned spheres have been plastically deformed, they now allow a high-amplitude wave to propagate without further plastic dissipation as long as the preconditioning load, F_{max}, is not exceeded. Figure 1.11 demonstrates the dependence of the solitary wave speed in a chain of preconditioned beads on the peak input force and the preconditioning level. Notably, the solitary wave has accomplished much higher amplitudes (on the order of kN) than in previous studies [90].

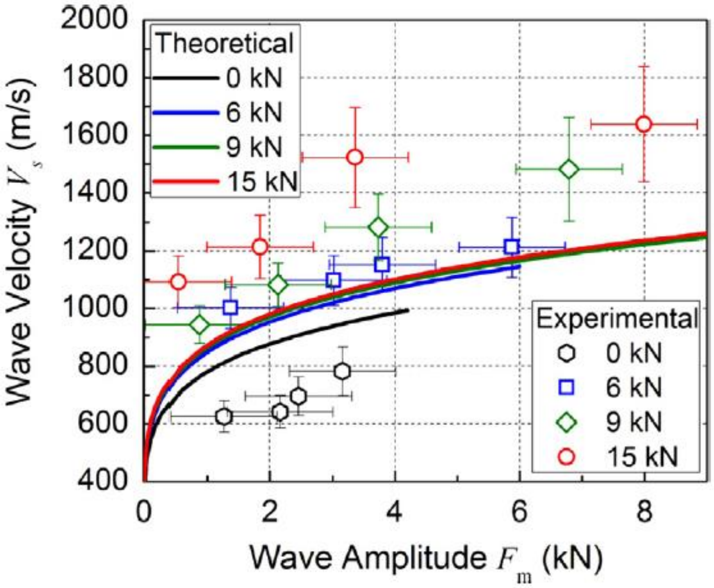

Figure 1.11: Experimental and analytical results demonstrating the ability to permit and tune high amplitude solitary waves using preconditioned contacts (reprinted from [90] with permission from Elsevier).

1.3 Statement of Objectives

The experimental investigations detailed in this thesis seek to manage wave propagation in granular systems so that they exhibit wave characteristics that cannot be achieved using “traditional” homogeneous materials. Within this overarching context of developing materials with revolutionary wave mitigation properties, the objectives of the work detailed herein are to:

- Design unique geometries/arrangements in 1D granular media that exhibit properties inspired by electromagnetics, such as switching and filtering.
- Investigate elasto-plastic wave propagation (i.e., wave speed and amplitude, shape of the wave front) in a square and a hexagonal packing and inspect the plastic dissipation at the contact granules along certain propagation paths.

- Tailor a 2D granular system to enable regions of preferred wave propagation (e.g., regions with faster and/or higher-amplitude waves) so as to achieve desired wave response to a wide variety of spatiotemporal inputs.

Chapter 2 of this document will discuss the experimental techniques used to load and record data within the granular arrangements of interest. Chapter 3 will explore two mechanical analogues of electrical systems: an elastic tunable system that allows wave propagation in one orientation and severely hinders wave propagation in a different orientation, similar to a switch, and a 1D chain that is elasto-plastically loaded and can act as a low-pass force filter by selectively preconditioning the contacts within the chain.

Chapter 4 expands this work to include 2D dimensional arrays and investigates the elasto-plastic wave propagation in square and hexagonal packings. A cornerstone of this work is to manage (i.e., deflect or disperse) and/or mitigate (i.e., reduce in amplitude) high-amplitude waves in granular media. While plasticity at granule contact points provides an effective means of wave dissipation, it does not offer any wave control of high amplitude stress waves. Chapter 5 seeks to tailor the wave propagation in a square packing of beads by placing cylinders at interstitial locations inspired by an optimization scheme. Chapter 6 explores tailoring elasto-plastic wave propagation in a hexagonal packing by preconditioning the contacts. Finally, Chapter 7 offers concluding remarks on the work herein and the future directions of research.

2. EXPERIMENTAL METHODS

2.1 Granular Materials and Load Frame

The granules used in this study were spherical beads made of brass alloy 260 obtained from McMaster-Carr and Salem Specialty Ball Company and, according to the manufacturer specifications, had a diameter of 9.53 mm (3/8 in), density 8500 kg/m^3, Young's modulus 115 GPa, Poisson ratio 0.3, and a yield strength of 550 MPa. In all subsequent Chapters except Section 3.1, the beads were contained in a custom-built frame made of 1018 low carbon steel, as shown in Figure 2.1 (photograph shown in the inset of Figure 2.1). The beads were arranged in the desired configuration atop a steel base covered with a polytetrafluoroethylene (PTFE) sheet with a thickness of 0.1 mm to minimize friction with the base plate. The frame had adjustable walls to accommodate different bead arrangements and, once the walls were appropriately placed in each case, they were fixed with flange nuts. The portions of the frame that were in contact with the granular packing were heat treated to ensure a Rockwell C hardness of 55 (Vickers 639) which was much higher than the surface hardness of the brass beads (Rockwell B hardness 75, Vickers 135). For the case of point loading, a loading bead was in contact with an adapter bar (see Figure 2.1) which, in turn, was in contact with the loading mechanism, a Hopkinson bar which will be discussed in the next Section. The adapter bar freely moved through a hole in the steel frame. Using an adapter bar with a smaller diameter than the incident bar reduced the size of the opening in the frame and prevented the incident bar of the loading mechanism from impacting the base plate. Two adapter bars were used – one made of stainless steel and one composed of tungsten carbide (WC), the latter impedance matched with the Hopkinson bar – and each will be discussed in the relevant Chapters.

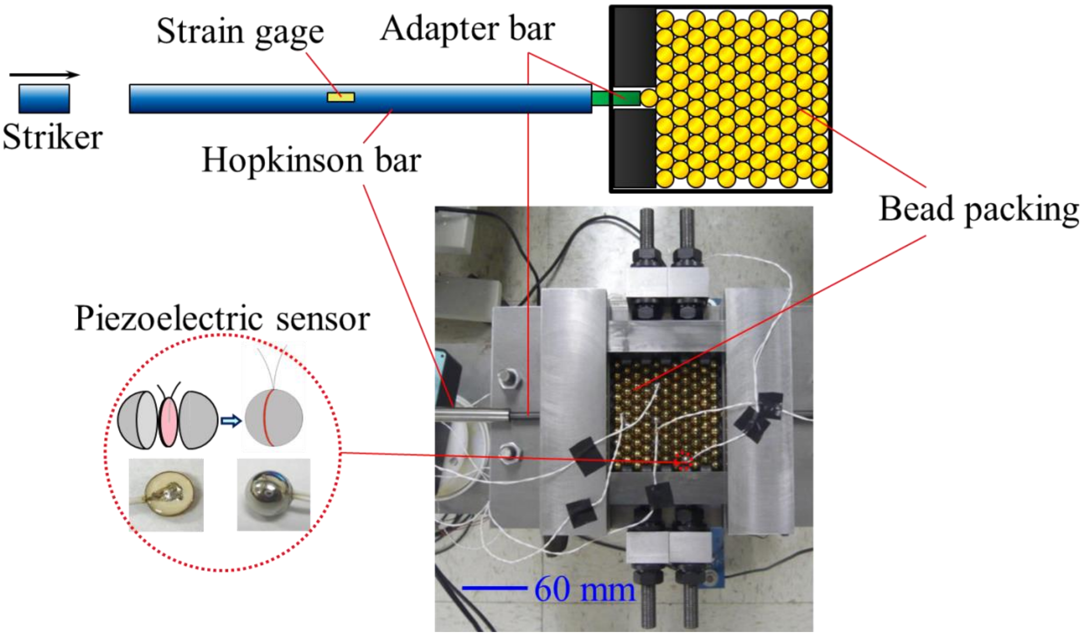

Figure 2.1: Experimental setup for impacting the 2D ordered granular media with a point loading. The packing is impacted with a Hopkinson bar and beads with embedded sensors measure the force profiles in the packing.

In the case of line-loading, the wall closest to the impact site was removed and replaced with a triangular fan made of aluminum, a photograph and three-dimensional (3D) solid model of which are shown in Figure 2.2a-b. The dimensions of the plate are provided in Figure 2.2c. The triangular plate contacted the Hopkinson bar as shown in Figure 2.2d. The base of the triangle was in contact with the granular packing, as shown in Figure 2.3a. Figure 2.3b shows signals from strain gages placed along the base of the triangular plate near the granular packing, where the numbers in the legend correspond to the (upside-down) numbers in the photograph. The similar signals indicated that the load from the Hopkinson bar was evenly spread along the base of the aluminum plate. Thus, we considered this set-up as generating planar loading where each bead in contact with the aluminum plate received about the same load.

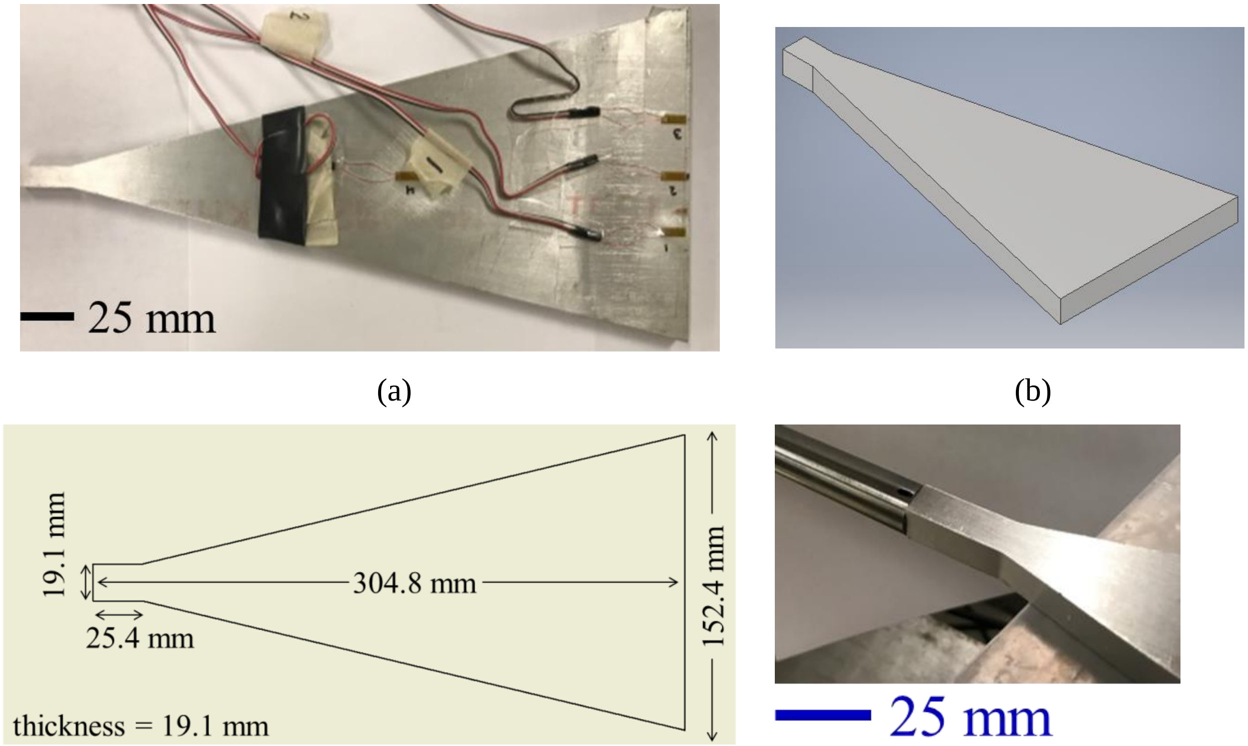

(a) (b)

(c) (d)

Figure 2.2: (a) Photograph and (b) 3D solid model of the aluminum triangular plate used in line loading experiments. (c) Schematic of the plate with dimensions. (d) Interface with Hopkinson bar.

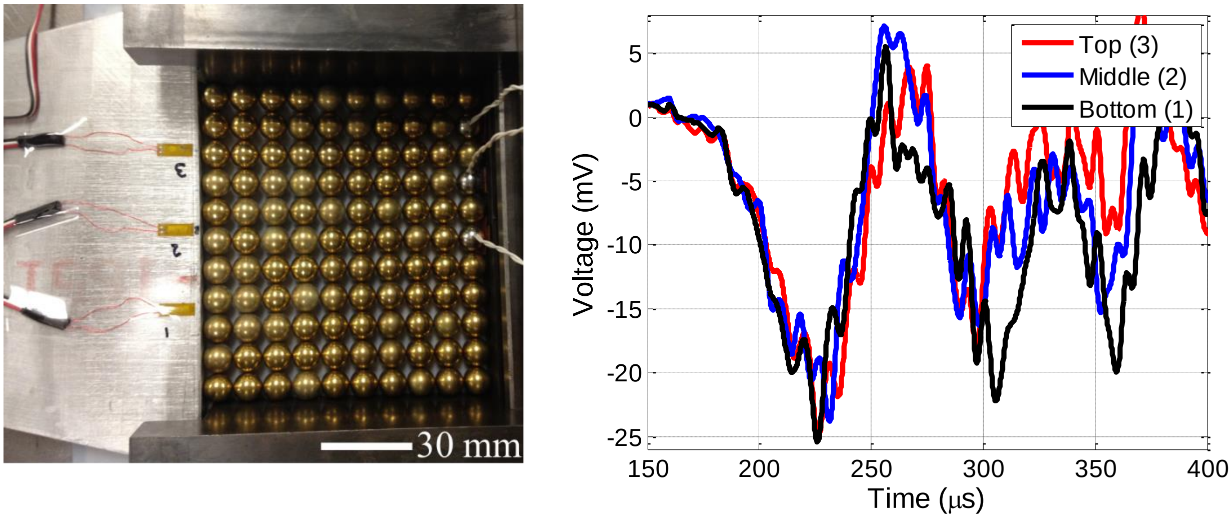

(a) (b)

Figure 2.3: (a) Aluminum triangular plate in contact with the granular packing for producing planar loading. (b) Signals from each strain gage when the plate is impacted. Numbers in the legend correspond to numbers (upside down) in the photograph.

2.2 Hopkinson Pressure Bar Loading

The primary loading mechanism in these experiments was a Hopkinson pressure bar, shown in Figure 2.1. The setup consisted of a gas gun, striker, and incident bar. The striker bar and incident bar had the same diameter (12.7 mm) and were made of maraging steel C350, which had a Young's modulus, E, of 200 GPa. The striker was propelled to impact the Hopkinson bar by compressed air. Upon impact, an incident compressive pulse was generated and travelled down the Hopkinson bar. A reflected pulse was sent back from the interface with the stainless steel adapter bar, or, if the impedance matched WC adapter bar was used, the granular medium. Two strain gages (Vishay Micromeasurements model EA-06-250BK-10C) on the Hopkinson bar recorded the incident and reflected signals as voltages, as in Figure 2.4a; the strain gages were placed on diametrically opposite sides of the bar such that the average of the two signals minimized the effects of bending waves. The strain gages were connected to a signal conditioner and amplifier in the Wheatstone quarter-bridge configuration (in-depth details on stain gage circuits and instrumentation can be found in [91]). The strain, ε, was calculated by converting the recorded voltage, $V_{measured}$, using the following relation:

$$\varepsilon = \frac{\dfrac{4V_{measured}}{GV_{excitation}}}{gf\left(1+\dfrac{2V_{measured}}{GV_{excitation}}\right)}, \qquad (2.1)$$

where the gage factor, gf, was a property of the strain gage and had a value of 2.105, and the gain, G, and the excitation voltage, $V_{excitation}$, were properties of the signal conditioner and amplifier box and had values 31 and 15 V, respectively.

Once the voltage signal was converted to strain by Eq. 2.1, the incident (ε_i) and reflected (ε_r) strain pulses were shifted so that they began at the same time, as shown in Figure 2.4b.

Assuming a 1D stress state, which is typical for Hopkinson bar analyses since the length of the bar (1.52 m) is much larger than the diameter (12.7 mm), it was possible to determine the input force through the relation $F_{input} = -EA(\varepsilon_i + \varepsilon_r)$, where E and A were the Young's modulus and the cross-sectional area of the incident bar, respectively [92]. The resulting force profile is plotted in Figure 2.4c.

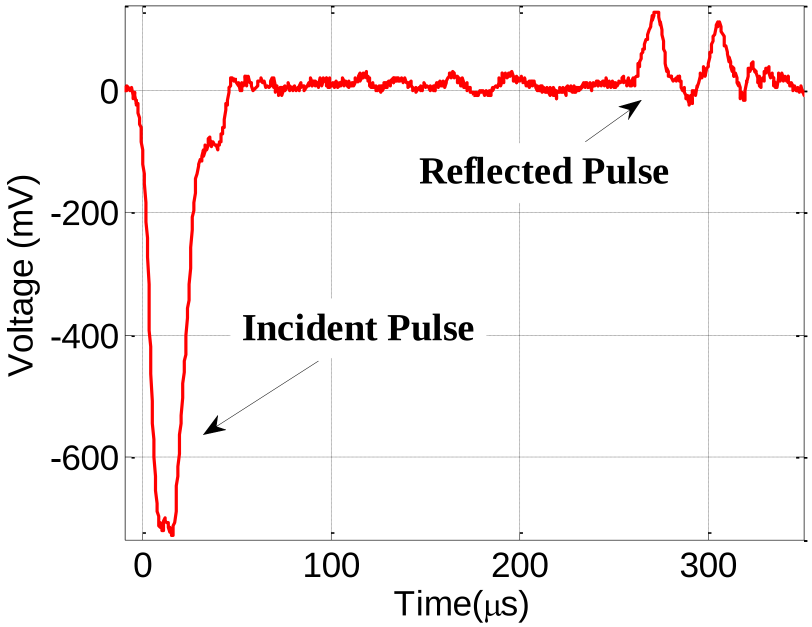

(a)

Figure 2.4 (cont.)

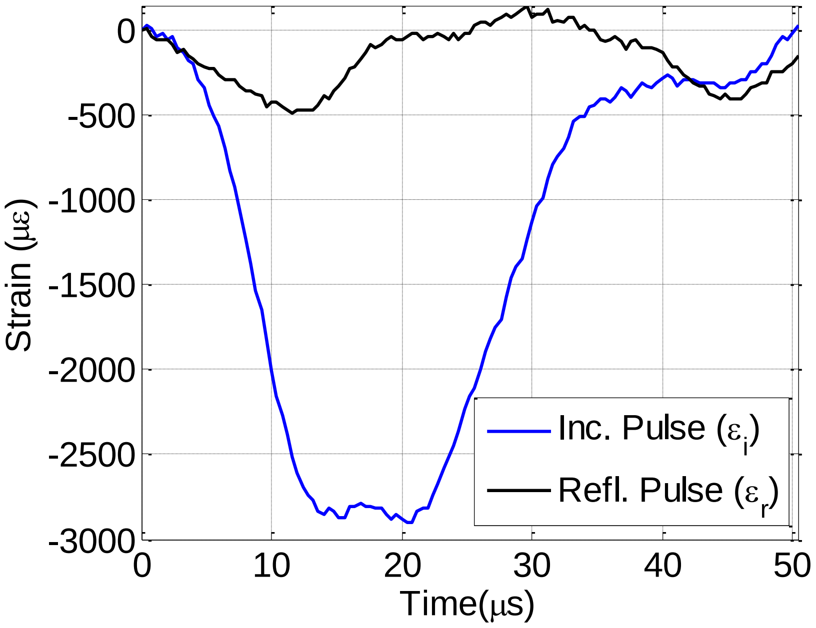

(b)

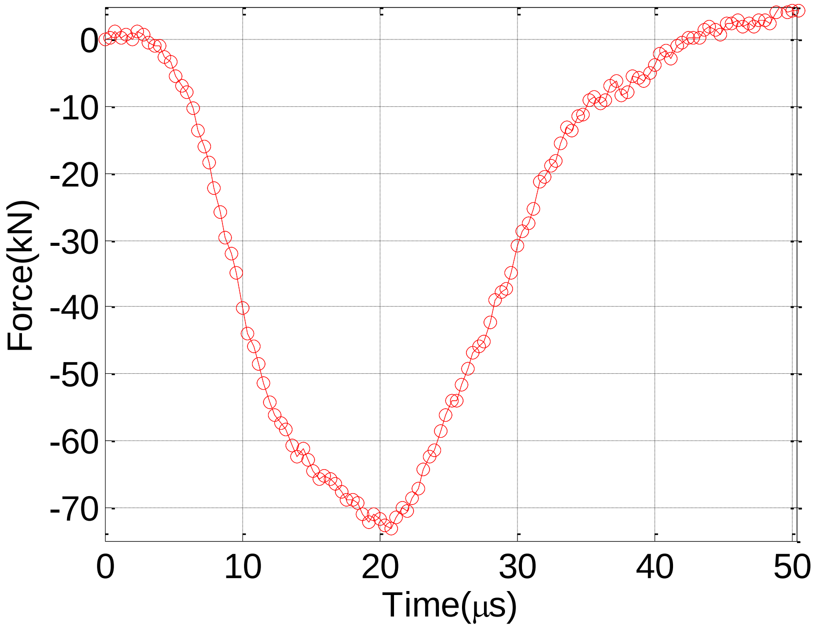

(c)

Figure 2.4: Determination of input load into the granular system. (a) The two voltage signals from the diametrically opposite strain gages have been averaged to remove bending effects. (b) The incident signal and the negative of the reflected signal have been cut and overlapped, such that the sum of the two signals gives (c) the input force into the granular medium.

2.3 Piezoelectric Sensors

Diagnostics were also required to study the propagation of waves within the granular packing itself. Piezoelectric sensors were suitable for this task since they could capture the frequency content of the waves to be investigated (10s of kHz) and survive the expected loads (kNs). A further advantage was that piezoelectric sensors were sufficiently small to fit within a sphere, allowing measurements within a 1D granular chain or 2D packing. Piezoelectric sensors also have a well-established history of studying wave propagation in granular materials and have been used extensively in the study of wave propagation in granular materials [15,18,23,90,93–95].

2.3.1 Principles of operation

A piezoelectric material refers to a crystalline structure that has the ability to convert a mechanical displacement into a voltage and vice versa such that it will produce a given voltage for a given strain [96–98]. These materials are often used as passive sensors meaning that no external exciting voltage is required for them to generate a signal. The operational range of the sensor is between the cut-off frequency, f_c, and the resonant frequency of the sensor, f_r [96]. The cut-off frequency is defined as $f_c = \frac{1}{2\pi\tau}$, where τ is the circuit's time constant – the time it takes the signal to decay to ~63% of its initial amplitude. The time constant is calculated as $\tau = RC$, where R and C are the equivalent circuit's input resistance and capacitance, respectively, and, for the sensors in this work, $R = 2$ MΩ and $C = 3000$ pF ± 15%. The time constant was then calculated as approximately 6 ms ($\tau = RC \approx (2\ \text{M}\Omega)(3000\ \text{pF}) = 6\ \text{ms}$). The specific material used in this work was lead zirconate titanate (PZT), which is known to have a high coupling factor between voltage and strain [99]. An in-house resistive box was constructed to reduce the amplitude of the piezoelectric signal, so that the maximum voltage would be within the ±25 V range of the Agilent Technologies DSO6104A digital storage oscilloscope used for data recording. The frequency content of the elasto-plastic solitary-type waves in this work ranged from 20-40 kHz, as measured from Fast Fourier Transforms of typical signals [100,101]. The measured frequency content was well below the resonance frequency of the sensor (300±10 kHz), and above the cut-off frequency of the circuit (170±30 Hz).

The time required for a bead to homogenize is $T \approx 2.5R / c_1$ [16]. For brass and steel spheres with a diameter of 9.53 mm, the homogenization time is less than 2.53 μs, occurring at a frequency much higher than what the piezoelectric sensor can detect. Thus, the piezoelectric sensor does not provide the force history of oscillatory waves within a sphere prior to homogenization (i.e., the "ringing"), but instead, a homogenized force value that is related to the contact forces experienced by the sphere (discussed below). The contact forces depend on the propagating solitary waves or plastic solitary-type waves observed in [83], and in this work the waves had characteristic times which range from 20 μs to 470 μs and were within the bounds of what the piezoelectric sensor could reliably detect.

2.3.2 Sensor construction

Beads with embedded piezoelectric sensors (hereinafter referred to as instrumented beads) provided in-situ measurements of the arrival time of a stress wave and the average value of the contact force on either side of the bead at select locations within the packing. Note that since the contact forces changed with time, the value of the average contact force was also time dependent. An instrumented bead consisted of a PZT disk (*d* = 7 mm, thickness = 0.2 mm, obtained from Steiner & Martins, Inc.) with silver electrodes and in-house attached lead wires that was inserted into a bead that was appropriately machined to accept it, as shown in the circular inset of Figure 2.1. A close-up photograph and 3D solid model of the machined bead are shown in Figure 2.5a-b and the dimensions of the machined area are given in Figure 2.5c. The properties of the PZT disk are given in the Appendix, but of note is that the solidus/liquidus temperature of the solder used in the construction of the sensor (361A-20R, obtained from Vishay MicroMeasurements) is 183 °C – well below the Curie temperature (320 °C) of the disk, so it was not expected that the temperature from the soldering iron damaged the sensors. After the wires were attached, the PZT disk was adhered into the appropriately machined hemispheres with polyurethane, which also served to electrically isolate the piezoelectric disk. The instrumented beads were made of stainless steel 440C rather than brass and had a final diameter of 9.2 mm. A photograph of the assembled instrumented bead is shown in Figure 2.5d. The reason for using steel sensor beads rather than brass ones was that, in the range of loads present in these experiments (up to 25 kN), only the brass bead yielded in the brass-steel bead dimer; thus, the stainless steel 440C sensor remained elastic throughout the experiment [79], which allowed for an appropriate calibration and the repeated/repeatable use of the piezoelectric force sensors. The disadvantage was that there a material mismatch existed wherever a bead sensor was placed. As a result, in order to minimize issues associated with this material jump, steel sensor beads were placed primarily at granule locations contacting the surrounding wall.

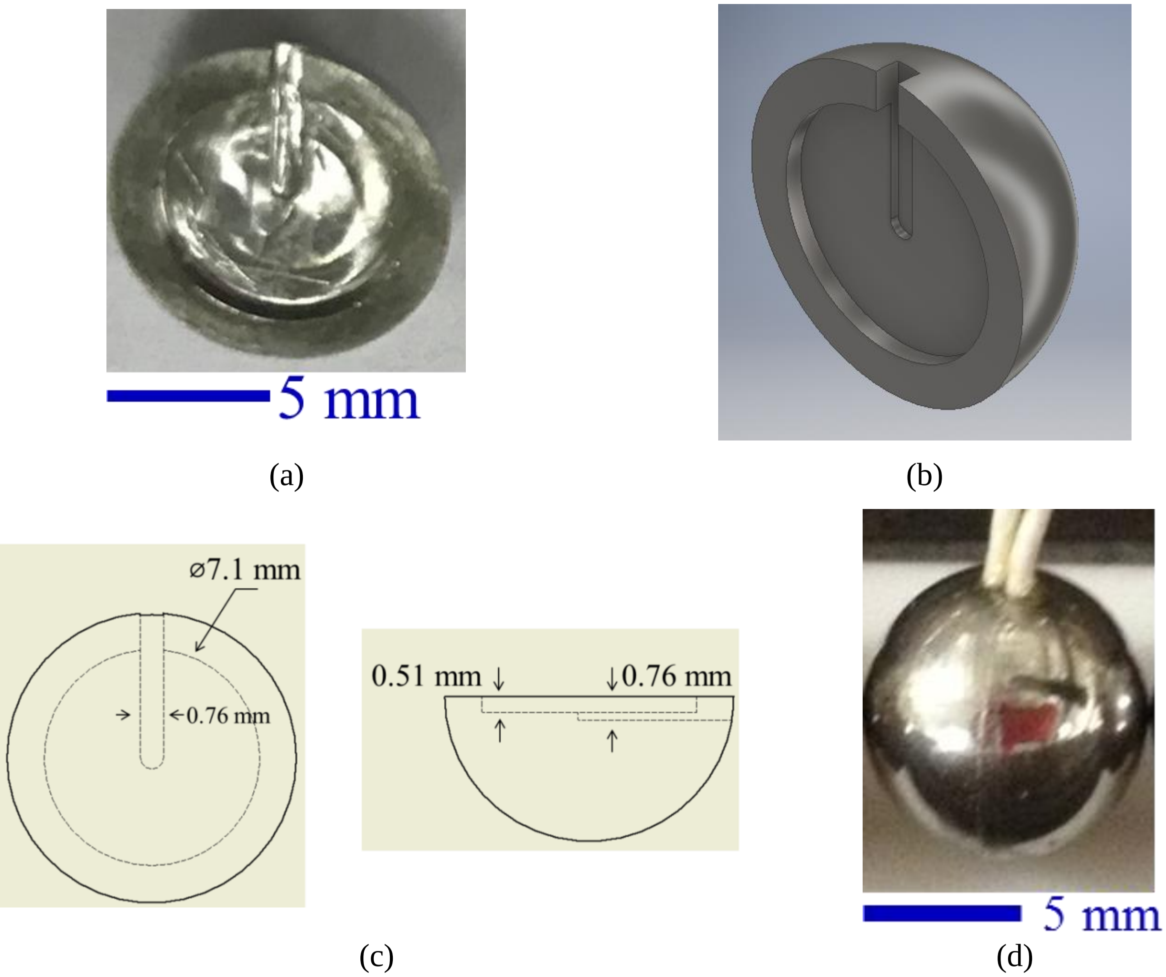

Figure 2.5: (a) Photograph, (b) 3D solid model and (c) schematic with dimensions of the machined stainless steel sphere that accommodates a piezoelectric sensor. (d) Photograph of the assembled instrumented bead.

2.3.3 Sensor calibration

As discussed above, the time constant of the system was approximately 6 ms, which did not allow quasi-static measurement since the charge from the piezoceramic dissipated before a desired load level was reached. For low amplitude events, an oft-used procedure to calibrate the sensor in the range of tens of Newtons is the “ball-drop” technique [18,102]. Conservation of momentum used to calculate the input force of the bead and then the voltage in the bead is calibrated to a numerically simulated solitary wave, with the same granular chain parameters and input force. Furthermore, the voltage only measures the average of the contact forces, so the contact force must be reconstructed by manipulating the signal [18]. This conservation of momentum approach was used here for calibrating the sensors used in the set of elastic experiments in Section 3.2; however we forgo an explanation here since the technique is explained with great detail in [18,102].

The remainder of this dissertation focuses on high-amplitude events (where the peak forces that reach the sensors could be on the order of kN), so a different calibration approach was employed. The calibration method was published in [90], and will be explained here in detail since it was essential to many of the measurements made in this work. Figure 2.6 shows a schematic of the calibration setup in which a clear plastic tube supported the instrumented bead and two brass beads, which were placed immediately upstream of the instrumented bead. These two brass beads shaped the pulse that reached the instrumented bead in a manner favorable to the calibration technique by forming a sinusoid-like wave that monotonically increased to a peak value before monotonically decreasing. The plastic tube containing the beads was in contact with the Hopkinson bar. A fourth bead was placed at the opposite end of the tube and was propelled by a gas gun to impact the short granular chain. Impacting the short chain with a bead of the same mass as the other beads in the chain was beneficial since it resulted in a single pulse which allowed for an easier comparison with the signal in the Hopkinson bar. If the impactor were more massive, then a train of solitary waves would emerge [18] that would complicate the calibration process.

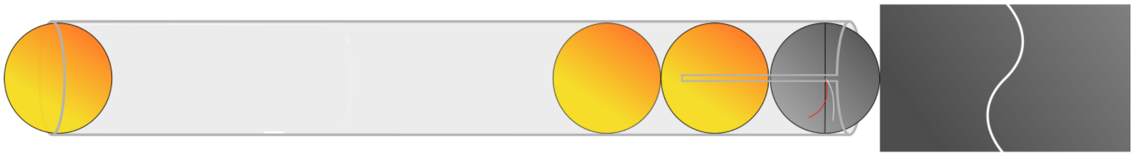

Figure 2.6: Calibration setup. The instrumented bead is placed between two pulse-shaping beads and the Hopkinson bar. Another bead is propelled into the granular chain by a gas gun.

During impact, voltage signals were acquired from the instrumented bead and from the strain gages on the Hopkinson bar. The voltage signals from the Hopkinson bar strain gages were converted to force using the procedure outlined above in Section 2.2. Throughout impact, the instrumented bead experienced two contact forces, $F_1(t)$ and $F_2(t)$, that were a function of time, t, as shown in Figure 2.7. The signal acquired from the instrumented bead corresponded to its average contact force, $F_{avg}(t) = (F_1(t) + F_2(t))/2$. However, the signal from the Hopkinson bar corresponded to the contact force $F_2(t)$ only, so a direct calibration between the force from the Hopkinson bar and the voltage from the sensor was not appropriate. First it was necessary to reconstruct the signal that corresponded to the contact force of the instrumented bead from the voltage signal that corresponded to the average contact force. The two contact forces, $F_1(t)$ and $F_2(t)$, have the same profile if the bead remain elastic, which was the case here since the steel bead does not yield when in contact with the brass beads at the load levels of interest [79].

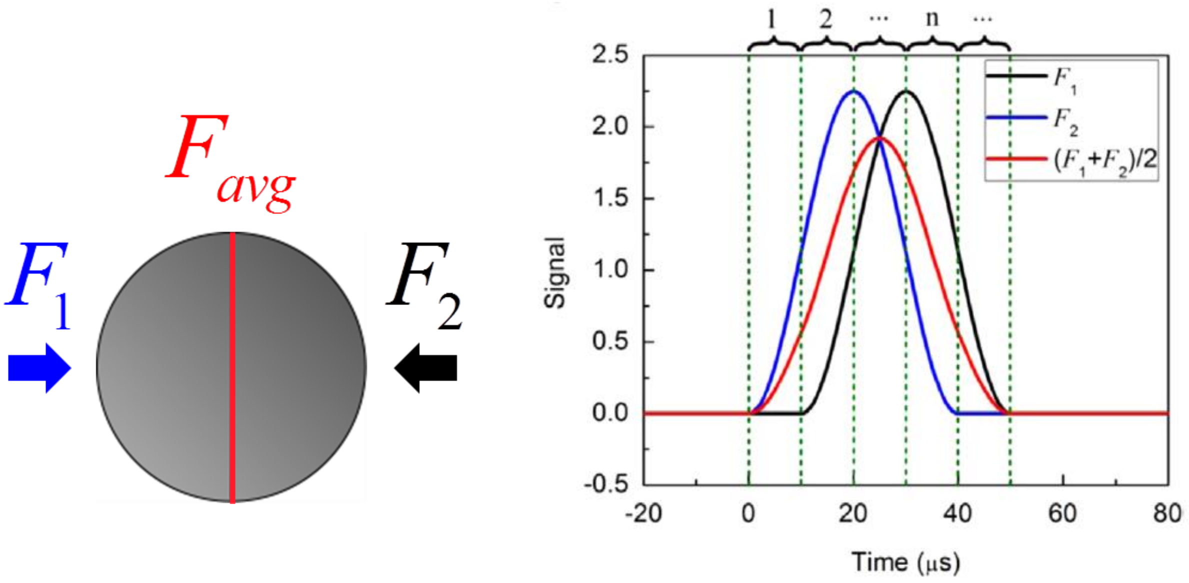

(a) (b)

Figure 2.7: (a) Illustration of the relevant forces for the instrumented bead calibration. (b) Plot displaying the contact force and the average contact force, subdivided into the intervals t_{step} (reprinted from [90] with permission from Elsevier).

Now, the critical quantity needed to reconstruct the contact force profile was the time difference between when $F_1(t)$ began acting on the bead and when $F_2(t)$ began acting on the bead, a quantity referred to as t_{step}. In Figure 2.7b, the interval t_{step} is denoted by dashed green lines and in the first interval (interval markers along the top of the graph), $F_2^1(t)$ has not arrived yet and is zero, so the only force acting on the instrumented bead is $F_1^1(t)$, where the superscripts indicate the contact forces in the first interval. Recalling that $F_{avg}(t) = (F_1(t) + F_2(t))/2$, the left contact (i.e., the contact between the instrumented bead and the pulse-shaping bead) profile can now be calculated as $F_1^1(t) = 2F_{avg}^1(t) - F_2^1(t) = 2F_{avg}^1(t)$. Furthermore, since the contact force profile at the right contact (i.e., between the instrumented bead and the transmitted bar) have the same shape as the left contact profile, it can be calculated as:

$$F_2^{n+1}(t) = F_1^{\,n}(t), \tag{2.2}$$

where n is the interval quantity and is greater than zero. In general, the contact force profile $F_1(t)$, is calculated with the equation:

$$F_1^{n+1}(t) = 2F_{avg}^{n+1}(t) - F_2^{n+1}(t) = 2F_{avg}^{n+1}(t) - F_1^{\,n}(t)\,. \tag{2.3}$$

The value t_{step} was found experimentally by investigating a plot of the original signal from the instrumented bead and the contact force profile from the Hopkinson bar, as shown in Figure 2.8a. The two signals in Figure 2.8a were triggered at the same time by the instrumented bead. The Hopkinson bar signal was shifted such that the transit time from the instrumented bead-Hopkinson bar interface to the strain gage was removed. The delay between the arrival of the sensor signal (red) and the strain gage signal (black) was determined to be 10 μs. Once t_{step} is known, the contact force F_1 can be included in the plot by simply shifting F_2 by $-t_{step}$, as done in Figure 2.8b. From Figure 2.8b, the peak voltage of the sensor was calibrated to the force value at $F_1(t) = F_2(t)$, which is 1.8 kN at $t = 26\ \mu s$. Figure 2.8c shows that, using Eqn. 2.2, the contact force can be successfully reconstructed (red) from the average force signal to match the original contact force signal detected by the transmitted bar.

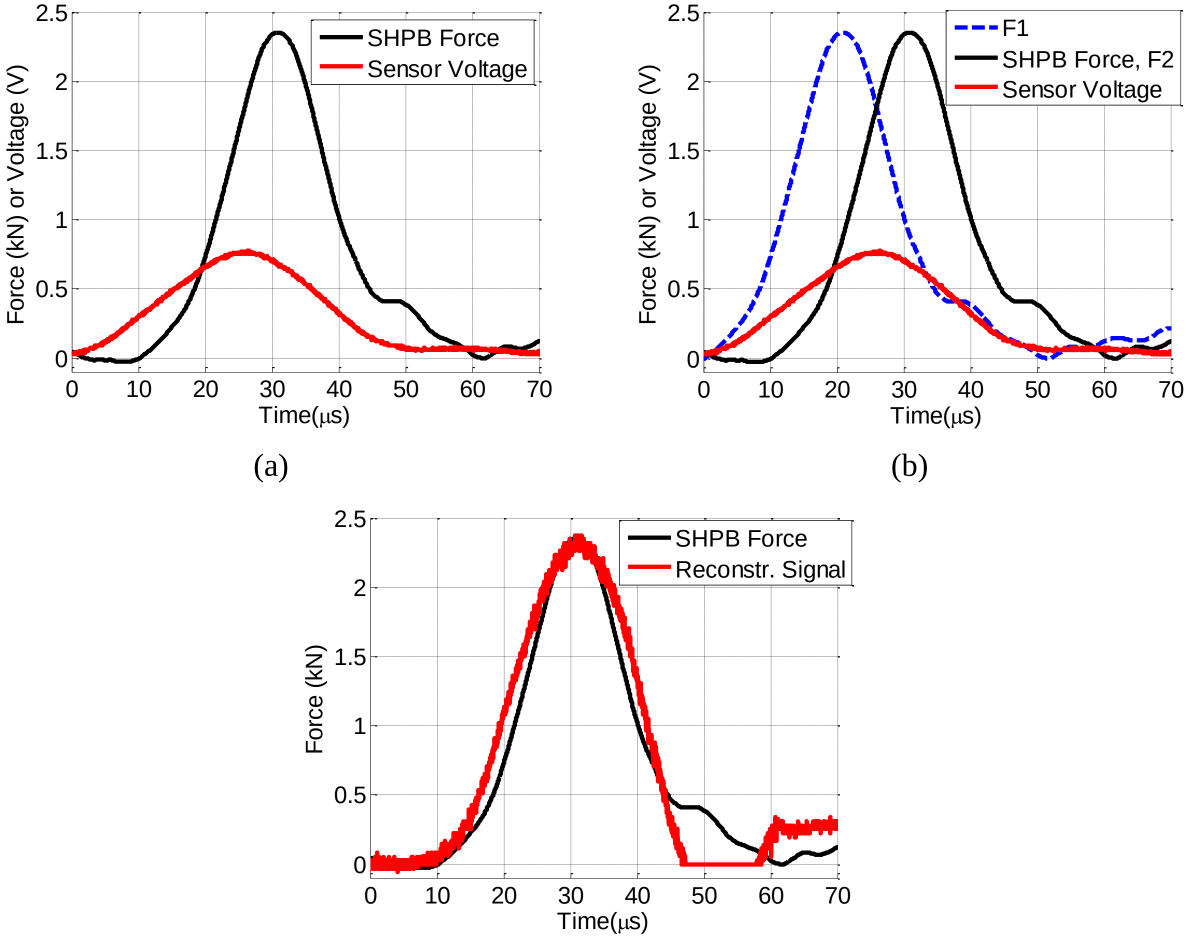

(a) (b)

(c)

Figure 2.8: (a) Determination of t_{step} by plotting the instrumented bead signal (red) and the transmitted bar signal (black). (b) The contact force F_1 (blue dashed line) can be plotted by shifting the contact force F_2 measured by the Hopkinson bar by the amount t_{step} since the sensor remains elastic. The peak voltage of the embedded sensor can then be calibrated at the point F_1 and F_2 coincide, which is 1.8 kN at $t = 26\ \mu s$. (c) The procedure for recreating the contact force from the average force shows good agreement with the contact force measured by the Hopkinson bar.

The above calibration procedure was repeated multiple times per sensor at different loads to establish a range of forces that could be measured by each sensor. Figure 2.9 shows the calibration curves from six typical sensors. A marker indicates the peak voltage in the sensor and the calculated contact force for one test. The markers for a given sensor are connected by a piecewise linear curve, with the slope of the curve being the calibration value. We note that the calibration value changes depending on the recorded voltage. For example, in calibration curve #4, the calibration value is different at a recorded voltage of 0.6 V than 1V. However, most of the calibration curves demonstrate linearity in Figure 2.9, although the slopes are different for each individual sensor.

The first few times the stainless steel instrumented bead was loaded against the Hopkinson bar, the bead yielded, due to the stress concentration at the granule/bar contact. The yielding is visible by eye and the yielded area could be quantified by analyzing an image from an optical microscope. Whenever yielding of the bead occurred, the calibration procedure could not proceed since the signal would not be repeatable. All of the stainless steel beads eventually became sufficiently work hardened that they would no longer yield; that is, inspection of the contact revealed no increase in yield area after an impact. The calibration curves in Figure 2.9 are from instrumented beads that remained elastic when loaded against the Hopkinson bar and allowed for repeatable results.

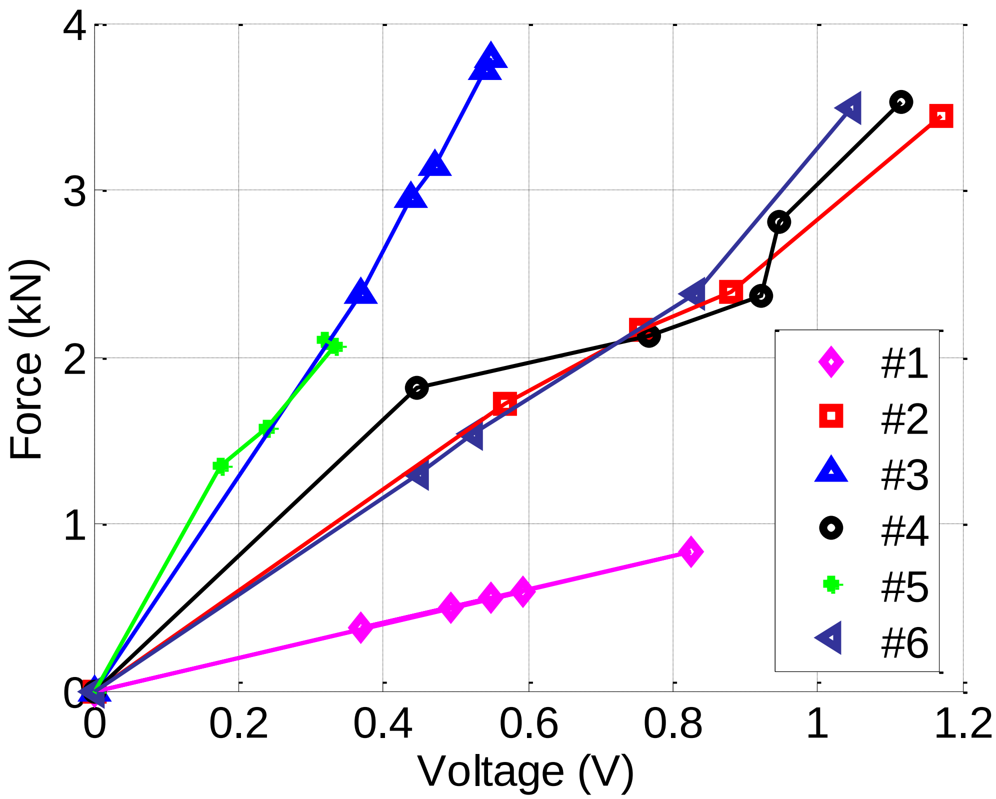

Figure 2.9: Typical calibration curves for 6 different instrumented beads. A marker indicates the peak voltage and force from one calibration experiment. Once several calibration tests are completed for a given sensor, the data points are connected piece-wise with lines. Then, for a given peak voltage from the instrumented bead, the local slope of the line provides the calibration value in kN/V.

3. 1D WAVE MANAGEMENT: ACOUSTIC SWITCH AND LOW-PASS FORCE FILTER

The design of mechanical analogues of electrical or optical systems, such as acoustic lenses [72] and acoustic switches [49], is an active area of research due to the potential that these new devices exhibit in areas such as non-destructive evaluation of materials and improved biomedical ultrasound imaging. This Chapter explores designs that can be considered as the mechanical equivalent of a switch and a low-pass filter.

3.1 Solitary Wave Switch

We first designed a mechanical switch that could easily be altered between two states: one that allowed solitary wave propagation and one that attenuated the solitary wave's amplitude. The system can alternatively be considered a "load diode" in that it allows unhindered solitary wave propagation in one direction, but attenuates the wave amplitude, potentially completely, when the wave travels in the opposite direction. The framework for the elastic wave tailoring in this design was based on changing the relative positions of granules, i.e., the lattice network, between two configurations. The results discussed here were published in [52] and the numerical results therein, and referred to below, are from our coauthors, Dr. R.K. Pal and Prof. P.H. Geubelle.

3.1.1 Operating principle: wave propagation in the lattice

The wave-tailoring lattice was arranged in a plane and wave propagation was considered in the axial direction only. Schematics of the two configurations of interest here are presented in Figure 3.1a-b for both side and top views. The lattice consisted of a 1D primary chain of "axial spheres" (red in Figure 3.1) that were aligned with the impact source, and a set of "side spheres" which were symmetrically placed on opposite sides of select axial spheres (blue in Figure 3.1). The blue spheres were placed at every other location simply for geometric reasons – to avoid direct contact of side spheres with each other. The side spheres were confined between two parallel plates. The lattice attained two states based on its inclination relative to the impact direction. In the *downstream* configuration shown in Figure 3.1a, the lattice was inclined such that a pair of side spheres were in contact with the adjacent downstream axial sphere (defined as the direction of primary pulse propagation) and a gap exists between the pair of side spheres and the axial sphere upstream. In the *upstream* configuration shown in Figure 3.1b, the lattice was inclined such that a gap existed between a pair of side spheres and its adjacent axial sphere in the downstream direction. Switching between the two configurations was easily achieved by slightly tilting the lattice in one of two ways in a gravitational field, as illustrated in the lower part of Figure 3.1a and Figure 3.1b. The effect of gravity on the lattice dynamics is negligible considering that only a small inclination (about 2° as will be seen in the subsequent experiments) was needed to keep each configuration stable. Thus the force due to gravity was about 4 orders of magnitude smaller than the magnitude of forces involved in wave propagation. However, gravity played a key role in providing a force sufficient to ensure stability of both configurations in their static assembly.

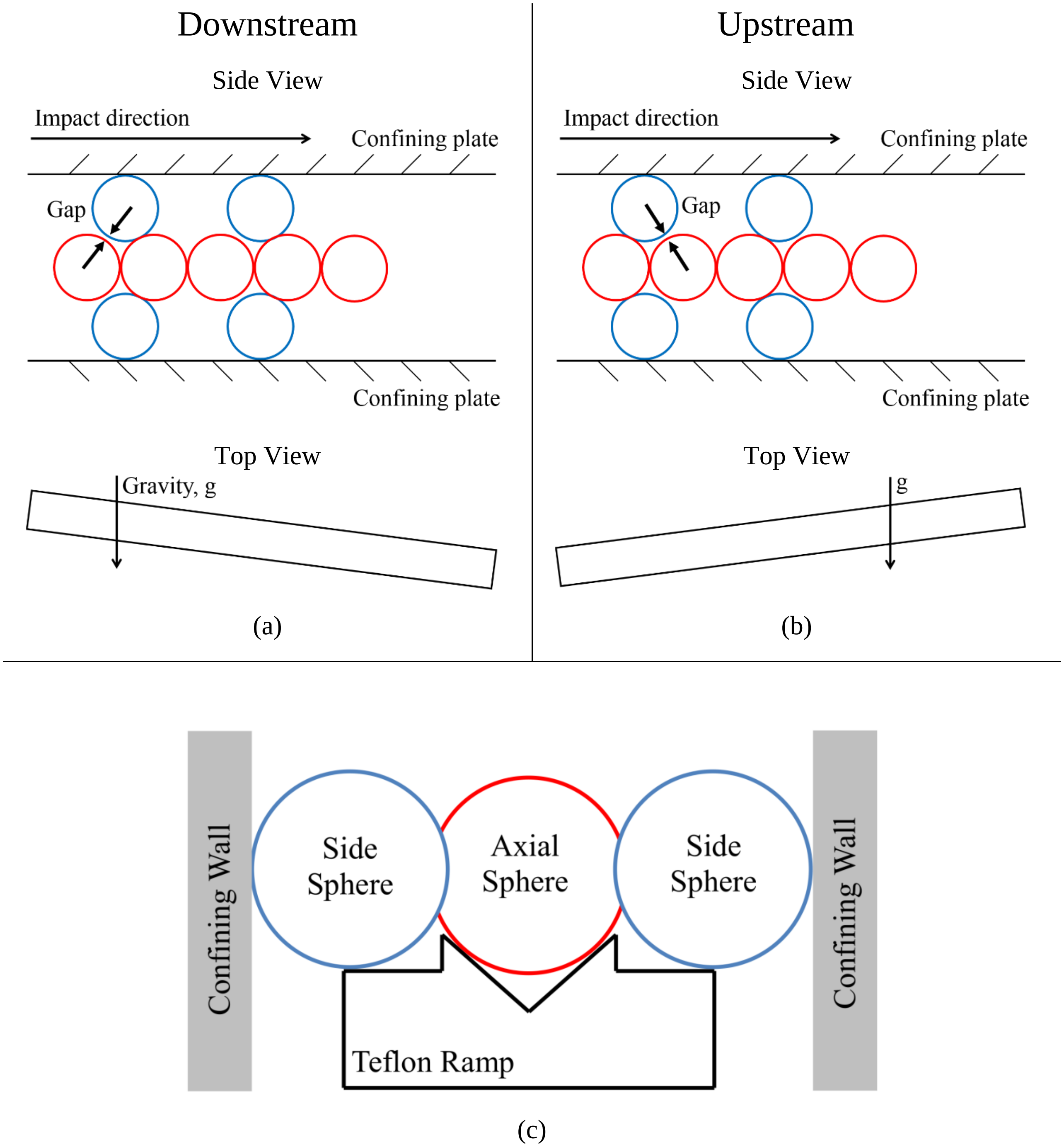

Figure 3.1: The network of spheres is arranged on an inclined ramp. Gravity alters the lattice network topology between: (a) the downstream configuration, in which side spheres (blue) only contact the adjacent downstream axial sphere (red), and (b) the upstream configuration. (c) Cross-sectional view of spheres resting on the Teflon ramp.

When the downstream configuration (Figure 3.1a) was impacted along the axial direction, a solitary wave propagated through the chain. The axial spheres moving forward did not contact the side spheres ahead as the wave propagated and the side spheres played no role in the dynamics of the lattice. In contrast, when the upstream configuration (Figure 3.1b) was subjected to the same impact, a wave with progressively decaying amplitude traversed through the lattice as the wave interacted both with the spheres along the axis and with the side spheres. After impact, the side spheres were in free flight and they eventually collided with the axial spheres adjacent to them in the downstream direction and there were local oscillations. The energy lost due to these local oscillations was similar to the oscillations observed in wave propagation through dimer lattices at the tail of the propagating wave where the smaller mass of a dimer unit cell may oscillate between two larger masses [31,51,103].

Due to symmetry, there was zero net force on the axial spheres in the lateral direction (vertical in side views of Figure 3.1a-b), and the spheres only moved axially. Note that the difference between the two configurations was in the location of the side spheres along the chain. The key aspect in the design was a change in lattice network topology, causing a change in the wave propagation behavior from a solitary wave to a rapidly decaying wave down the primary chain.

3.1.2 Experimental setup

The experimental setup consisted of axial spheres that were placed on a grooved PTFE holder ramp that both confined the axial spheres to move axially and reduced friction with the substrate. The side spheres were placed at the same horizontal level outside the groove and they were in contact with two parallel confining walls, as illustrated in Figure 3.1c. The PTFE holder ramp was located between and equidistant from the two confining walls. The symmetry of the holder ramp between the confining walls and gravity ensured that a given pair of side spheres was symmetrically situated with respect to the axial chain. The side spheres could move both axially and laterally within the confines of the parallel plates. The axial spheres were restrained from moving laterally as they were constrained by the groove and impacted only along the axis. Furthermore, the force due to the side spheres on the axial spheres was symmetric and hence the lateral component of force on the axial spheres was negligible. The inclination of the holder ramp is 2.2° which was sufficient to achieve the desired configurations while minimizing gravitational effects. The side spheres were in contact with the axial spheres, which held them in equilibrium in the axial direction. The contact force at equilibrium that balanced the weight of the side spheres was much smaller than the forces associated with the wave propagation and thus did not influence the dynamics of the spheres.

The axial and side spheres, obtained from Salem Specialty Ball Company, were made of 440C stainless steel and had a diameter of 9.53 mm, with material properties: Young's modulus 200 GPa, density 7670 kg/m^3 and Poisson's ratio 0.3. Figure 3.2, a close-up of the loading area of the set-up, shows that the Teflon holder rested between adjustable aluminum walls lined with steel inserts (the aluminum walls and steel inserts are the "confining walls" in Fig. 3.1c). The steel inserts were introduced to better match the rigid boundary conditions used in our collaborators' numerical simulation of the granular lattice. The steel inserts were in contact with two parallel plates. One of the parallel plates was fixed, while the position of the other plate could be adjusted by using a screw-driven mechanism. Pairs of side spheres were symmetrically placed along the sides of the primary chain such that each side sphere was in contact with one axial sphere from the primary chain and a sidewall. The primary chain was impacted by a sphere identical to the axial and side spheres released from a consistent height from an input ramp, seen in the left part of Figure 3.2. The impact velocity of this sphere onto the first axial sphere was determined from the delay between the disruption of infrared light from two infrared emitters (also seen in Figure 3.2). An impact velocity of 0.62±0.015 m/s, low enough to ensure elastic deformations throughout, was used in all experiments discussed in Section 3.1.

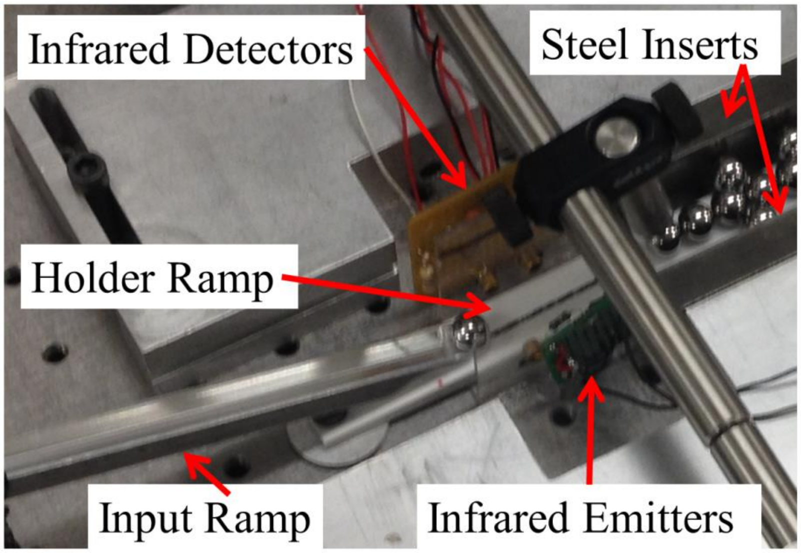

Figure 3.2: Close-up of the loading area of the set-up illustrating loading ramp, infrared-based velocity measurement system, and confining steel walls.

Figure 3.3 shows the experimental downstream configuration, where the holder ramp was inclined (again at 2.2°) in the opposite direction such that the side spheres were in contact with only the downstream axial spheres. The axial chain was comprised of 21 total spheres and a sphere with an embedded piezoelectric sensor was placed at the axial location of the 18th sphere (Figure 3.3b) to read the reaction force generated in each case. The instrumented bead was manufactured as discussed in Section 2.3.2 and calibrated as in [18,102].The peak force at the 18th sphere was then recorded 10 times for each tested configuration of 0, 3, and 5 sphere side pairs.

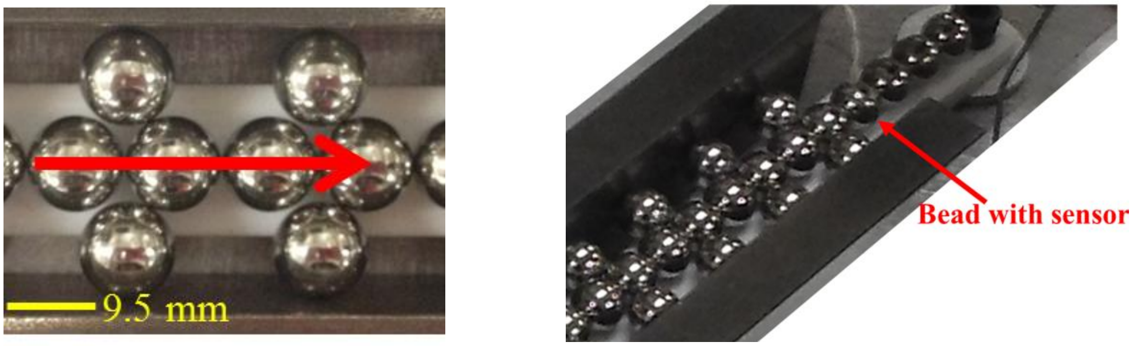

(a) (b)

Figure 3.3: Downstream configuration. (a) The red line indicates the direction of wave propagation through two unit cells. The lateral beads are only in contact with the downstream lateral beads. (b) Embedded sensor at the end of the chain to measure the solitary wave profile; additional beads are placed between the instrumented bead and the support to reduce interference from reflections.

Figure 3.4 shows photographs from the experimental upstream configuration, in which the side spheres were only in contact with the upstream sphere of the primary chain. The impacting velocity was again 0.62±0.015 m/s in all experiments. The upstream configuration was composed of 18 axial spheres which were stopped from sliding along the incline by a steel support (Figure 3.4b) that was situated such that it did not interfere with the impact between the impacting sphere and the first sphere of the primary chain. Infrared detectors were placed at the end of the primary chain (Figure 3.4c) to capture the departing (output) velocity of the last axial sphere in the primary chain. By comparing this output velocity with the input velocity, the solitary wave decay was quantified. Note that it was not possible to capture the output velocity in the downstream configuration (as the motion of the last sphere was constrained for static equilibrium before impact). In this upstream configuration, 20 experiments were completed each for 0, 1, 2, 3, 4, and 5 side sphere pairs.

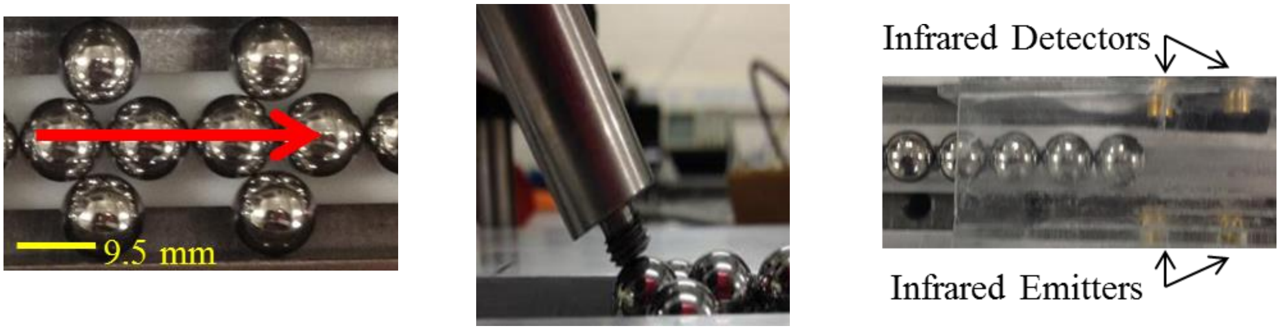

(a) (b) (c)

Figure 3.4: Upstream configuration. (a) Two unit cells, with the red line indicating the direction of wave propagation. Note that the lateral beads are only in contact with the upstream primary chain beads. (b) Steel support that prevents the chain from rolling. (c) Infrared detectors at the end of the chain that are used to measure the output velocity.

3.1.3 Results and discussion

Experiments were conducted on both configurations to demonstrate the concept of a solitary wave switch. The experiments were repeated for various numbers of pairs of side spheres, while the input velocity was kept fixed at 0.62±0.015 m/s. Figure 3.5 illustrates the experimental data for the velocity of the final sphere, normalized with the velocity of the impacting sphere, for the upstream configuration. The horizontal axis shows the number of side pairs in the setup and the vertical axis shows the set of normalized velocities. The decrease in the output velocity for the zero side sphere case was due to the fact that the impact energy was initially localized in the impacting bead and the first axial bead, while the energy associated with the solitary wave was distributed over 5 particle diameters [15]. The experimental data for each set of pairs of side spheres are in good agreement, demonstrating the repeatability of the experiment. Figure 3.6 plots the numerically simulated force history at the 18th sphere for different numbers of side pairs and shows the progressive decay of the wave amplitude with increasing number of pairs of side spheres. Further numerical investigations verified that the amplitude decay was due to energy being transferred from the axial spheres to the side spheres [52].

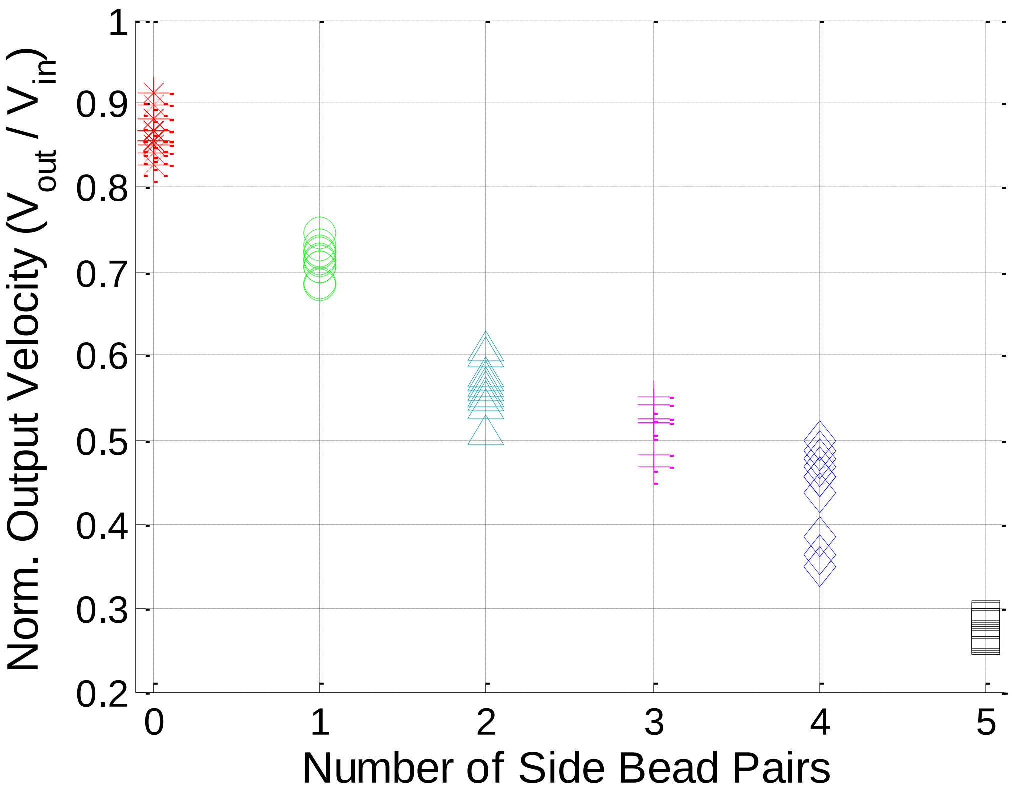

Figure 3.5: Upstream configuration. The normalized output velocity decreases rapidly with increasing side pairs.

Experimental factors that contributed to scatter included friction among the spheres and between the side spheres and the wall, the variable input velocity (0.62±0.015 m/s), and slight misalignments that could not be detected by eye which may arise from the non-uniform sphere diameter (tolerance: ± 0.0127 mm).

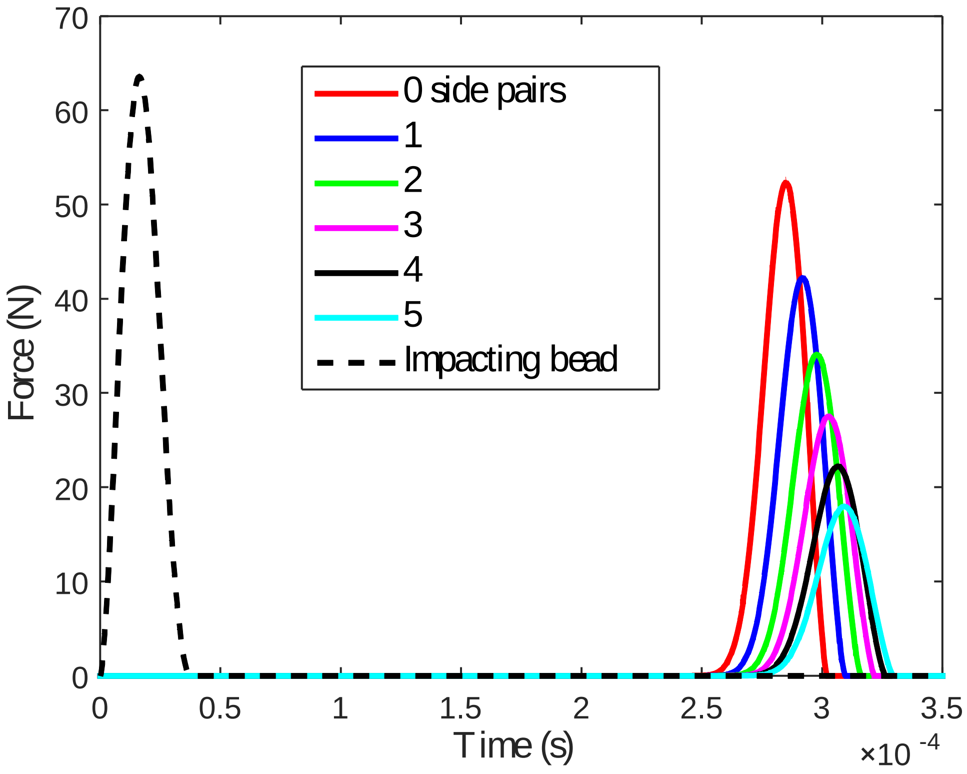

Figure 3.6: Numerical simulations showing that force amplitude at the 18th sphere decays with an increase in the number of side spheres in the upstream configuration [52].

Figure 3.7a shows the force histories at the same axial sphere (#18) for different numbers of side sphere pairs when the chain is in the downstream configuration and Figure 3.7b summarizes the peak force values. The peak amplitude of the solitary wave was 52 N, which was below the yield force of 68 N, calculated from Eq. (1.4), of the stainless steel spheres used in this work. In the downstream configuration, a solitary wave propagated down the chain independent of the number of pairs of side spheres, a result that is verified numerically in Figure 3.8. The axial spheres did not interact with the side spheres as their displacement toward the impact direction was about 13 μm (numerically calculated), which was much less than the gap between them and the side spheres. The dynamics in the downstream configuration were thus identical to a solitary wave traversing in a monodisperse chain.

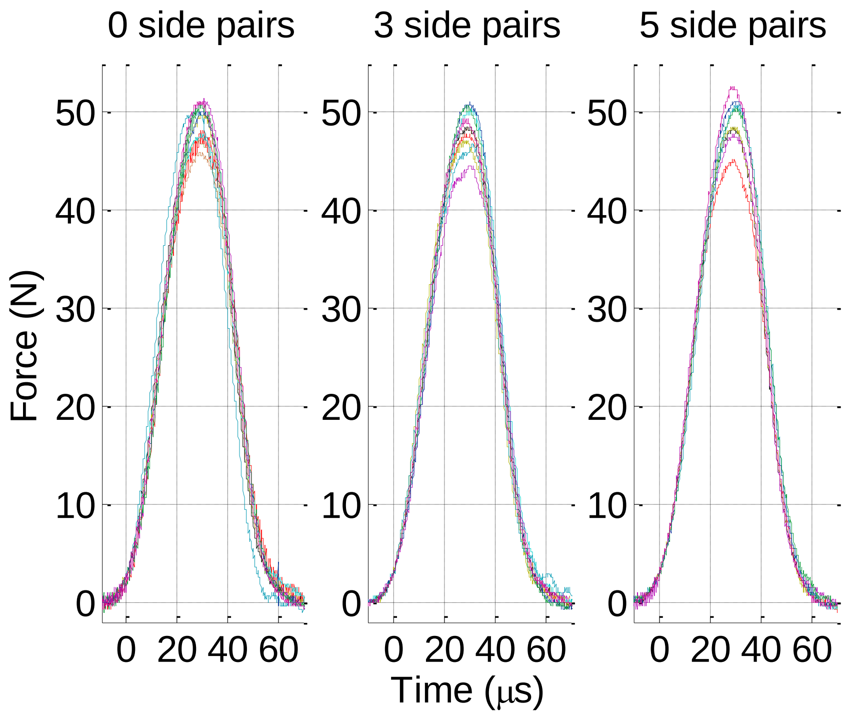

(a)

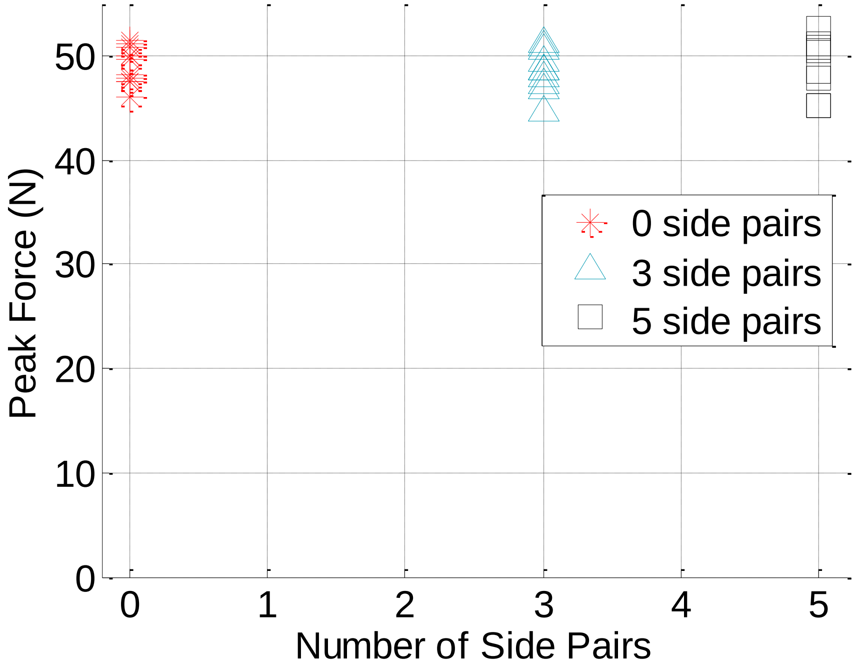

(b)

Figure 3.7: Peak force values experienced at the 18th bead are constant regardless of the number of side pairs in the downstream configuration. (a) Force profiles from the instrumented beads for the case of the 0, 3, and 5 side pairs. (b) Summary of the peak forces for 0, 3, and 5 side pairs.

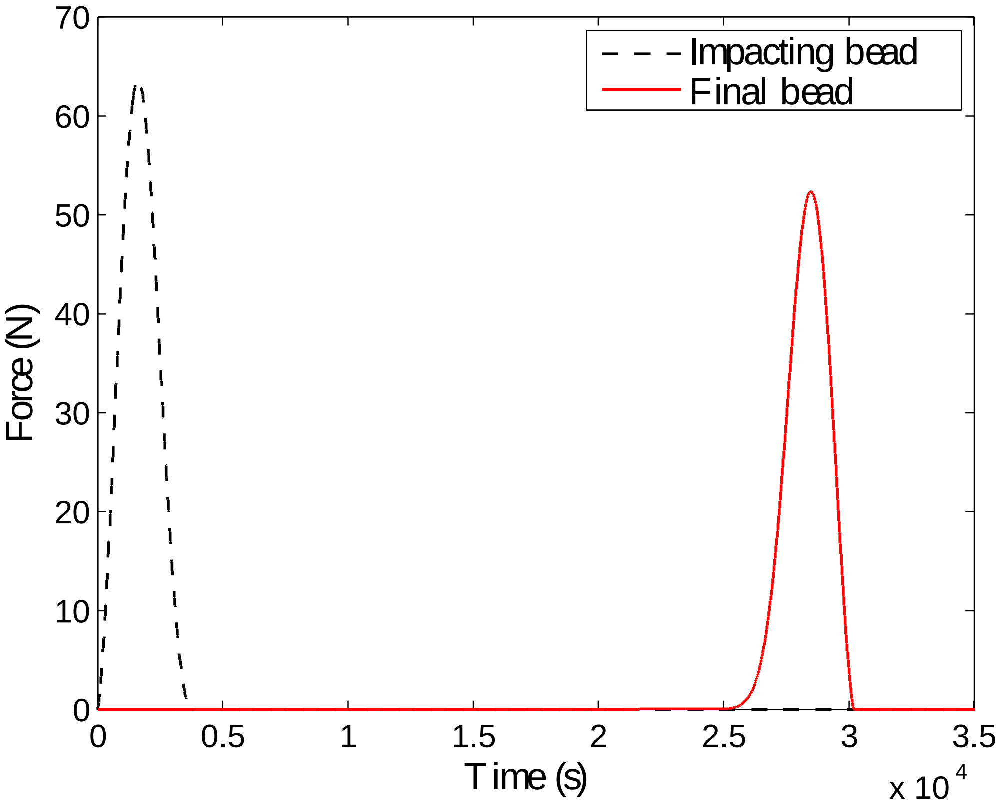

Figure 3.8: Numerical simulations showing the force at the 18th sphere is unchanged regardless of the number of side pairs in the downstream configuration [52].

Figure 3.5Figure 3.8demonstrate that the behavior of the lattice was significantly different between the upstream and downstream configurations, thus validating the proposed design of a solitary wave switch that is triggered by altering the lattice network topology. Solitary waves form in the regions after the side spheres and they are non-dispersive; thus the trends displayed here do not vary as the quantity of axial spheres is increased. Furthermore, note that an upstream configuration in one direction is identical to the downstream configuration for a wave travelling in the opposite direction. Indeed, there are two ways of looking at our system: as a device that permits higher amplitude propagation in one direction than the other ("load diode") and as a switch. The downhill configuration endeavors to realize a closed circuit and transforming to the uphill configuration corresponds to an open circuit. Thus, the mechanism to alter between configurations can be viewed as a device for the management of mechanical impulses.

In conclusion, the proposed framework was validated by experimental measurements and numerical simulations. In the upstream configuration, the primary wave amplitude decreased along the chain due to the presence of side spheres, while in the downstream configuration, a (fixed-amplitude) solitary wave propagated along the chain. Energy “leaking” via the side spheres was responsible for the amplitude decay in the upstream configuration and thus the more side pairs were present the more significant the decay. With 5 side pairs a decay of about 70% was achieved and almost complete extinction would be possible with the addition of more side pairs. Furthermore, since a given side pair may be placed adjacent to any axial sphere and the side pairs may be placed nonconsecutively, it is possible to tailor regions with different solitary wave properties within a granular lattice. In practice, switching between the two configurations, decaying and steady, can be done by exploiting gravity and tilting the primary chain in one or the other direction. This framework of altering the lattice network topology, in this case by gravity, can clearly be extended to alternate designs and more complex mechanisms. The device presented here can also be used either as a one way propagation device or as a logic element in a mechanical circuit. The work demonstrates the potential to develop a family of devices for wave tailoring using granular crystals.

3.2 Low-pass Force Filter

3.2.1 Operating principle: filtering via preconditioned contacts

Preconditioning, first discussed in Section 1.2.3, enables the propagation of high amplitude solitary waves since the contacts have been treated to sustain up to a given amount of loading elastically [90]. By incorporating preconditioning into 1D chains of beads it is possible to taper or filter the amplitude of the nonlinear wave. Dr. A. Awasthi, a collaborator to this effort and of the preconditioning concept [90], conducted simulations to show that chains of beads with varying levels of preconditioning can act as a low pass force filter for high-amplitude (kN range) solitary waves. The fundamental idea is that the maximum amplitude of the solitary wave that emerges from a 1D granular chain is limited by the section of the chain that has the lowest preconditioning level. The limiting effect of the lowest preconditioned beads is due to the plastic dissipation that would otherwise occur at the contacts, provided the chain was long enough. In the limit of a long bead chain, the wave would continue to decay until only an elastic wave is propagating. (Note we are referring here to filtering of the *maximum force level*, not the frequency content of the wave, hence the term “force filter”.) Figure 3.9 illustrates the low-pass force filtering of an incoming solitary wave with amplitude 15 kN. The filter in Figure 3.9a consists of a chain of beads whose contacts have been preconditioned to 9 kN (the filter portion is highlighted by a purple box in Figure 3.9). When reaching the 9 kN preconditioned beads the 15 kN solitary wave will attenuate until the amplitude is 9 kN, at which point the wave will continue to propagate through the chain elastically. Similarly, for a sufficiently long filter, the 15 kN solitary wave would be reduced to a 5 kN solitary wave if the contacts within the filter are preconditioned at 5 kN, as in Figure 3.9b. Finally, the limiting case would be if the filter contains no preconditioned contacts. In this limiting case, the amplitude of the incoming solitary wave would be diminished to the elastic limit of the bead contact points. For a brass bead with a diameter 9.5 mm, that limit would be 0.126 kN, shown in Figure 3.9c. If the amplitude of the incoming solitary wave is below the preconditioning level of the filter, then the solitary wave will pass through the filter without any amplitude attenuation as shown schematically in Figure 3.10 for the case of a 5 kN solitary wave passing through a filter containing 9 kN preconditioned contacts.

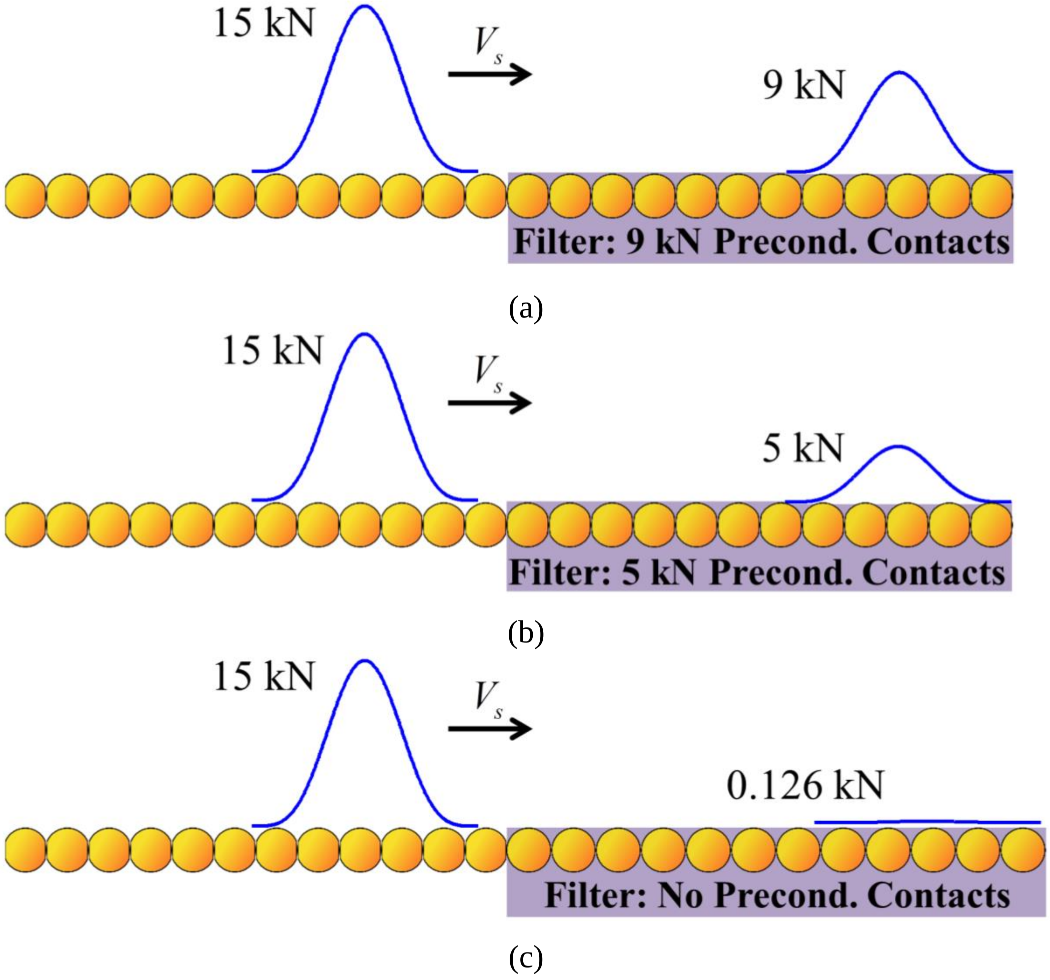

Figure 3.9: Schematic illustrating that the preconditioning level of the filter controls the output force amplitude if the incoming solitary wave has larger amplitude than the filter preconditioning level. The filter is portion is emphasized by the purple box. A solitary wave with a 15 kN amplitude is reduced to (a) 9 kN, (b) 5 kN, and in the case of no preconditioning, 0.126 kN – the elastic limit of the brass.

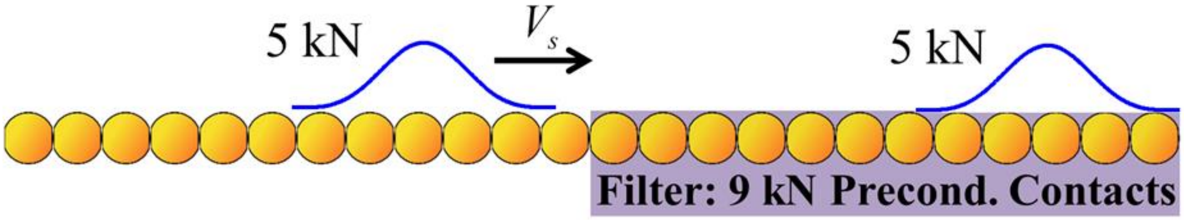

Figure 3.10: Schematic illustration of a solitary wave passing through a filter without attenuation if its peak force is lower than the preconditioning level of the filter.

3.2.2 Experimental setup

Motivated by this, a 1D granular system was constructed to experimentally explore the filtering concept. The experimental setup accommodated a 1D granular chain in which all beads were made of the same rate-insensitive material, brass 260, with the material properties described in Section 2.1. The beads were preconditioned by placing them in a quasi-static load frame and compressing them to the desired load level such that the two diametrically opposite contacts were preconditioned to the same level and then unloaded and removed from the load frame (Figure 1.10 in Section 1.2.3 demonstrates the preconditioning procedure). Figure 3.11 shows a close-up of a brass bead that has been preconditioned to 9 kN. While the preconditioned contact may appear flat, the contact retains curvature as shown by profilometry measurements in [90].

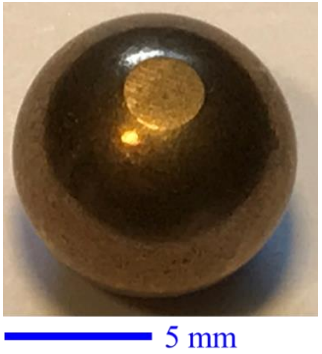

Figure 3.11: Brass bead preconditioned to 9 kN. The diametrically opposite side (not visible in the photograph) is also preconditioned to 9 kN.

The system, shown in Figure 3.12a, was loaded using the configuration described in Section 2.2, whereby a maraging steel Hopkinson bar impacted the 1D granular chain in a custom-built load frame via an impedance-matched tungsten carbide (WC) adapter bar. The load frame was modified to accommodate a 1D chain by pushing the lateral walls closer together using the adjustable screws. The two lateral walls were replaced with shorter walls, wrapped in PTFE and visible in Figure 3.12b-c, facilitating easier alignment of the preconditioned contacts in the 1D chain. Following the granular chain was an aluminum transmitted bar that allowed the granular chain to move parallel to the loading direction after being impacted. The aluminum transmitted bar entered the load frame through a hole in the rear wall, similar to the hole that permitted the adapter bar.

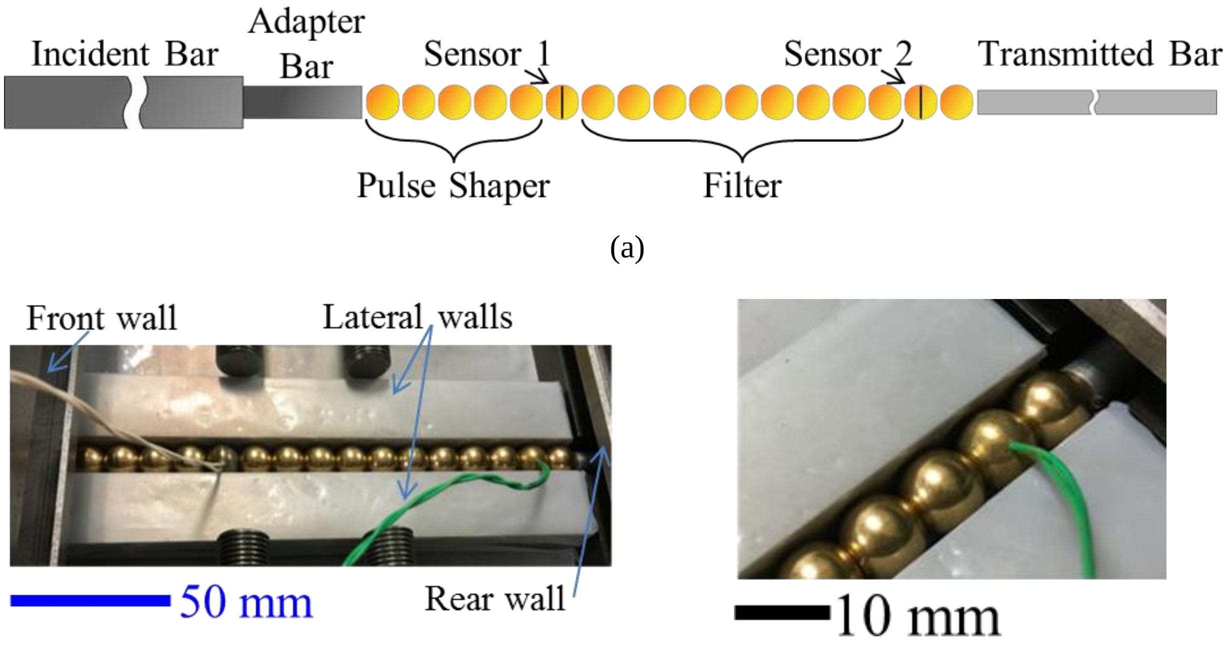

(a)

(b)

(c)

Figure 3.12: Experimental setup of low-pass force filter. (a) Schematic illustrating the main components of the low-pass force filter. (b) A photograph of the setup. (c) Close-up of the rear section of the filter showing the preconditioned contacts, Sensor 2, and the aluminum transmitted bar.

The first section of the chain, denoted as “pulse shaper” in Figure 3.12a, consisted of beads that have been preconditioned to 21 kN and allow a high amplitude solitary wave to form. The pulse shaper was necessary since a solitary wave requires five beads to form [15]. The solitary wave was subsequently detected by an instrumented bead, denoted as Sensor 1 in Figure 3.12a. After the wave passed through a filter with some preconditioning level, it was detected at another sensor, Sensor 2. In contrast to the other Chapters in this work, the piezoceramic sensors were embedded in brass, instead of stainless steel, beads to reduce the effect of a material mismatch in the chain. Figure 3.13 shows a brass bead that was preconditioned to 21 kN and loaded (at a level below 21 kN) adjacent to a stainless steel bead. A large dimple is evident in the preconditioned contact. Thus, using a stainless steel instrumented bead at the Sensor 1 location would be detrimental to demonstrating the low-pass force capabilities of the preconditioned contacts in the chain since a portion of the input load coming out of the pulse shaper would be immediately lost at the contact between the last bead of the pulse shaper and the stainless steel Sensor 1.

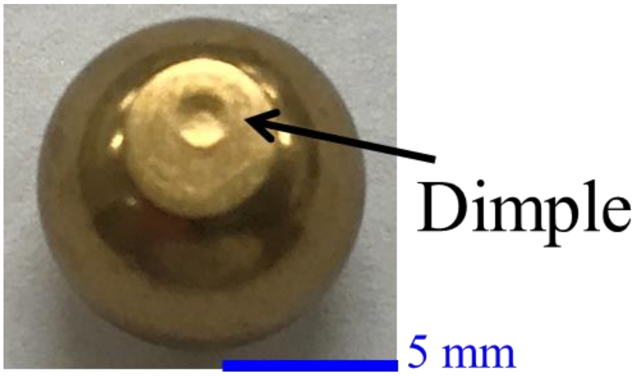

Figure 3.13: Evidence of yielding when an instrumented stainless steel bead is used in the filter.

In order for the instrumented brass bead to remain elastic, it was necessary to precondition the contacts. Thus, prior to instrumented bead assembly, each machined hemisphere was placed in a quasi-static load frame and preconditioned to the desired load – 21 kN. In order to prevent the machined hemisphere from plastically bending, a stainless steel cylinder was placed in the region that has been cut-out to accommodate the piezoceramic disk, as shown in Figure 3.14. After each hemisphere was preconditioned, the piezoelectric disk with attached lead wires was placed into the machined groove and the instrumented bead was assembled with polyurethane, identical to the procedure discussed in Section 2.3.2. The calibration also proceeded as in Section 2.3.3, where the preconditioned instrumented bead was placed in contact with the Hopkinson bar and had two brass beads immediately preceding it, as shown in Figure 3.15. A fourth brass bead was launched at the short chain. The voltage recorded in the instrumented brass bead was then converted to force using the procedure discussed in Section 2.3.3. The preconditioned instrumented bead did not yield on either side during the calibration procedure as there are no dimples and the yield area remained constant.

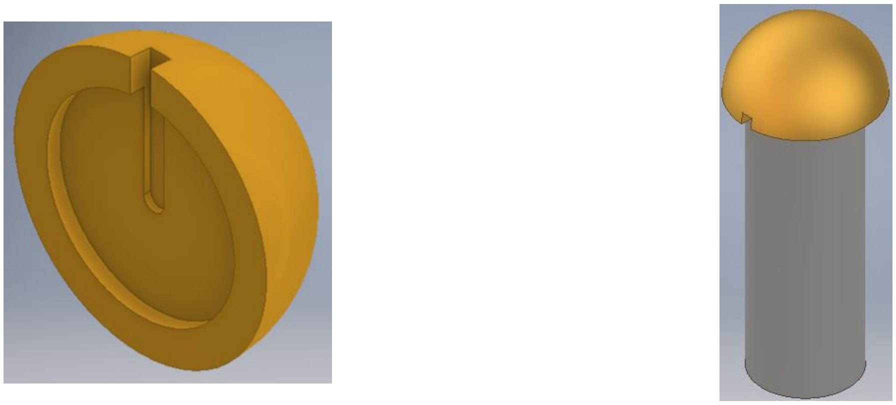

(a) (b)

Figure 3.14: (a) Model of a brass hemisphere that has been machined to accommodate a piezoceramic sensor. (b) A stainless steel cylinder is placed within the cut-out region of the hemisphere prior to preconditioning. The presence of the stiff cylinder prevents the cut-out region from plastically bending during compression. Note that both hemispheres that encapsulate the piezoceramic disk are preconditioned in this manner.

Figure 3.15: Calibration setup of preconditioned instrumented bead.

3.2.3 Results and discussion

The wave amplitude was selectively filtered by controlling the preconditioning levels of the filter for two input loads – 15 kN and 33 kN. First, we investigated a 15 kN load that travelled through a filter that consisted of beads that were uniformly preconditioned at 21 kN. Figure 3.16 shows the force profile that enters the filter, as detected by Sensor 1 (see Figure 3.12 for labels) and the force profile at the end of the filter, detected by Sensor 2 for three nominally identical experiments. Since the input load was below the preconditioning level, we expected no yielding to occur; however, Figure 3.16 shows that a minor (~5% on average) decrease in the wave amplitude occurred between Sensor 1 and Sensor 2. The wave attenuation was in part due to slight misalignments among any of the pairs of preconditioned contacts and friction amongst the particles and between the particles and load frame. We also note that the second peak in the Sensor 2 readings was due to reflections from the end of the chain.

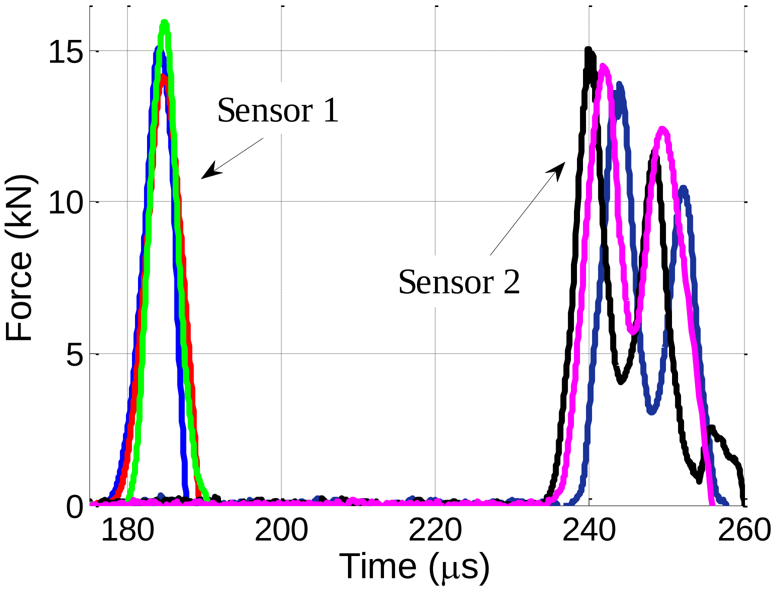

Figure 3.16: Input and output loads for a uniformly preconditioned 21 kN chain loaded at 15 kN. Sensor 1 detects the force profile that enters the filter and Sensor 2 detects the output signals. The force profiles from three distinct, nominally identical tests are shown to establish the scatter.

Next, we investigated the output loads in a filter, again uniformly preconditioned to 21 kN, for an input load of ~33 kN. Figure 3.17 shows the results from three nominally identical experiments to show the scatter in the input loads (Sensor 1) and output loads (Sensor 2). The average value of the maximum load experienced at Sensor 2 was 29 kN, which was 12% less than the load at Sensor 1. The amplitude of the wave at Sensor 2 was expected to match the lowest degree of preconditioning present in the filter (here, 21 kN) when the input load was higher than the preconditioning level. However, the design of the load frame was such that it could only accommodate 17 beads arranged in a 1D chain and the consequence of this design limitation was that the waves have less time to dissipate to the expected amplitudes. Thus, to completely filter the 33 kN input load, the load frame would need to be redesigned to accommodate a longer chain. Note, as the chain length increases, there is an increased likelihood of a misalignment between preconditioned contacts, which effectively decreases the preconditioning level of that contact to the limit that it would appear as if no preconditioning occurred.

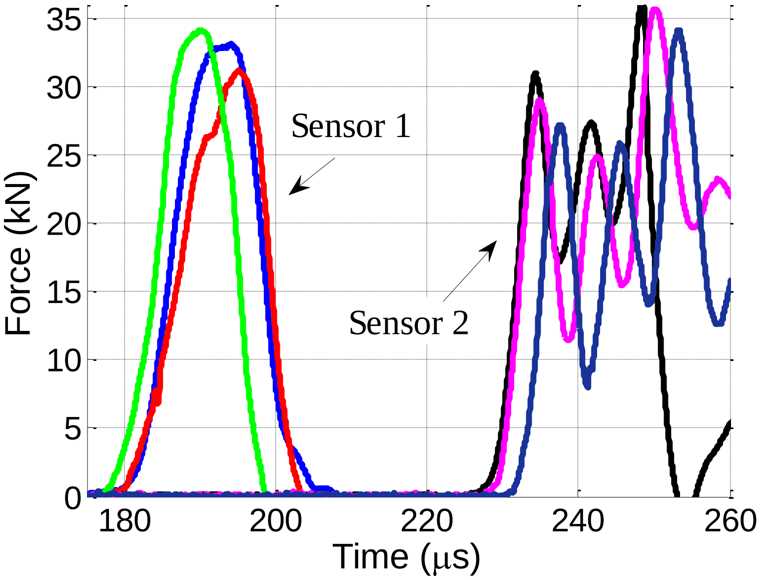

Figure 3.17: Input and output loads for a uniformly preconditioned 21 kN chain loaded at 33 kN. Sensor 1 detects the force profile that enters the filter and Sensor 2 detects the output signals. The force profiles from three distinct, nominally identical tests are shown to establish the scatter.

Non-uniform filter

In addition to the uniform 21 kN filter, other configurations were investigated that had two distinct preconditioning levels. In the non-uniformly preconditioned filter setup, the first four beads were preconditioned to one level while the next five beads were preconditioned to a different, lower level. A sample result is shown in Figure 3.18, in which a 21 kN – 5 kN filter (i.e., first four beads of the filter were preconditioned to 21 kN and the last five beads were preconditioned to 5 kN) reduced the 15 kN input load to 5.5 kN. The filter was nearly successful in that it reduced the input load to about the lowest preconditioning level (5 kN). We note that the Sensor 2 signal in Figure 3.18 arrived later than the Sensor 2 signal in Figure 3.16 since the wave amplitude was lower due to the plastic dissipation occurring at the 5 kN-preconditioned contacts. The plasticity also resulted in trailing waves in the Sensor 2 reading in Figure 3.18 (along with reflections).

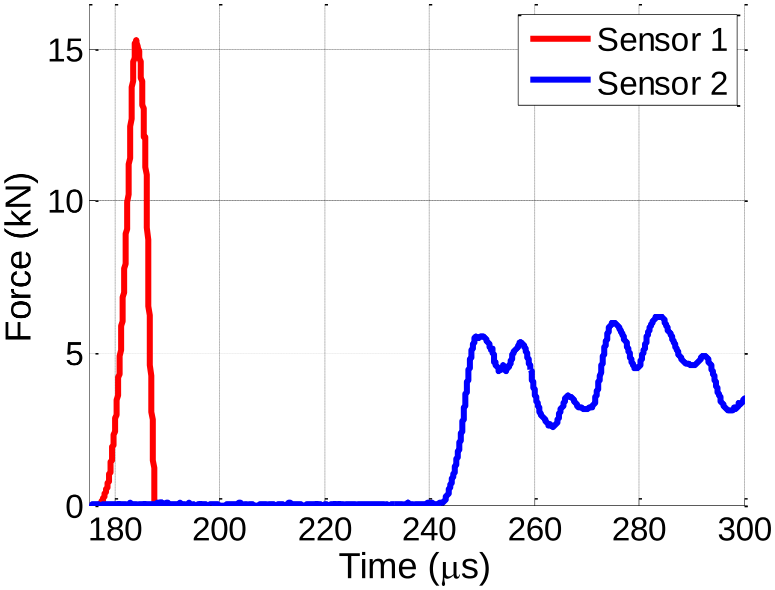

Figure 3.18: Input and output load for a 21 kN – 5 kN filter.

We investigated additional filter configurations for the 15±1 kN input load and summarize the peak forces experienced at the Sensor 2 location inFigure 3.19. The scatter bars indicate the scatter from three tests for each of the filter configurations. At the 21 kN- 9 kN filter level, the transmitted load was reduced to about 10 kN, which is close to the expected output of 9 kN, indicating that 6 contacts were sufficient to reduce the wave amplitude from to ~10 kN. However the shortness of the chain again caused larger-than-expected transmitted force amplitudes for the 21 kN- 5 kN filter. Finally, the case of no preconditioning demonstrated that the lower limit for the transmitted load amplitude for the given input load was about 800 N (rather than the predicted 126 N).

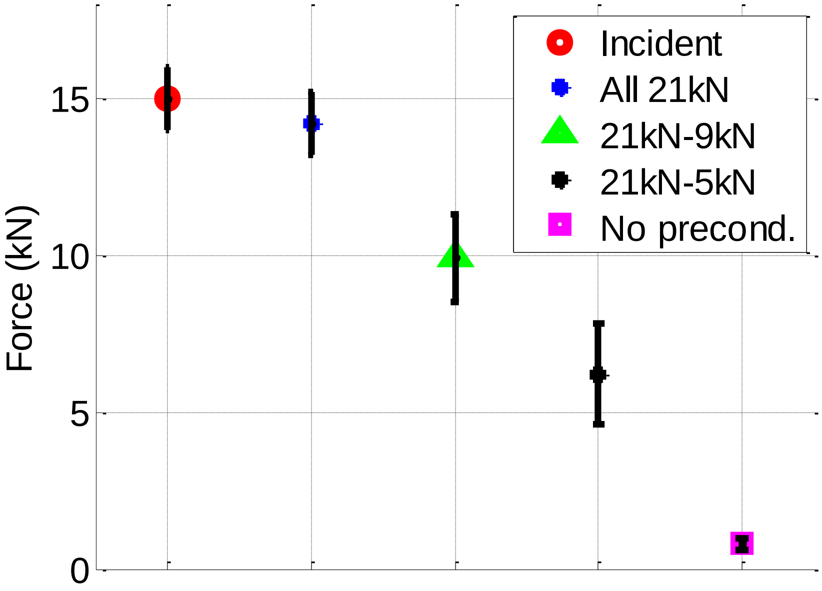

Figure 3.19: Scatter in incident force recorded at Sensor 1 (red circle) and transmitted forces recorded at Sensor 2 for different filter configurations for 15 kN loading.

Figure 3.20 shows similar results from a series of experiments in which the input load (denoted by the red circle) was 33±2 kN. The remaining markers in Figure 3.20 show the average peak force load – from four tests at each filter configuration – that was recorded by Sensor 2 at the end of the filter and the error bar indicates that scatter that was present in that set of experiments. Since the preconditioning level of all the filters was below the wave amplitude of the input force, the wave amplitude attenuated due to plastic dissipation at the contacts. As the preconditioning level decreased, a corresponding decrease was observed in the output load at Sensor 2, with the lowest output load occurring at the limit that all of the beads of the filter were not preconditioned (magenta square).

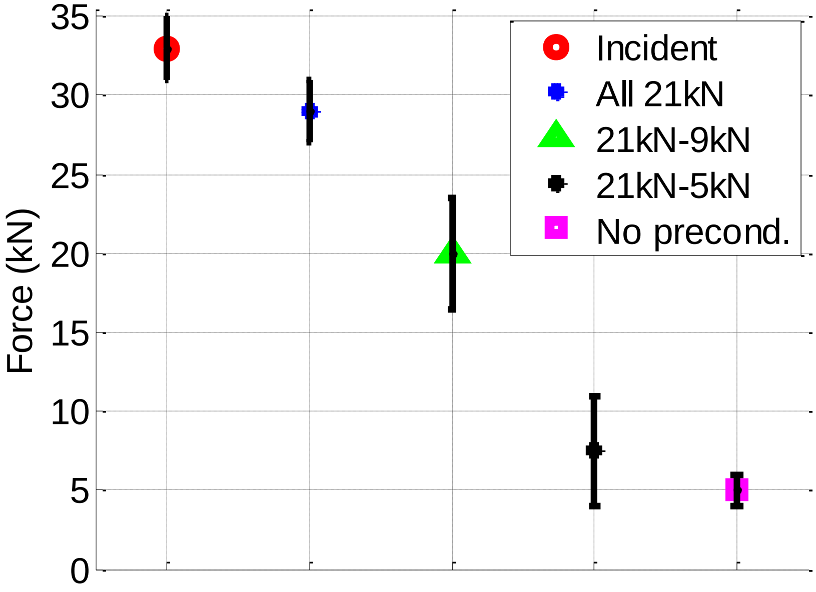

Figure 3.20: Low-pass force filter results from 33±2 kN loading. Scatter in incident force recorded at Sensor 1 (red circle) and transmitted forces recorded at Sensor 2 for different filter configurations.

4. WAVE PROPAGATION IN 2D ELASTO-PLASTIC GRANULAR MEDIA

Elasto-plastic studies in 2D and 3D ordered granular systems are limited due to the need for appropriate elasto-plastic contact models and the technical difficulties associated with any experimental methodology. Here, we extend the 1D experimental work of [82,83] to 2D with the goal of establishing an understanding of the complicated wave behavior in elasto-plastic 2D ordered systems and also of helping validate reliable numerical frameworks for granular material design. The work presented in this Chapter was accepted for publication in [88].

Our experimental study on 2D ordered packings focused on three tasks: (i) to generate a controllable stress pulse in a 2D granular packing while implementing in situ force measurements, (ii) to study the stress wave propagation and plasticity propagation pattern in the packing, and (iii) to compare the experimental results to a numerical simulation framework (assembled by our collaborators) which has an appropriate contact model for contacting ductile granules.

4.1 Experimental Setup

The experimental setup was similar to the one discussed in Chapter 2 and is illustrated in Figure 2.1. Beads made of rate-independent [76] brass alloy 260 (diameter, $d = 9.53\,\text{mm}$) were placed in the aforementioned load frame and loaded with a Hopkinson bar. A lead pulse shaper was present at the striker-incident bar interface to smooth the profile of the compressive stress pulse by decreasing the rise and fall times of the loading pulse [104]. The significant difference here was that the adapter bar was made of stainless steel ($d = 6.35\,\text{mm}$, $l = 76.4\ \text{mm}$) and was not impedance matched to the incident bar [14]. Thus, the strain gages on the incident bar only allowed for the calculation of the load input into the adapter bar, rather than the granular packing. Stainless steel 440C beads with embedded piezoelectric sensors helped determine the evolution of stress waves as they travelled through the granular array by enabling knowledge of the loads and arrival times at certain locations.

The brass beads were manually arranged into one of two 2D packing configurations – square or hexagonal – as shown in Figure 4.1. The beads in both packings were horizontally arranged (i.e., in a plane parallel to the ground) which eliminated any gravitational effects. The square packing was composed of a 10 bead by 10 bead arrangement while the hexagonal packing contained 11 rows in which the first row (the row closest to impact) contained 10 beads and subsequent rows alternated between 9 and 10 beads. A loading bead was symmetrically placed in contact with the 5th and 6th beads of the first row. The loading bead helped to minimize any misalignment effects of directly loading the granular packing with the incident bar of the Hopkinson bar device. Finally, the beads were numbered using a permanent felt tip marker so their location in the array could be identified during postmortem analysis.

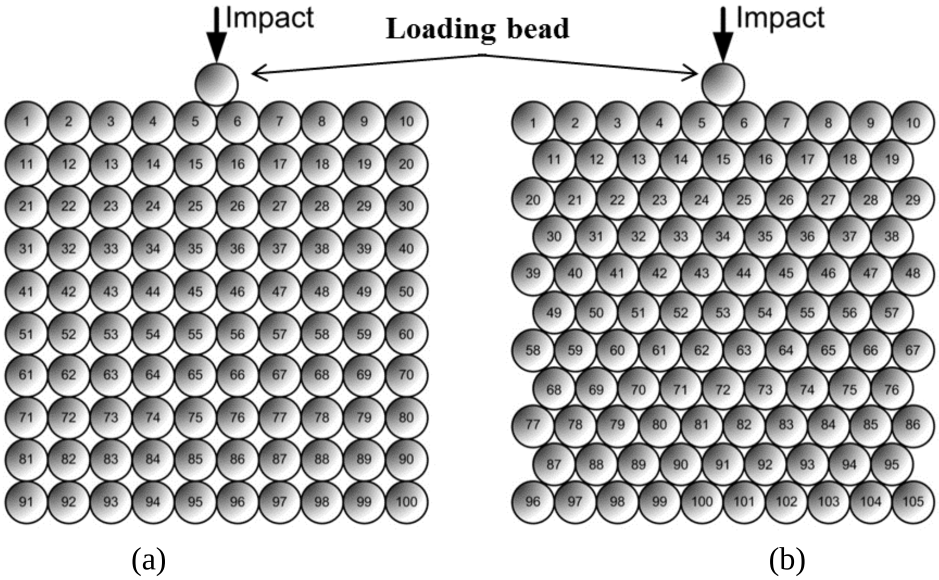

Figure 4.1: The brass beads arranged horizontally in (a) a 10 x 10 square packing and (b) a hexagonal packing with alternating rows of 10 and 9 beads. The impact occurs at a symmetrically placed loading bead.

After impact, the force on the adapter bar was measured by summing the incident and reflected pulses recorded by the strain gages. A typical example of a signal recorded by the strain gages (and converted from voltage to force using the relations given in Section 2.2) in these experiments is shown in Figure 4.2.

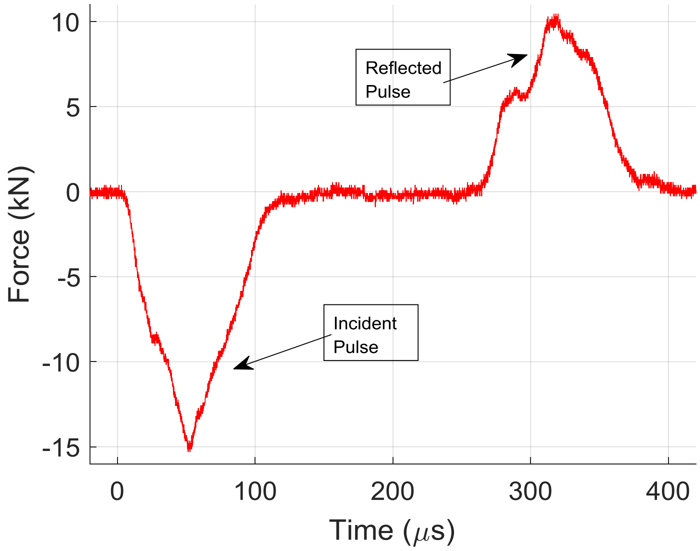

Figure 4.2: Typical incident and reflected pulse measured by the strain gages.

A given granular packing was subjected to one of three typical input forces, labeled as high, medium, and low, and shown in Figure 4.3. After each loading, the hexagonal packing was reconstituted using a different set of beads. Note that the input load was on the order of kNs, which is much higher than the 126 N elastic limit calculated in Section 1.2.3 for the brass beads used here.

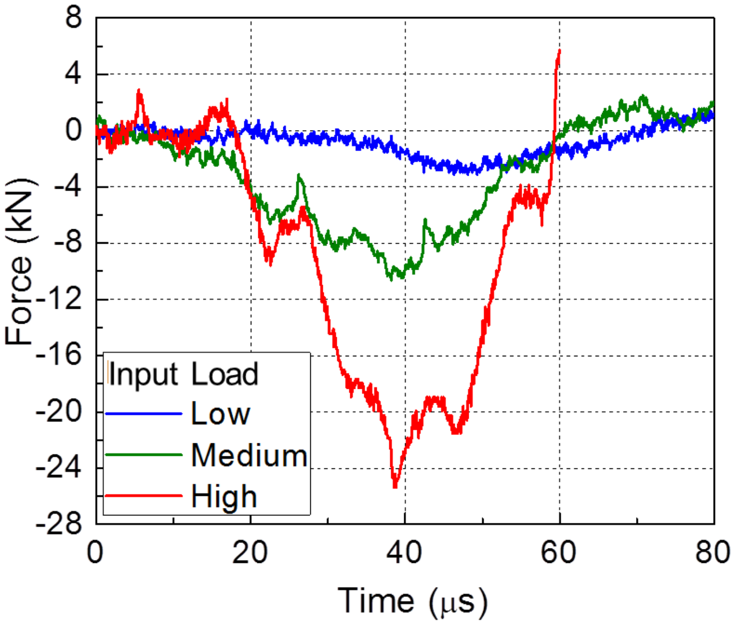

Figure 4.3: Input force profiles present in the experiments.

4.2 Experimental Results

4.2.1 Square packing

An input force of 10 kN (medium level in Figure 4.3) entered the adapter bar before loading the square granular packing (10 x 10 beads). Three piezoelectric sensors were placed within the packing at the locations shown as light gray circles in the inset of Figure 4.4. The light gray circles have a solid line which indicates the orientation of the piezoelectric disk surfaces. The sensor only measured force components that were normal to this surface. Figure 4.4 shows the force profiles measured by the piezoelectric sensors. Since the wave was reflected from the fixed boundaries, we were primarily concerned with the magnitude and arrival time of the first peak (“primary pulse”) in these force profiles. Unlike an elastic solitary wave in the same 2D configuration [60,61], the peak force decayed with increasing wave propagation distance. As will be seen shortly, the wave propagated only through chains that were directly contacting the loading bead, as in the elastic case [60,61]. Thus, the force amplitude attenuation was not due to wave front expansion but due to plastic deformation. The large drop in the peak force indicated significant plastic deformation, as expected and as predicted numerically [86]. Furthermore, the rate of peak force attenuation decreased with an increase in propagation as evidenced by the greater decrease in peak force between Sensors 1 and 2 (40% decrease) than between Sensors 2 and 3 (22±7%).

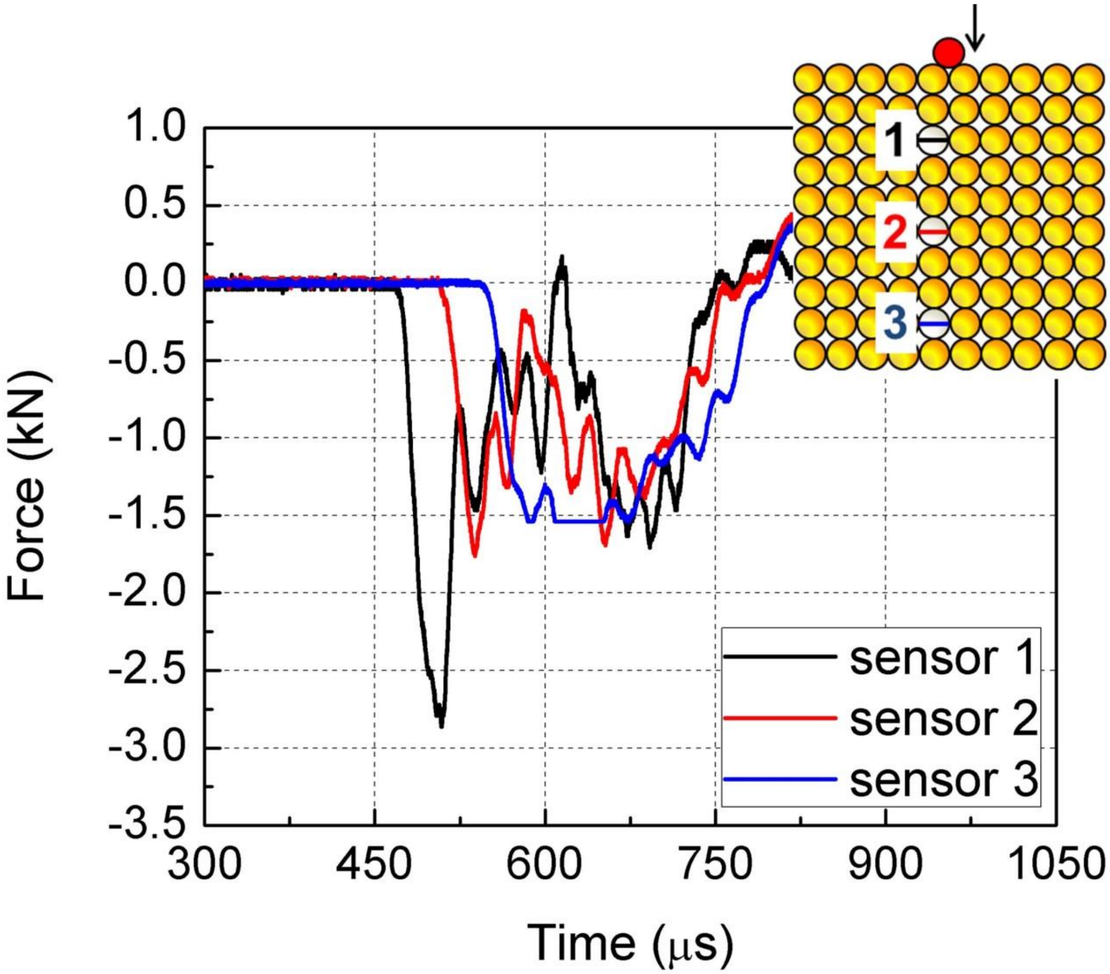

Figure 4.4: Contact force at Sensors 1, 2, and 3 in the square packing for an impact of 10 kN.

In addition to the in situ data collected from the piezoelectric sensors, postmortem optical microscopy of the contact points allowed for the construction of a yield map of the granular packing, as shown in Figure 4.5. Yielded beads are shown as blue in the figure and contacts that have experienced plastic deformation are denoted by small red rectangles (the stainless steel beads with the embedded sensors did not yield and are shown as light gray). Yielding only occurred in chains that were in contact with the loading bead. Since the elasto-plastic wave only propagated through the contacts that have yielded, it is apparent that the elasto-plastic wave propagation pattern is the same as that for a pure elastic wave in a square packing [60,61]. The wave propagation patterns are similar in the elastic and elasto-plastic cases since the force can only be transferred normal to the contact point as there is no lateral force coupling between beads.

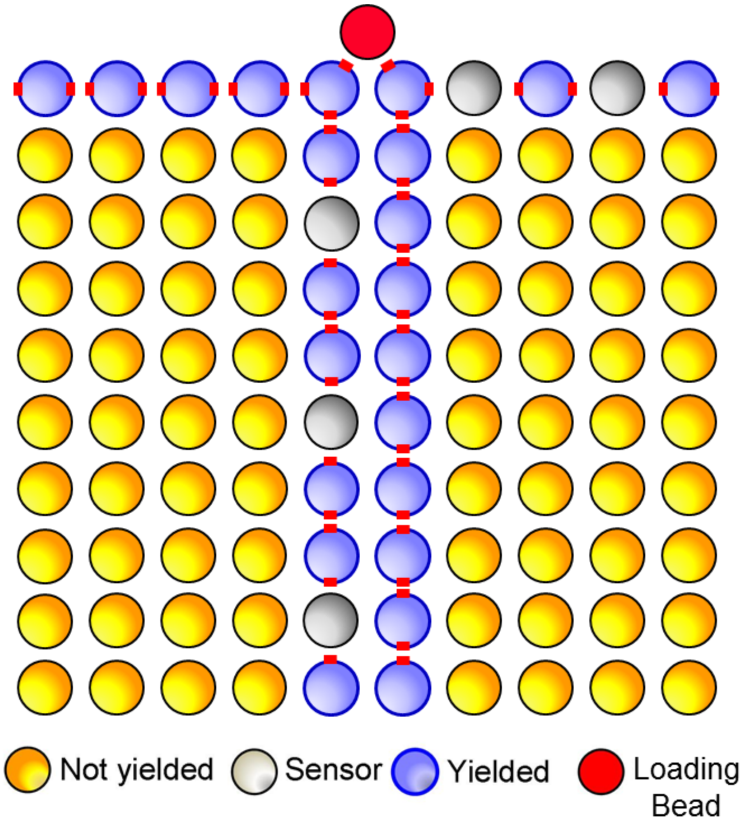

Figure 4.5: Yield map of the square packing.

4.2.2 Hexagonal packing

The hexagonal granular packings were loaded at the low, medium, and high input levels shown in Figure 4.3. The accompanying yield maps for each load level are shown in Figure 4.6.

The extent of yielded beads spread forward and laterally and increased with increasing input force level. The elasto-plastic wave again propagated similarly to the pure elastic case in which the wave front opposite the point of impact is flat [66]. Figure 4.6 also shows magnified images of the yielded contact areas at selected contact points indicating the plastic dissipation of the wave as it travelled along the 60° angle direction seen by a decreasing contact area. However, in some cases, there was overlapping yield areas – indicative of multiple impacts – e.g., at the two contact points closest to the impact in Figure 4.6c.

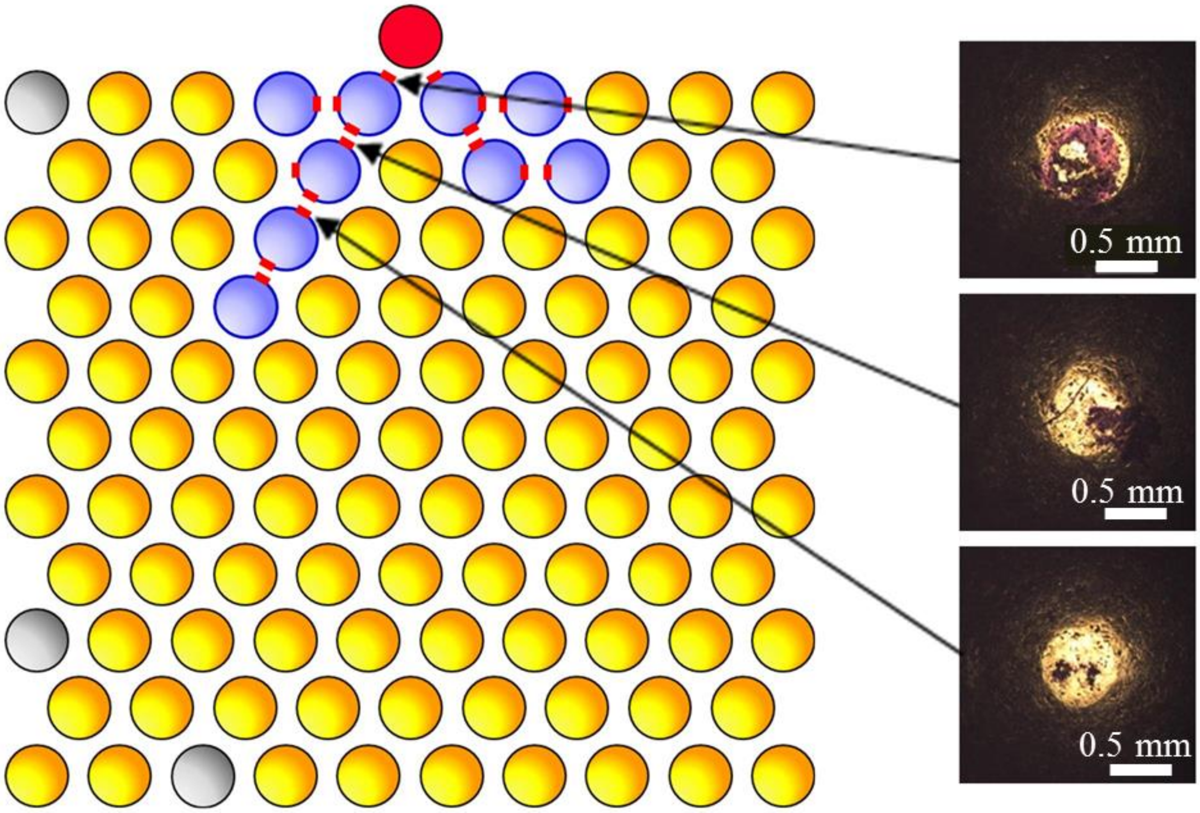

(a)

Figure 4.6 (cont.)

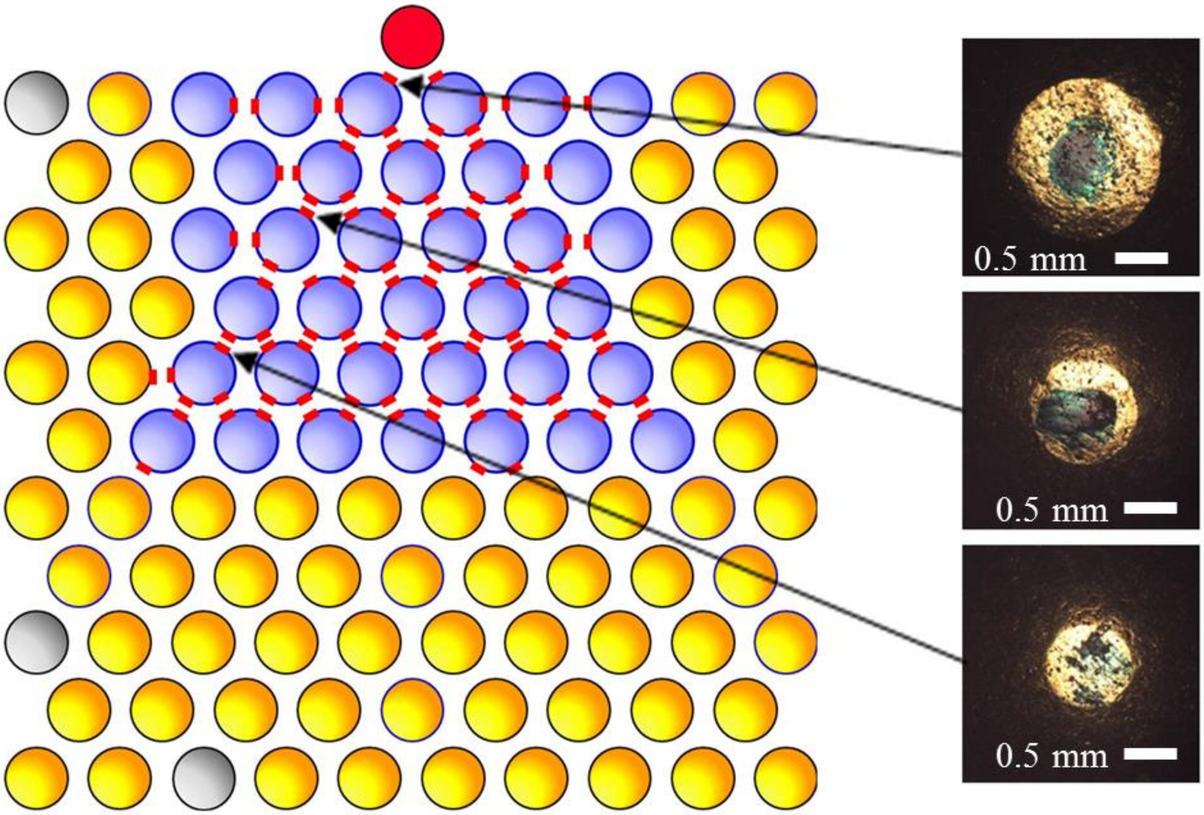

(b)

Figure 4.6 (cont.)

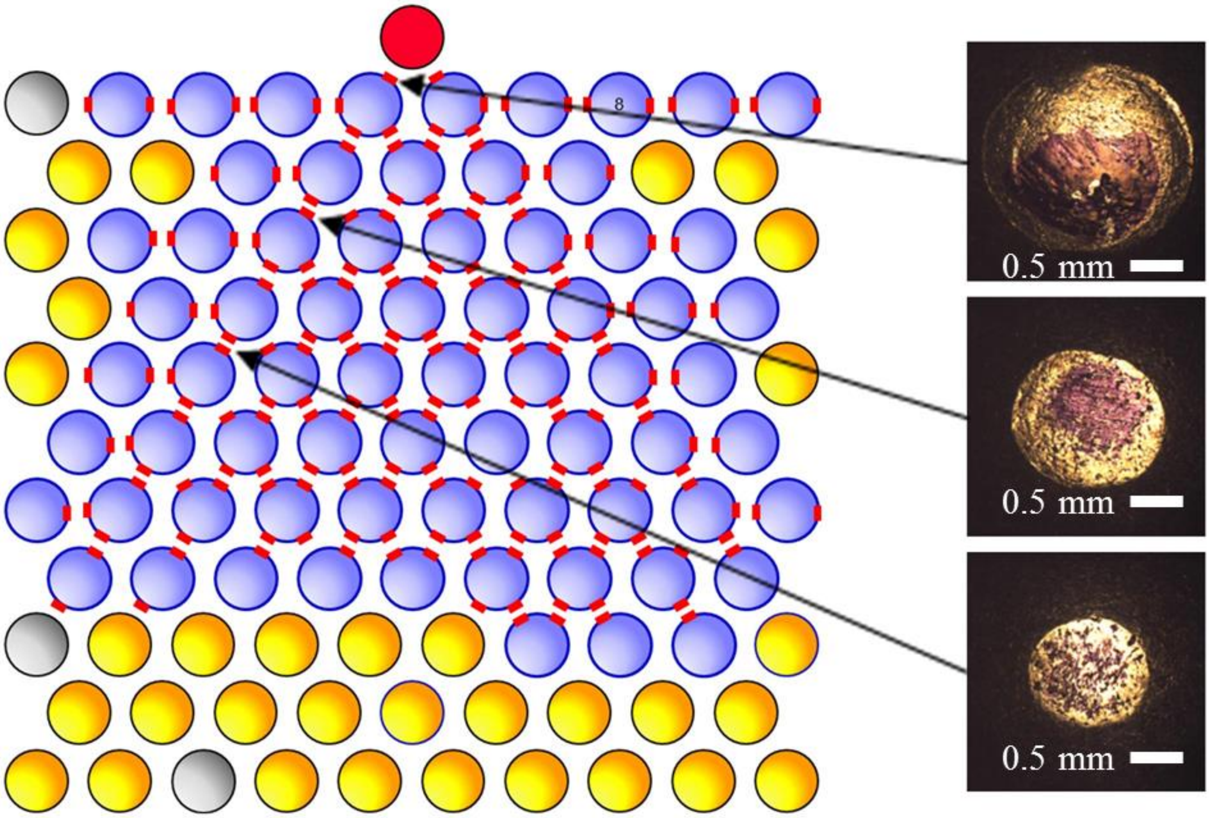

(c)

Figure 4.6: Yield map of the hexagonal packing after impact at (a) low (~4 kN), (b) medium (~10 kN), and (c) high load levels (~24 kN).

Knowledge of the maximum forces present along the wave path is important to understanding wave mitigation. It is possible to approximately reconstruct the maximum contact force at each yielded contact by measuring the yield area postmortem. The quasi-static single contact point compression experiments in [76] were carried out in the present study for several different maximum loading levels (in addition to the data available in [76]). After each quasi-static test, the size of the yield area was measured and a comparison between the yield area and the maximum force is shown in Figure 4.7. Since brass 260 is rate insensitive [76], the quasi-static data can be used in the dynamic case also to reconstruct the maximum force at every contact point based on the measured size of the yielded contact area. The finite element analysis (FEA) model developed in [80], also plotted in Figure 4.7, was used to calculate the maximum force experienced at the contact from the measured contact area. The FEA developed in [80] was relevant to this study as it provided the contact relation used in the simulations we later compare with the experimental results.

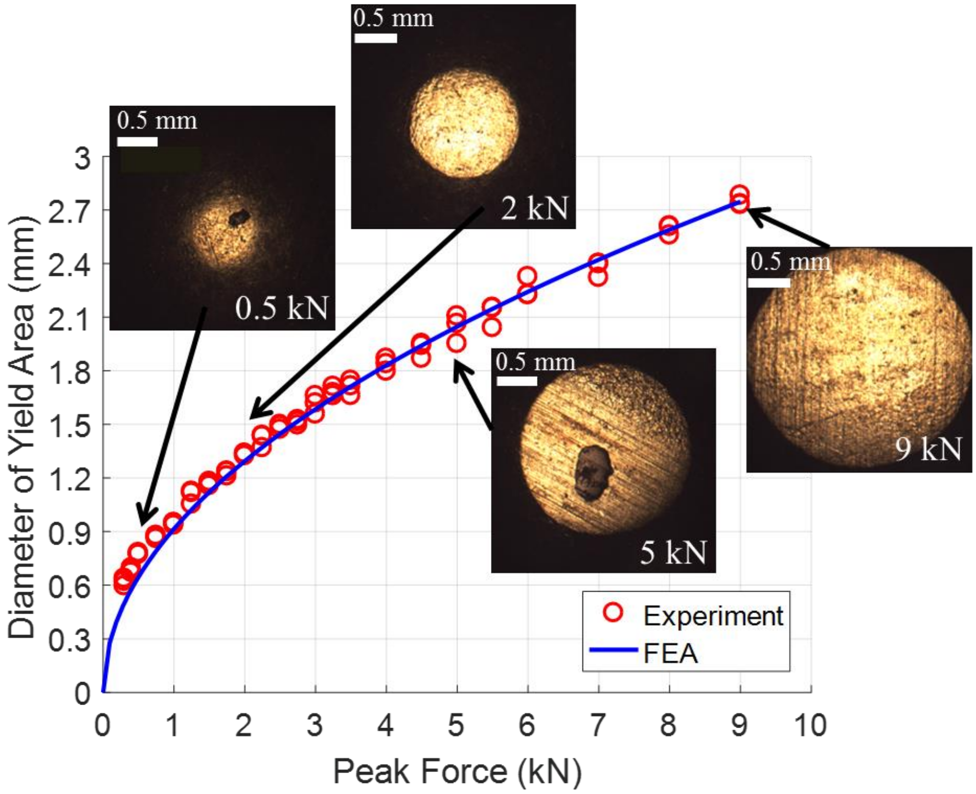

Figure 4.7: Peak compressive force vs diameter of the yield area.

Figure 4.7 shows the calculated maximum forces at every contact point along the left 60° chain in the hexagonal packing for different input loading levels. As expected, the peak force decreased with distance from the impact location. The rate at which the peak force attenuated also decreased with distance from the impact. Note that, when the maximum loading level was below 400 N (still larger than the elastic contact limit of 126 N predicted from the modified Thornton model), it became difficult to optically detect the yield area, likely since the plastic deformation originates below the contact surface[13].

Figure 4.8 compares the force experienced in the chains that were in contact with the loading bead (red) – namely the top row of beads and the two 60° chains. Figure 4.8 shows that for the given input loading, the diagonal chains experienced significantly more force than the top row of beads at the first eight contact locations. The maximum load along the top row was less than 400 N and the corresponding yield areas were difficult to detect and measure, which likely contributed to the non-monotonic behavior of the data in Figure 4.8. In general, possible errors in the yield area measurement occurred when a bead had been impacted multiple times because either it was not known which impact occurred first, as in the middle picture in Figure 4.6c, or the original shape was obscured, as in top picture in Figure 4.6c. The postmortem yield force measurement was thus subject to error due to multiple impacts.

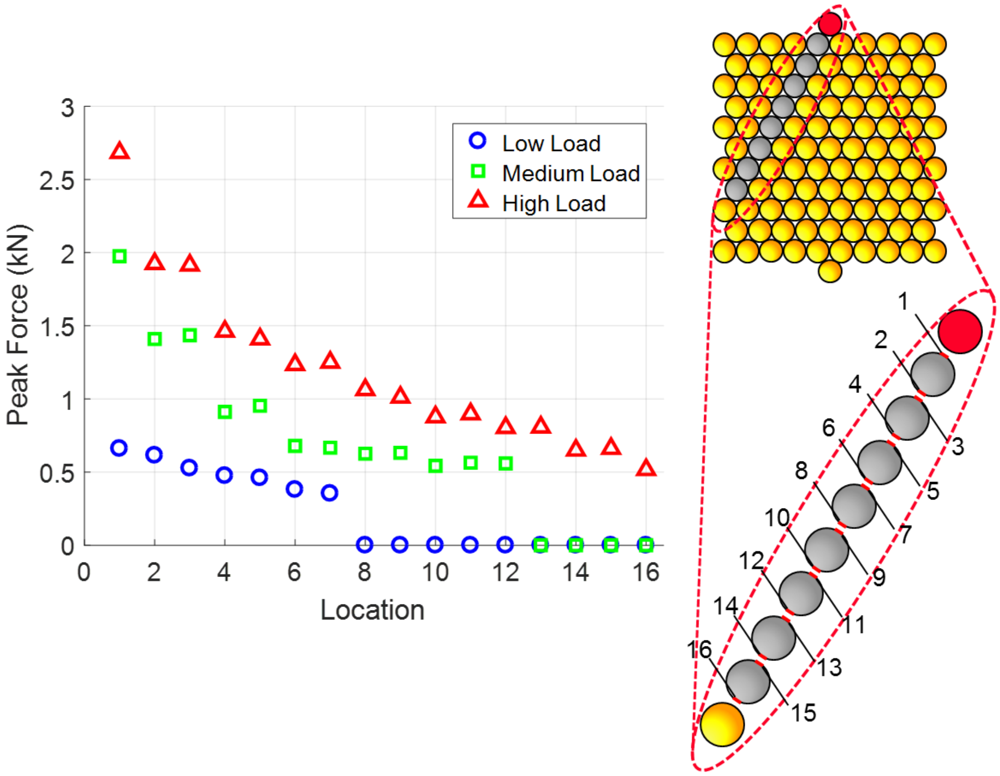

Figure 4.8: Maximum force at each contact along the left 60° diagonal.

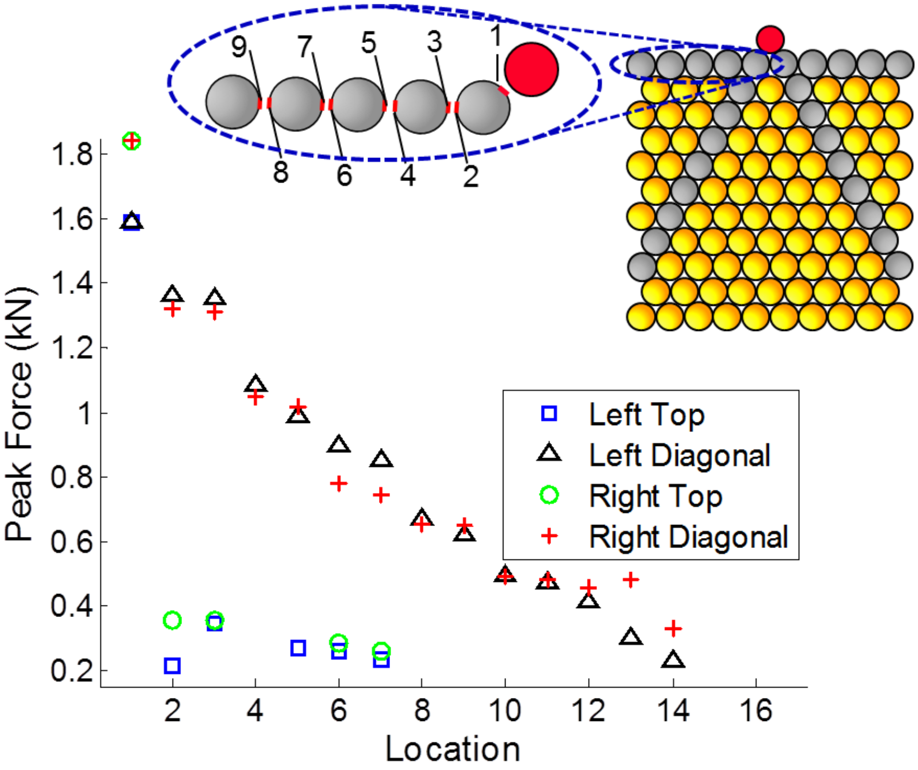

Figure 4.9: Comparison of the contact forces experienced in the two chains directly in contact with the loading bead (red). The abscissa refers to the contact location, where the contact numbers for the top row are shown here and the contact numbers along the diagonals are the same as in Figure 4.8.

In situ force measurements from the piezoelectric sensors at three locations around the packing are shown in Figure 4.10 for different input loading levels for a “typical” experiment. Each sensor location and the orientation of its piezoelectric disk (denoted by the solid line) are shown in the inset of Figure 4.10. In contrast to the square packing, the instrumented beads were only placed along the boundary of the hexagonal packing. An instrumented bead was smaller than the lower bound of the brass bead tolerance since a portion of the instrumented bead was cut away during manufacture (see Section 2.3.2 for sensor construction). Consequently, placing instrumented beads within the hexagonal packing introduced large gaps – significantly disturbing wave propagation – that could not be easily corrected with thin metal shims (as was done in the square packing) due to the lateral coupling in the hexagonal packing case.

All of the signals were synchronized such that zero time corresponded to the input load arriving at the loading bead. The results show that, similar to the case of elastic wave propagation in a hexagonal packing [66], the force amplitude and the wave speed were controlled by the loading levels. Higher loading levels resulted in higher peak force amplitudes and faster wave speeds. Increased distance from the impact source resulted in elongated force profiles. For instance, Sensor 2 is twice as far from the impact source as Sensor 1 and thus more contacts were present between Sensor 2 and the loading bead than Sensor 1 and the loading bead. As each contact plastically deforms, kinetic energy was dissipated and the loading process slowed, thus passage through more contact points elongated the force profile more.

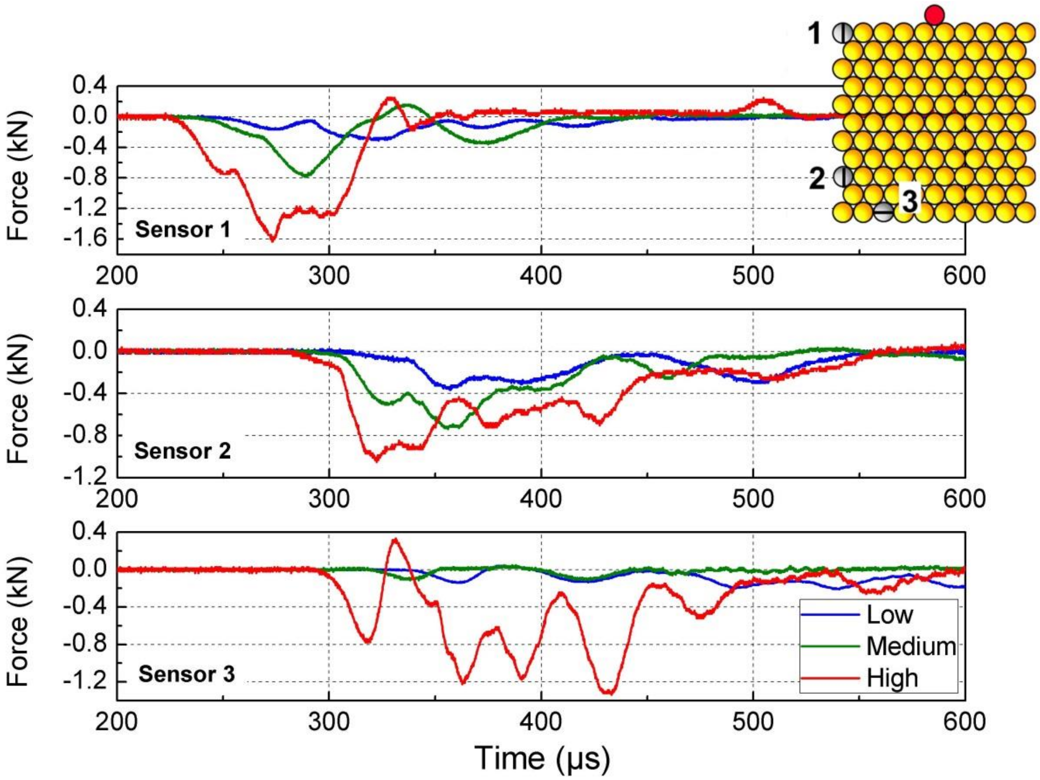

Figure 4.10: Measured forces from the piezoelectric sensors in a hexagonal packing at different input loads.

4.3 Discussion of modeling and experimental results

Our collaborators, Dr. Awasthi and Prof. Geubelle, constructed a numerical framework to simulate the dynamic behavior of the hexagonal packing. We present here a summary of their numerical results, which also appear in [88], since they enhance the discussion of the experimental results. The dynamic response of the granular packing was modeled as a frictionless network of point masses connected by nonlinear springs. As mentioned earlier, from a wave propagation perspective, modeling the bead as a point mass implies that wave propagation within each bead is assumed to be homogenized; i.e., the time scale associated with solitary wave propagation is much longer than the time required for homogenization [15,16]. In this work, the nonlinear spring captures the elasto-plastic contact interaction, not just the elastic one, normal to the bead contacts, and thus must account for unloading-reloading of the beads. This mass-spring system is similar to a molecular system and thus the open source MD simulation software LAMMPS, developed in 1995 by Sandia National Laboratories, was used to simulate the current problem [105].

The modified Thornton model, an elasto-plastic contact model described in [76], was used to simulate the contact interaction between beads. The model is described by Eqs. 4.1-4.2 below, where F is the contact force and δ is the displacement between the particle centers:

$$\text{loading part:} \quad \begin{cases} F = \frac{4}{3}E^{*}\sqrt{R^{*}\delta^{3}} & \text{when } F \le F_y = \frac{1}{6}\left(\frac{R^{*}}{E^{*}}\right)^{2}\left(\pi p_y\right)^{3} \\ F = F_y + \pi p_y R^{*}\left(\delta - \delta_y\right) & \text{when } F > F_y = \frac{1}{6}\left(\frac{R^{*}}{E^{*}}\right)^{2}\left(\pi p_y\right)^{3} \end{cases} \qquad (4.1)$$

$$\text{unloading part:} \quad F = \frac{4}{3}E^{*}\sqrt{R_p^{*}\left(\delta - \delta_R\right)^{3}}$$

where E^{*} and R^{*} are describe in Eq. 1.1, δ_R is the residual displacement after unloading, and the terms associated with yielding are:

$$\delta_y = \frac{1}{4}\frac{R^*}{\left(E^*\right)^2}\left(\pi p_y\right)^2 \text{ and } R_p^* = \frac{4E^*}{3F_{max}}\left(\frac{2F_{max}+F_y}{2\pi p_y}\right)^{3/2}. \tag{4.2}$$

The critical yield pressure, p_y, according to the von Mises yield criterionfor brass alloy 260 is $1.6\sigma_y$, where σ_y is the uniaxial yield stress of the material and the yield force is F_y, which is well below that seen experimentally. Consequently, it is usual to modify the Thornton model by adjusting the magnitude of the yield pressure accordingly [78]. For brass alloy 260 the adjusted yield pressure, p_y is $4.7\sigma_y$.The contact displacement at yield, when $F = F_y$, is δ_y, the maximum force before unloading is $F_{\max}$, and the curvature after plastic deformation occurs is R_p^*. Figure 4.11, taken from [76], demonstrates that the modified Thornton model with p_y = $4.7\sigma_y$ accurately describes the experimental contact behavior between the brass beads in the current study. Since brass 260 is strain rate insensitive [76], rate sensitivity was not considered.

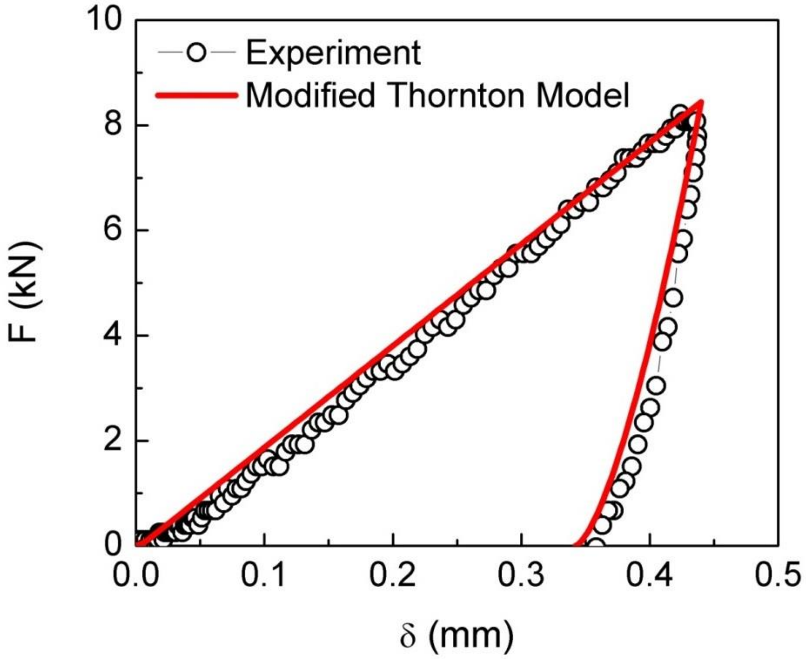

Figure 4.11: Comparison of modified Thornton model (solid line) used to model 2D granular lattice with experimental points (circles) [76].

The boundary was numerically modeled by placing additional spherical beads at every location where the outer beads in the array contacted the boundary. The beads comprising the boundary were fixed in space (i.e., their centers of mass were constrained against displacement) and were also modeled to be rigid (hence no deformation of the wall during contact). The contact interaction (described by the modified Thornton model discussed above) between the boundary and an adjacent bead was made to represent the interaction between a rigid half-space and a sphere by setting the radius of curvature of the boundary to zero. The steel instrumented beads were not modeled, i.e., their positions were occupied by brass beads in the model. The numerical system, which did not include the adapter bar, was loaded by placing an input force profile into the loading bead (unnumbered bead in Figure 4.1). The numerical input load is based on the experimental load that was input into the adapter bar. Specifically, the input force profiles obtained experimentally (Figure 4.3) are fit with a sine curve which is then used as the load input to the loading bead in the numerical set up.

4.3.1 Perfect packing simulation comparison

We started with a perfect system, i.e., one in which the beads were considered to be identical and positioned exactly in a hexagonal pattern. As an example, the simulated force profiles for the three loading cases at the Sensor 1 location for a perfect hexagonal packing are shown in Figure 4.12 and compared with a “typical” experimental result from Sensor 1 for the three load levels. The numerical results compared favorably with the experimental results with respect to arrival time, peak force, and pulse length. The experimental peak force was 15-35% less than the numerical peak forces. The input force measured experimentally was directly input into the packing in the numerical simulations (i.e., neglecting the existence of the adapter bar), whereas in actuality the measured input force in Figure 4.3 was the force applied to the adapter bar. Therefore, we expected the input force put into the experimental granular system to be less than the force put into the simulation. Regardless, Figure 4.12 indicates that the numerical model is capable of capturing the main characteristics of the experimental setup.

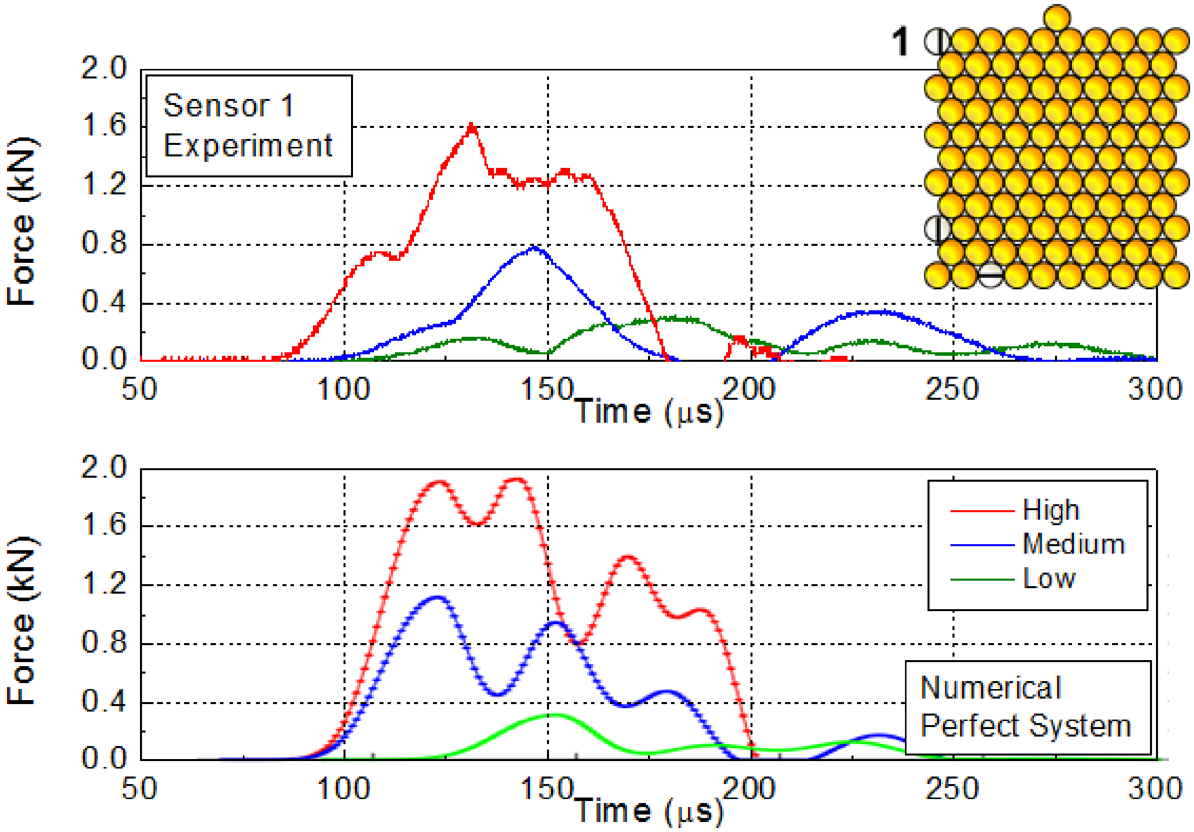

Figure 4.12: Comparison between experimental (top) and numerical (bottom) force profiles at the Sensor 1 location for high (red), medium (blue), and low (green) input loads.

4.3.2 Scatter in experimental results

Although Figure 4.12 shows general agreement between *one* experimental result and the simulations, repeated nominally identical experiments on the hexagonal packing (different packings used in each experiment) revealed that there was scatter in the arrival times and peak forces at the sensor locations. For example, Figure 4.13 shows the loading profile from multiple experiments with similar incident loads at the Sensor 1 location and the scatter in the primary pulse amplitude is apparent. Additionally, beyond the primary pulses in Figure 4.13, there is little repeatability in the time records. One possible reason for such variability was the existence of imperfections in the experimental set up of a nominally perfect hexagonal packing.

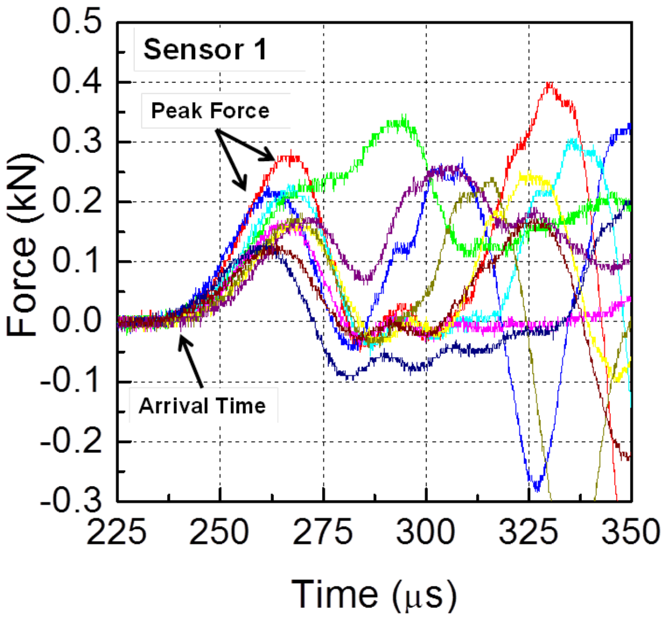

Figure 4.13: Force profiles at the Sensor 1 location for different experiments with nominally similar input loads.

Although extreme care was taken in aligning the granules before each experiment, there inevitably were gaps between beads, as shown in Figure 4.14, which influenced wave propagation through the array. If every bead in the system was identical, then the beads would contact each other perfectly with no gaps or initial compressive forces prior to impact.

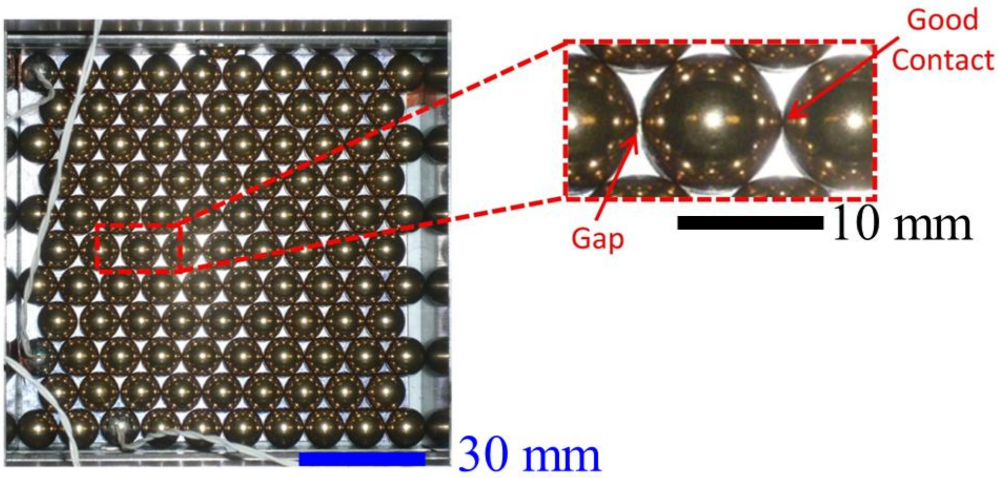

Figure 4.14: Imperfections within the packing.

Figure 4.15 shows the numerical peak force and arrival time at locations 1, 2, and 3 for the ideal case of identical beads when the packing was subjected to the high, medium, and low loads shown in Figure 4.3. However, the beads inevitably had a size tolerance (diameter tolerance of ± 0.00254 mm (± 0.001 in), as quoted by the manufacturer). When these non-identical beads were packed together, gaps between beads occur randomly throughout the packing – some of which may be imperceptible to the naked eye. At the same time, other contact locations may experience a precompressive force. These imperfections, mainly caused by size randomness, could significantly affect the wave propagation in a granular packing. It is worth noting at this point that no sensor beads were placed in the interior of the hexagonal array, unlike the case for the square array, precisely because the steel sensor beads had a slightly different size than the brass beads and would cause significant gaps in the initial set-up. (For the square array this effect was less pronounced which allowed placement of sensors within the array itself.)

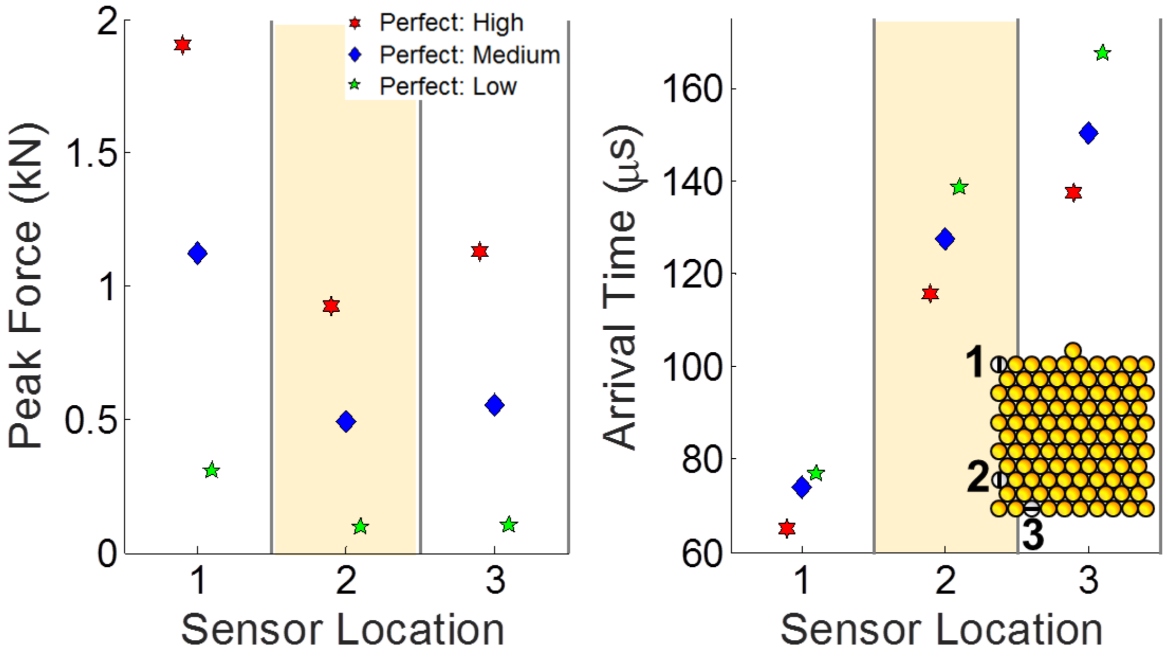

(a) (b)

Figure 4.15: Simulated peak force and arrival time at sensor locations 1, 2, 3 for high, medium, and low input loads for the case of monodisperse beads in the hexagonal packing.

4.3.3 Introducing randomness into the simulations

To further investigate the effects of disorder in the hexagonal array, our collaborators incorporated the bead size randomness into the numerical model. Based on the maximum diameter tolerances provided by the manufacturer, they assumed a normal distribution of bead diameters. They then conducted a large number of simulations (300 for each loading case) that incorporated random amounts of variability in the bead diameter in order to develop a numerical spread in the results that could be compared with the experimental variability. Figure 4.16a shows the numerical spread in the peak force at locations 1, 2, and 3 while Figure 4.16b displays the spread in the arrival time at each location. The numerical spread is denoted by error bars that are attached to solid markers: a red circle for the high input load, a blue square for the medium input load, and a green triangle for the low input load. The solid markers are indicative of the average value of the numerical spread. The numerical results for the perfect packing (all beads of uniform diameter) are also included.

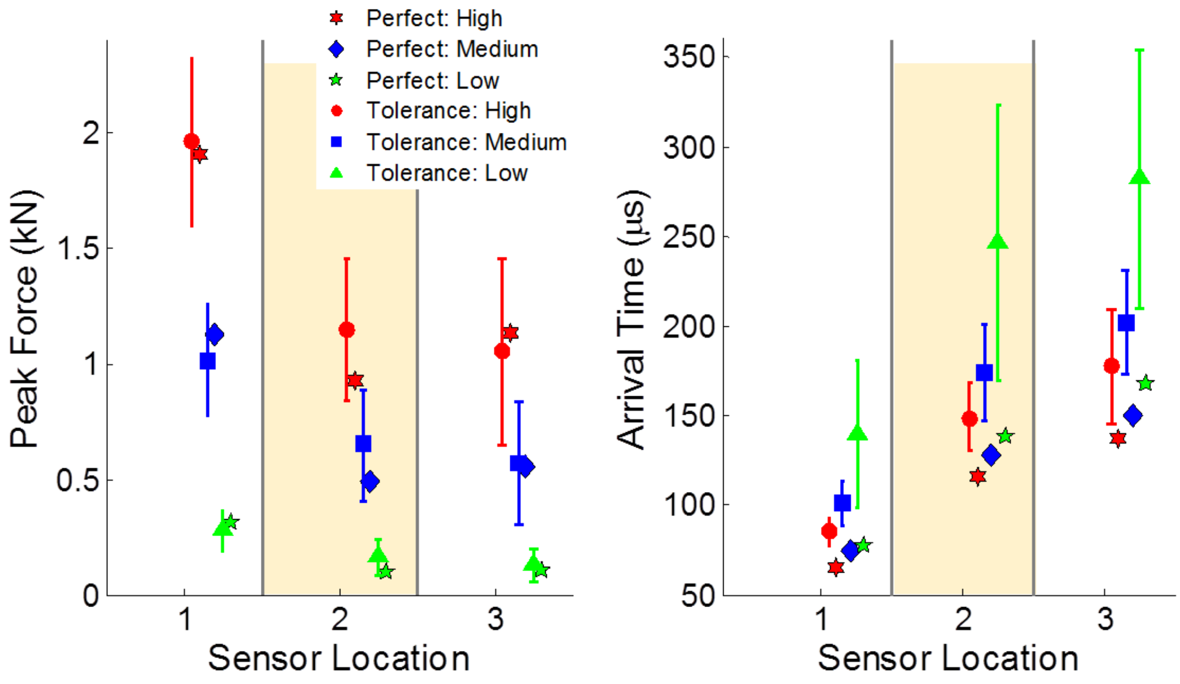

(a) (b)

Figure 4.16: Simulated peak force and arrival time at sensor locations 1, 2, 3 for high, medium, and low input loads for the case of monodisperse beads in the hexagonal packing.

Figure 4.16 serves as a baseline for the scatter that could be expected in the experimental data if the bead tolerance were the only source of non-uniformity between nominally identical experiments. Figure 4.17 and Figure 4.18 summarize all of the experimental and numerical data at each sensor location for the peak force and the arrival time of the primary pulses, respectively. Several experiments were conducted on the hexagonal packing and are grouped by the input load into the adapter bar. The legend in Figure 4.17 and Figure 4.18indicates that the input forces mostly fall between the low and medium input cases in Figure 4.3 and thus only the simulated results that correspond to the low and medium input loads are included. The experimental spread is not denoted by error bars, and instead each marker represents the value of the peak force or arrival time at a sensor from one individual test. Finally, each data group has been slightly offset for clarity of presentation. All of the data points that fall between 0.6 and 1.4 on the x-axis correspond to data from the Sensor 1 location. Similarly, data points that fall between 1.6 and 2.4 on the x-axis correspond to data from the Sensor 2 location and data points that fall between 2.6 and 3.4 on the x-axis correspond to data from the Sensor 3 location. Three additional locations in the packing are also experimentally considered and are labeled as locations 4, 5, and 6. Since there are only 5-6 data points at locations 4, 5, and 6, there is an apparently smaller scatter than the other three locations which have at least 20 data points each.

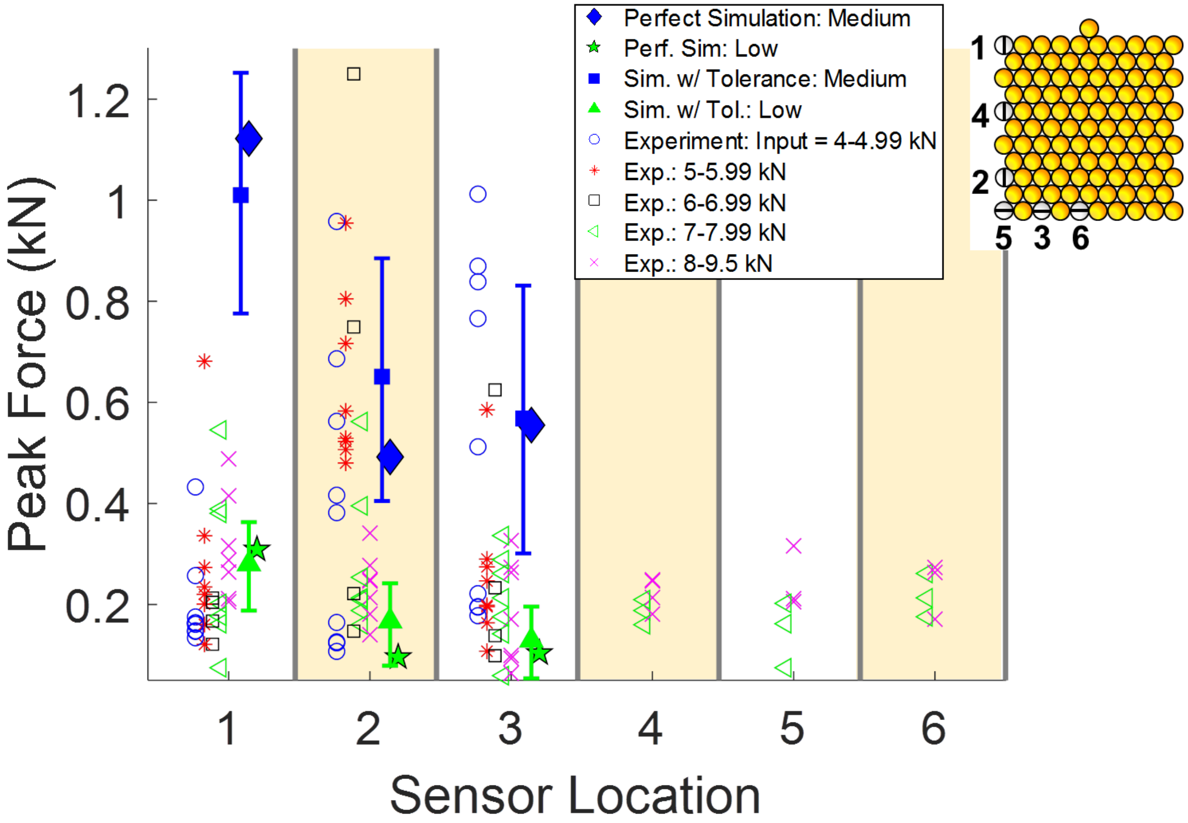

Figure 4.17: Comparison of peak force at the six sensor locations between the experiments, the perfect packing simulations, and simulations with diameter tolerance included.

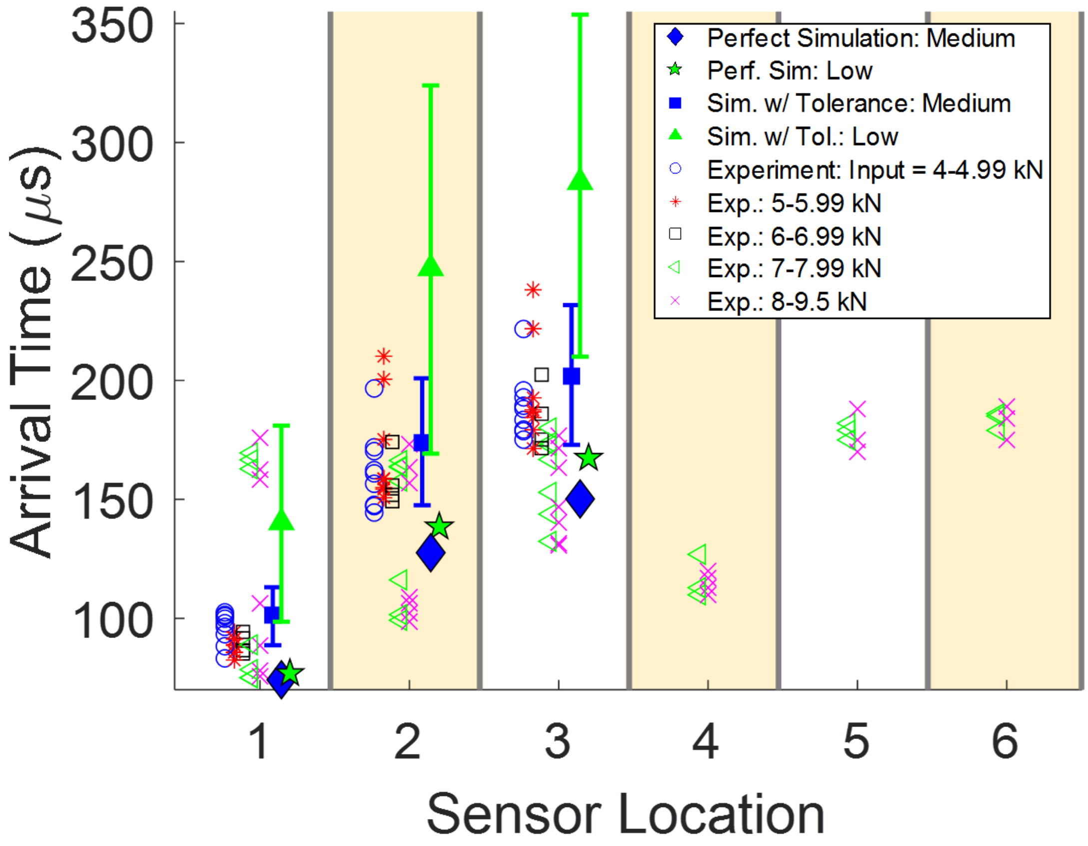

Figure 4.18: Comparison of arrival time scatter between experiments, perfect packing simulations, and simulations with diameter tolerance included.

When incorporating size tolerance, the numerical predictions and the experimental results have a large overlap, which indicates that size tolerance plays an important role in the propagation of an elasto-plastic wave. For the arrival time, all of the numerical spreads occur later than the perfect packing. Gaps induced by the size tolerance increase the wave propagation distance because the wave propagates through a path that has more contacts compared to the perfect case. The current consideration on the size tolerance does not fully encompass the scatter in the characteristic features of the experimental granular packing. Additional factors that could improve the simulation would be to include more features such as friction and the actual distribution of the bead diameter (instead of assuming a normal distribution).

5. MOMENTUM AND FORCE OPTIMIZATION IN A 2D SQUARE PACKING

Traditional methods of mitigating incoming stress waves involve energy dissipation via plasticity or through the formation of damage and/or fracture surfaces. Here, we seek to manage an elasto-plastic wave in a granular packing, in addition to mitigating it, such that we can redirect the wave away from sensitive components. In this Chapter, we will redirect elasto-plastic wave propagation in a square granular packing by selective placement of intruders at interstitial locations. Previous work has shown that interstitial intruders have a drastic effect on wave propagation since they enable lateral coupling which would otherwise not be present in the square arrangement [61–65]. The placement of the intruders will be guided by a numerical optimization scheme, performed by our collaborators on this project Prof. D.A. Tortorelli and Mr. M. Salazar de Troya, that optimizes specific objective functions depending on the desired stress wave control (force or momentum maximization or minimization).

5.1 Experimental Details

5.1.1 Granular packings and interstitial intruders

Two different granular packings of rate-independent brass beads were considered using the load frame, Hopkinson bar, and instrumented beads described in Chapter 2 and used in Chapter 4. The first packing that was investigated (in the momentum optimization study described below) was an 11x10 square packing, shown in Figure 5.1a. The non-impedance matched stainless steel adapter bar transfered the load between the Hopkinson bar and the loading bead, which is colored purple in the figure. The loading bead had the same material properties as the other beads in the packing and was placed in contact with only the central (6th) bead in the top row.

In the second set of experiments (which will investigate force optimization), the load frame had been enlarged to accommodate a 14x13 square packing of brass spheres and was shown in Figure 5.1b. Guided by results from 1D elasto-plastic experiments [82], the solitary-like wave that emerges from elasto-plastic loading requires 5 bead diameters to fully form – similar to an elastic solitary wave [15]. Thus the larger packing enabled the resulting waves to more fully develop and also reduced any signal disturbances that may have occurred from multiple hits from the Hopkinson bar. The 14x13 packing was surrounded by stainless steel spheres on three sides, which allowed the instrumented bead to be placed as part of the boundary rather than replacing a brass bead as was the case in the 11x10 packing described above. The adapter bar now was tungsten carbide (WC) and was impedance matched with the stainless steel incident bar. The adapter bar was in contact with a brass loading bead, colored purple in Figure 5.1b, which rested symmetrically in contact with the 7th and 8th beads in the first row.

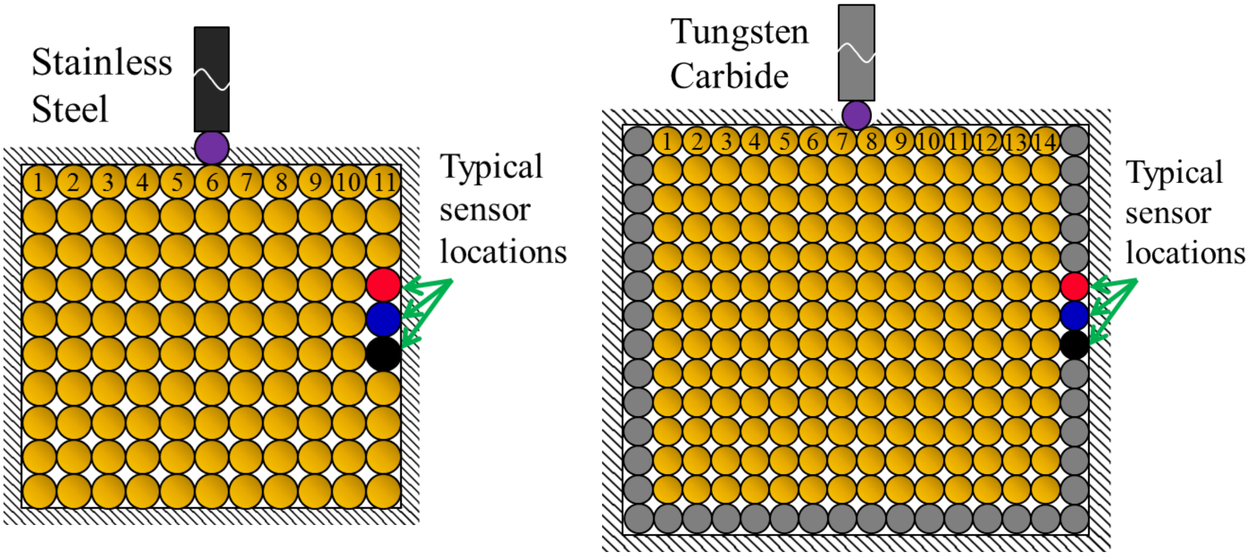

(a) (b)

Figure 5.1: (a) 11x10 square packing of beads with a stainless steel adapter bar in contact with the loading bead, which is only in contact with the 6th bead in the top row. (b) 14x13 square packing where the loading bead know rests symmetrically between the 7th and 8th beads in the top row.

Lateral coupling of the rectangular cardinal network shown in Figure 5.1 as achieved by appropriate placement of interstitial intruders. Prior works that have used smaller diameter spheres as the interstitial intruder particles [61,64,65] have either been numerical in nature (i.e., no physical setup required) or have placed custom-made beads atop holders at a few specific interstitial locations. Here we used cylinders as the interstitials since they can practically be placed at a large number of interstitial locations and remain situated throughout setup. The interstitial intruders were stainless steel cylinders ($E = 200\text{ GPa}$, $\rho = 7600\text{ kg/m}^3$, $\nu = 0.35$) and had a height, $h = 9.53\text{mm}$, identical to the bead diameters and a diameter, $d = 3.93$ mm, that allowed them to fit in a given interstitial location and touch the four surrounding beads. Figure 5.2 shows a packing with stainless steel intruders at all of the interstitial locations, a close-up image of the cylinder in the interstitial, and a side view schematic. The stainless steel intruders did not yield at the peak forces involved in these experiments, so only the brass beads experienced plastic deformation. Since the cylinder height was the same as the bead diameter, the centers of mass were the same and there was no torque introduced throughout the loading process. One drawback of using a cylinder as an interstitial was the increased friction due to the contact between the cylinder's face and the base of the load frame. However, a polytetrafluoroethylene (PTFE) sheet rested on the load frame's base, minimizing the friction due to the cylinder's contact. A second drawback was that an elasto-plastic force-displacement relation was needed for a sphere and a cylinder, and this was measured in this effort (see below Section 5.1.3).

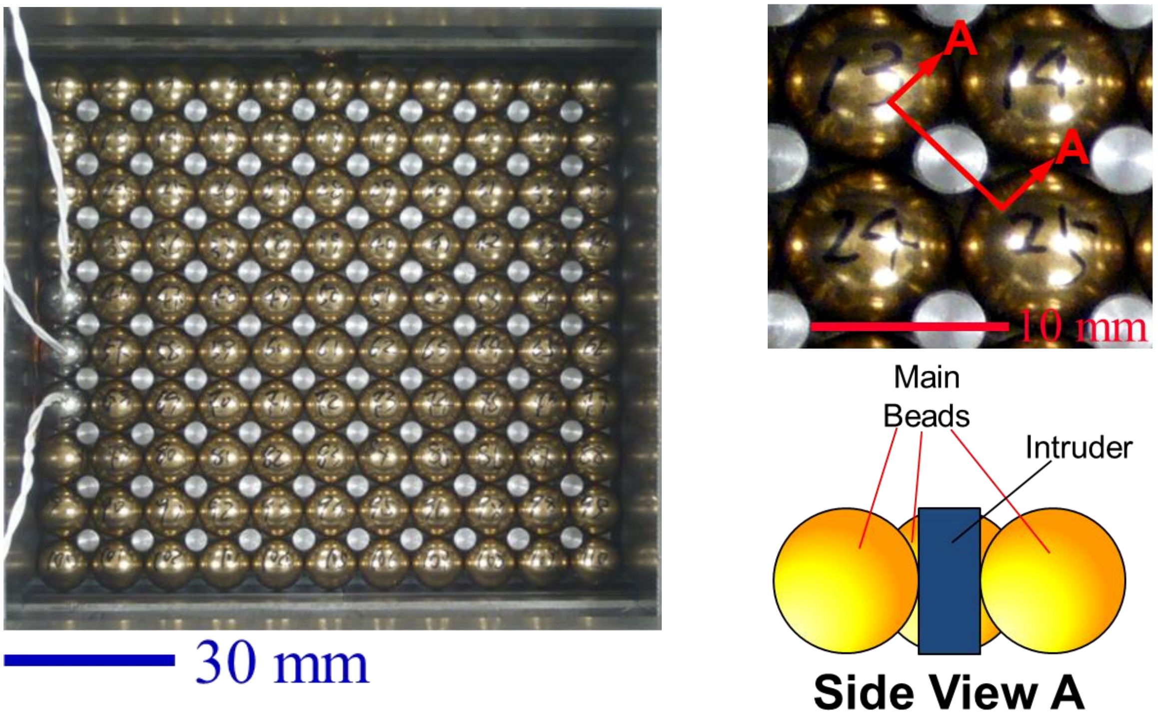

Figure 5.2: Square packing of brass beads with stainless steel cylinder located at interstitials.

5.1.2 Input forces

In all of the optimization experiments, a thin copper ($h = 0.8$ mm, $d = 6.4$ mm) pulse shaper was placed at the interface where the striker propelled by the gas gun impacted the

Hopkinson bar. The pulse shaper smoothed the applied compressive loading pulse by elongating the loading pulse rise time and made the pulse triangular rather than trapezoidal, bringing it closer to the half-sine wave which was used as the input to the simulations (described below). The two different packings discussed above had different adapter bars which affect how the optimization scheme is performed.

For the stainless steel bar, the input load (calculated from strain gage measurements of the Hopkinson bar as in Chapters 2 and 4) measured was the force input to the adapter bar, not the loading bead. In the simulations the applied load was idealized as a similar shaped pulse (half-sine) and had the same time variation as that measured in the experiments. Unlike Chapter 4, we modeled the response of the adapter bar as well, and applied the idealized load on the adapter bar. Figure 5.3a displays strain gage signals from the input loads for the 11x10 system. When the incident and reflected pulses were summed, the resulting signal provided the load input to the stainless steel adapter bar. The resulting compressive input loads and the simplified half sine representation that was used as the input for the numerical scheme are plotted in Figure 5.3b. The half sine wave had an amplitude of 8 kN and pulse width of 42.6 μs. The stainless steel adapter bar was modeled with 1D finite elements and the interaction between the bar and the loading bead was modeled as an interaction between a stainless steel sphere of infinite diameter and a brass bead of diameter 9.53 mm. Figure 5.3c shows the numerical input load in the adapter bar and the force experienced at the adapter bar-loading bead contact and provides information regarding the transit time of the input load in the modeled adapter bar. In all the optimization-related simulations time $t = 0$, corresponded to the moment the input pulse enters the adapter bar. In the raw experimental measurements time $t = 0$ varied and occurred shortly before the incident pulse in the Hopkinson bar triggered the acquisition systems. Thus, to compare the two sets of results on the same time scale, an appropriate shift in the experimental data was made by subtracting the transit time of the incident pulse from the strain gage to the Hopkinson bar-adapter bar interface (i.e., half the time between the initiation of the incident and reflected pulses).

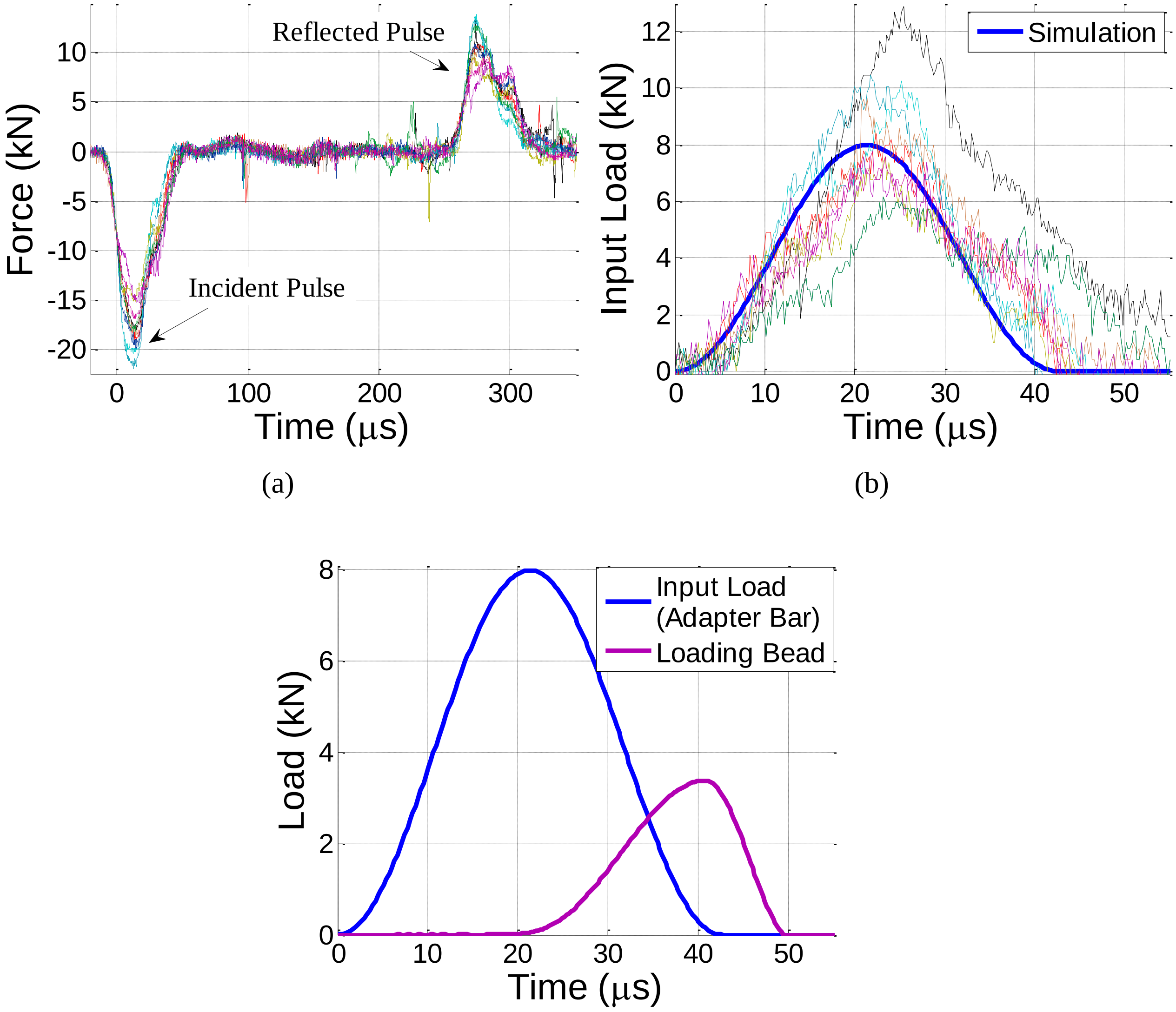

(a)

(b)

(c)

Figure 5.3: Input load for the 11x10 system. (a) Strain gage signals (converted to force) from the Hopkinson bar for multiple nominally identical experiments. (b) Several calculated input loads from the experiments compared with the input load used in the simulations. (c) Simulated values of the force in the adapter bar and the loading bead.

In the larger 14x13 packing, the input load was increased beyond that shown in Figure 5.3 to increase the signal to noise ratio in the instrumented beads (as will be seen below). Typical input loads measured in the 14x13 packing case, along with the corresponding input load to be used in the simulations, are shown in Figure 5.4, where the half-sine wave simulation input had amplitude 15 kN and pulse width 60 μs (compared to 8 kN and 42.6 μs for the 11x10 packing). The implementation of the impedance matched WC bar allowed the experimentally measured input force to be applied directly onto the loading bead in the simulations, bypassing the need to simulate the adapter bar in addition to the array itself. Nonetheless, an attempt was made to include the WC bar in the optimization scheme similar to how the stainless steel adapter bar was incorporated. However, the optimization did not converge, perhaps due to the greater stiffness of WC (627 GPa, compared to 200 GPa for steel) and the consequently smaller time step numerically required. The pursuit of numerically incorporating the WC bar in some manner led to the complicated (when compared to the valid approach of applying the input load in Figure 5.4 directly to the loading bead in the optimization) approach used in this study, described below.

The contact force history between the WC adapter bar and the loading bead was obtained from a deterministic simulation (which did not invoke the optimization scheme) of the packing with no intruders where the WC adapter bar had been subjected to the half-sine representation of the input load. The simulated contact force (between the WC bar and the loading bead) was then used as the input (applied on the loading bead) for the optimization scheme which did not contain any representations of the adapter bar. Next, the optimization was performed and provided the quantity and locations of the interstitial cylinders to best accomplish some prescribed objective. At this point, the contact forces among the brass beads in the packing and between the brass beads and the wall had also been calculated, and we refer to this set of contact forces as “Data Set 1.”

Another deterministic simulation was conducted with the WC adapter bar and the granular packing with the now-known location of the stainless steel cylinders. This final deterministic simulation produced another set of contact forces among the beads in the packing and the beads and the wall, which we denote “Data Set 2.” The contact forces in Data Set 2 were compared with the experimentally determined contact forces at the locations of interest. Note that the contact forces in Data Set 1 and Data Set 2 were not identical.

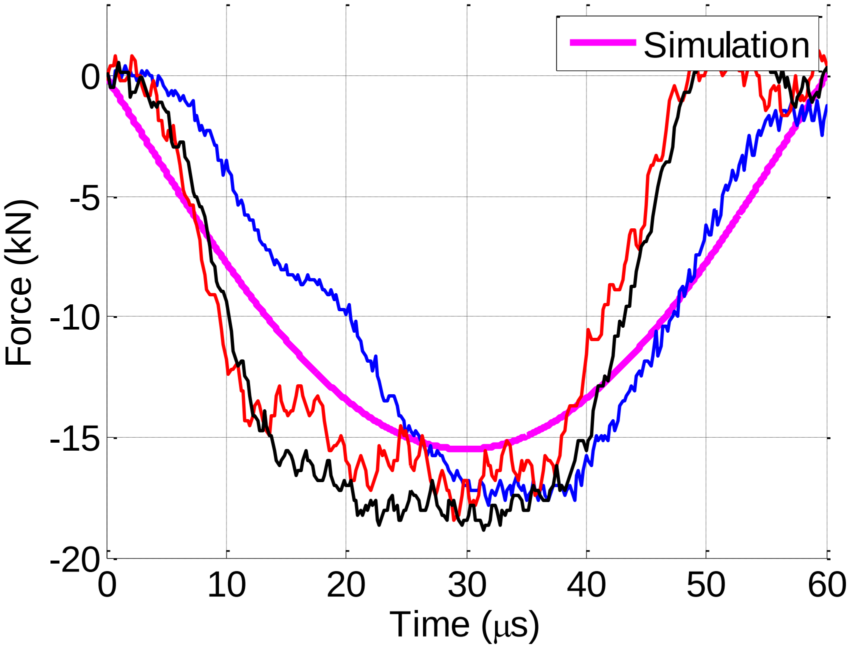

Figure 5.4: Comparison between experimental input loads and simulated input loads used in the 14x13 array.

5.1.3 Elasto-plastic contact relation between brass sphere and stainless steel cylinder

For the numerical analysis of the response of the array which was composed of the cardinal 2D square array of brass beads and the cylindrical stainless steel intruders, the optimization required the load-displacement contact relationship of two brass beads in contact, provided by [76], as well as the elasto-plastic contact relation between a brass bead and a stainless steel cylinder, for the lateral coupling contacts. The contact relation between a brass bead and steel cylinder was obtained here experimentally by placing a brass hemisphere and a steel half-cylinder (i.e., extruded semi-circle) in a quasi-static load frame, as shown in Figure 5.5a. Several of these experiments were performed, with some of the resulting force-displacement data plotted in Figure 5.5b to keep the figure uncluttered. The system was unloaded and reloaded several times until reaching a maximum force of 10 kN, at which point it was only unloaded. Figure 5.5b only shows a subset of the results obtained. Significantly more loading and unloading curves were generated such that we could confidently numerically interpolate between them for any value, up to 10 kN of contact force (a value larger than the largest load expected at a bead-cylinder contact in the impact experiments). The data have been smoothed using the moving average method. Note that it was justifiable to obtain the contact relation quasi-statically yet use it in the simulations of a dynamically loaded array since brass 260 is rate independent and [79] showed that the contact law between two dissimilar granules is controlled by the material with a lower yield stress which is brass in this case. In any case, the steel cylinder remained elastic throughout.

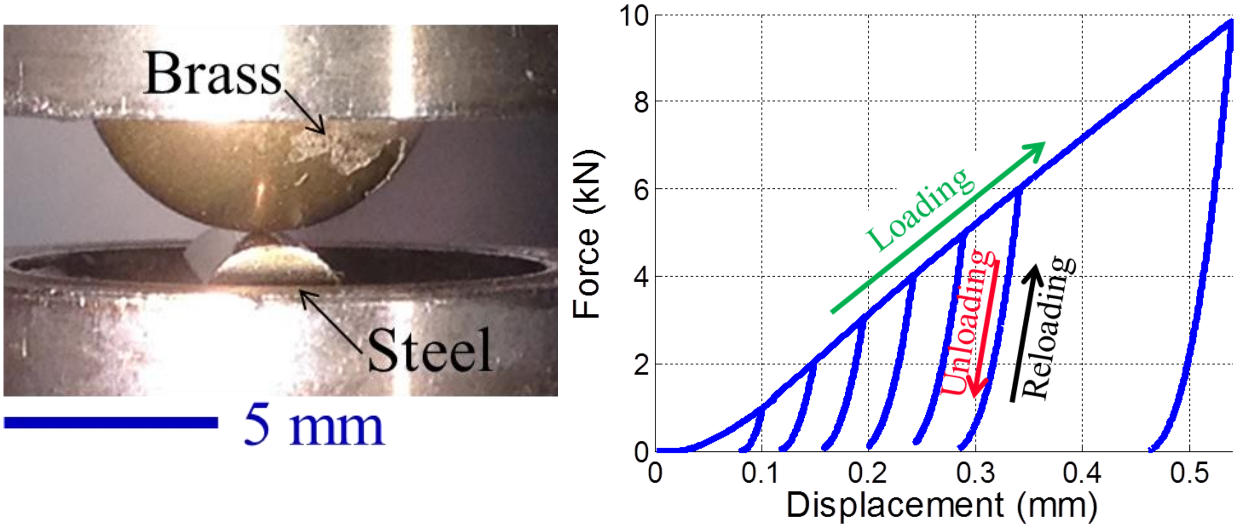

(a) (b)

Figure 5.5: (a) Setup used to obtain contact law between brass sphere and steel cylinder. (b) Smoothed experimental data showing the contact law with several unloading curves.

5.2 Numerical Optimization Scheme

A numerical optimization scheme – developed by our collaborators Mr. M. Salazar de Troya and Prof. D.A. Tortorelli – was used to determine the quantity and location of the cylindrical intruders placed in the square 2D array such that a maximum and/or minimum momentum and/or force can be accomplished at some desired location(s). The optimization scheme utilized a discrete element method that modeled the deformation between the centers of contacting particles (i.e., spheres or cylinders) as a spring-mass system, where the elasto-plastic contact relation was derived from the finite element analysis in [80]. The cost function was constructed such that when minimized, the desired quantity and location of interstitial intruders could be extracted. The optimizations were not constrained; that is, they were allowed to choose any quantity of cylinders to satisfy the given objectives, although constrained optimizations where intruders cannot exceed a maximum number could also be made. The transient problem was solved with a fifth-order explicit Runge-Kutta method and an adjoint sensitivity analysis was employed. Of particular importance, as we will see later, was that each optimization initiated with the potential for an intruder to be placed at each interstitial and a penalty method determined if the intruder should be realized at a particular interstitial. Full details of the method can be found in [89].

5.3 Momentum Maximization in an 11x10 System

Maximizing momentum at specified locations can be considered as either a wave focusing or a wave deflection application, depending on whether the maximization occurs either at or away from a region of interest, respectively. An advantage to this approach is that while a protective system would be primarily concerned with minimizing momentum at a specific location, maximizing momentum was chosen to be investigated here since it was more easily detectable experimentally.

The first optimization scheme presented here sought to maximize the momentum – calculated as the integral of the contact force over the time of the pulse – in two sets of three beads symmetrically on opposite sides of an 11x10 square array. The beads of interest were located at the numbered blue, green, and red circles (and their symmetric counterparts on the opposite wall) in Figure 5.6a. When the packing was subjected to a half-sine pulse with an amplitude of 8 kN and duration of 42.6 μs, the optimization scheme predicted that 46 cylinders situated as shown by the gray circles in Figure 5.6a would maximize *the sum of the total momentum* in the beads labeled 1, 2, and 3. Note that the combined momentum at Beads 1, 2, and 3 was not necessarily greater than the combined momentum of any other three beads in the system, but it was predicted greater for this configuration than the combined momentum at the same location (Beads 1, 2, and 3) for any other intruder configuration. Figure 5.6b plots the contact forces between each bead of interest and the wall when the 46 cylinders were optimally situated (the wall was modeled as a steel sphere with infinite radius). The color and number of each contact force curve correspond to the bead of the same color and number in the schematic. The orientation of the piezoelectric disk is indicated by the solid black line inside each of the colored circles.

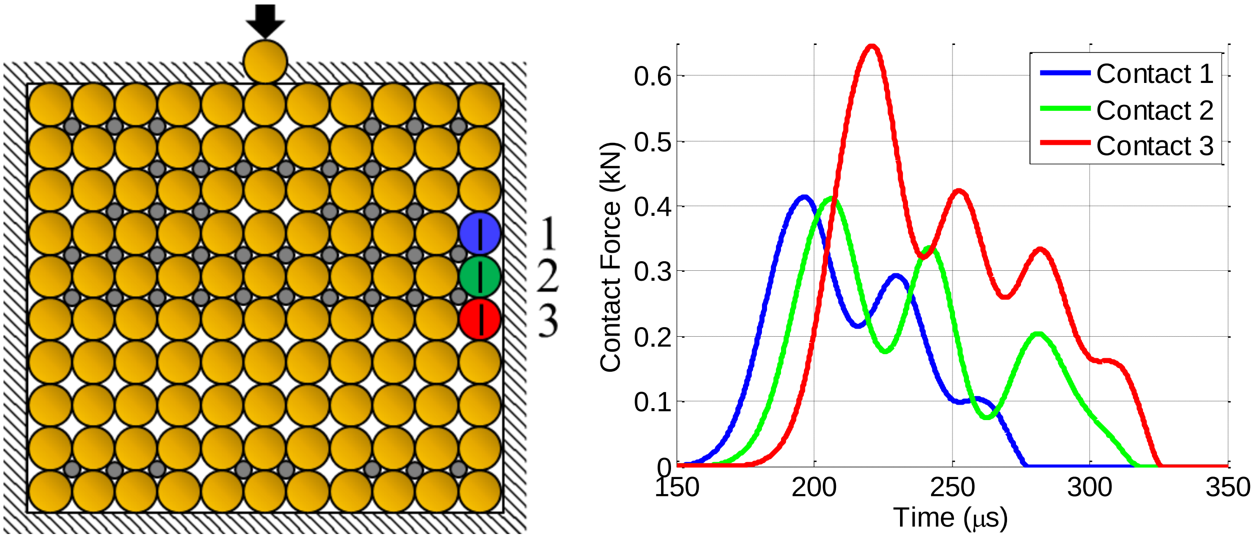

(a) (b)

Figure 5.6: (a) Location of interstitial cylinders to maximize the momentum at the blue, green, and red beads along the edge. (b) The simulated contact forces at the beads of interest.

Next we experimentally explored the contact forces by placing instrumented beads at locations 1, 2, and 3. Figure 5.7a plots the experimentally determined contact force between Bead 1 (blue in Figure 5.6) and the wall from multiple nominally identical experiments as well as the simulated contact force. Multiple experiments were performed here since it was found in Chapter 4 that variability in force records, even in nominally identical and carefully packed 2D arrays, can be significant. Figure 5.7b and Figure 5.7c are organized similarly, but with contact force for Beads 2 and 3, respectively. Each individual experiment is denoted by a letter in the legend such that the data from Experiment A displayed in Figure 5.7a-c are all from the same experiment. If a letter is not present in the legend, it indicates that the sensor recorded no signal at that location. The simulated contact forces had a much broader pulse width than the experimental results, immediately indicating that the momentum in the simulations was much greater than in the experiments. In fact, the sum of the simulated momentum of the three beads in the optimized case was 115 kN·µs while the average of the experimental one was 13 kN·µs. The simulated and experimental forces had similar force amplitudes at Beads 1 and 2, but Bead 3 had a much lower force amplitude, except for Experiment J. In Experiment J, the forces at Beads 1 and 2 is zero, possibly indicating that in that one experiment the entire load in the region of interest was directed at Bead 3. As was done in the 2D experiments presented in Chapter 4, we considered the arrival time and the peak force values as metrics for comparison between cases. The scatter in the magnitude of the peak forces and arrival times is summarized in Figure 5.8 and is comparable to the scatter seen in the results from the 2D packings in Chapter 4. The asterisks in Figure 5.8 are color coordinated to the force profiles in Figure 5.7.

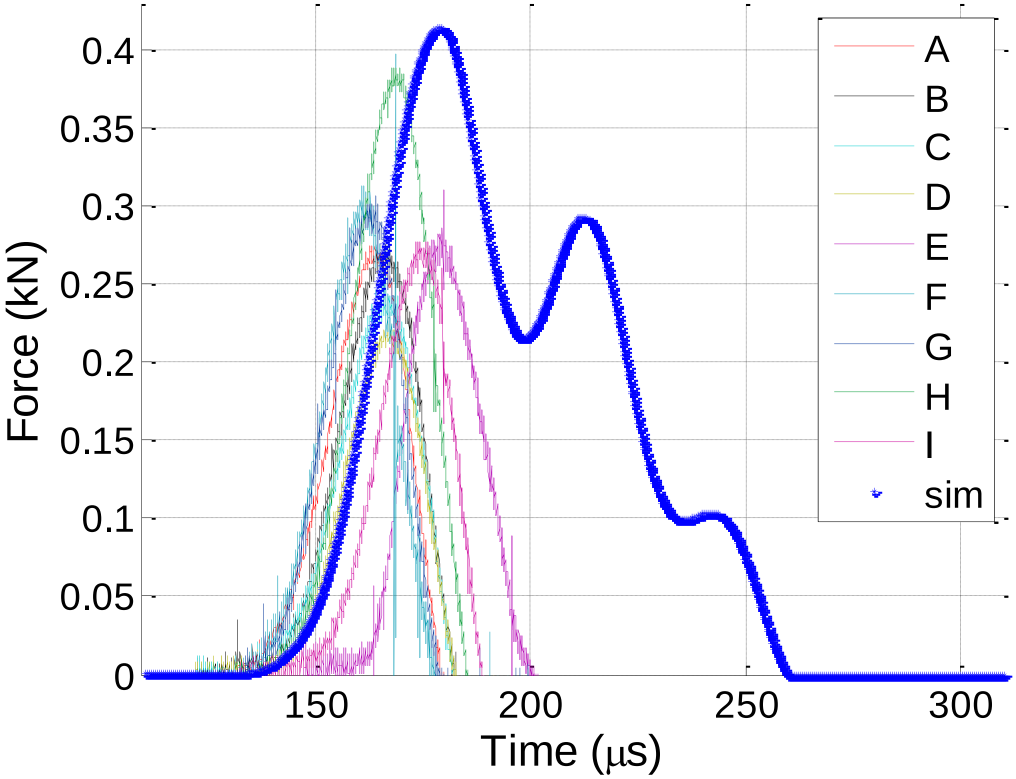

(a)

Figure 5.7 (cont.)

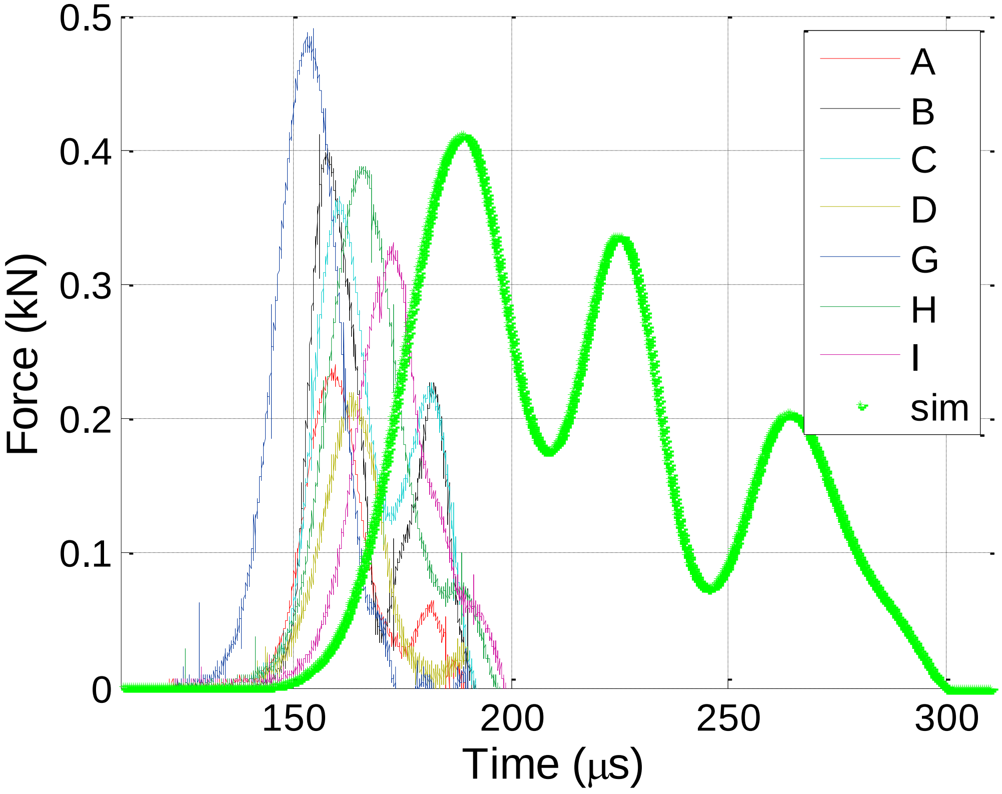

(b)

Figure 5.7 (cont.)

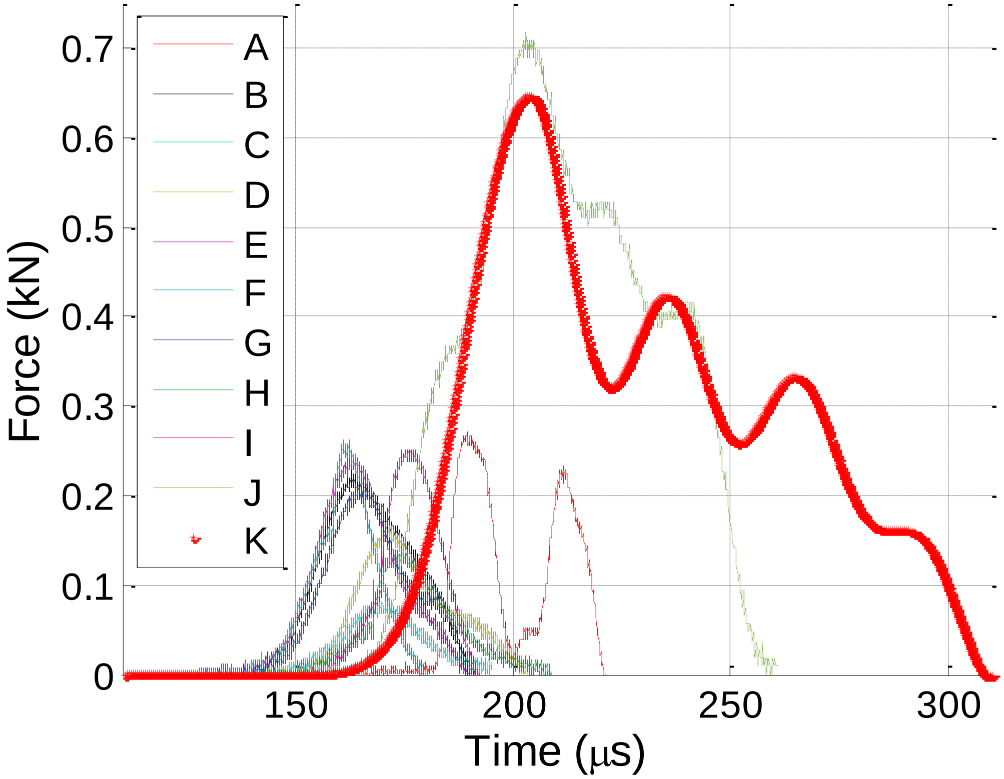

(c)

Figure 5.7: Comparison of experimental results with simulated result at Contacts (a) 1, (b) 2, and (c) 3.

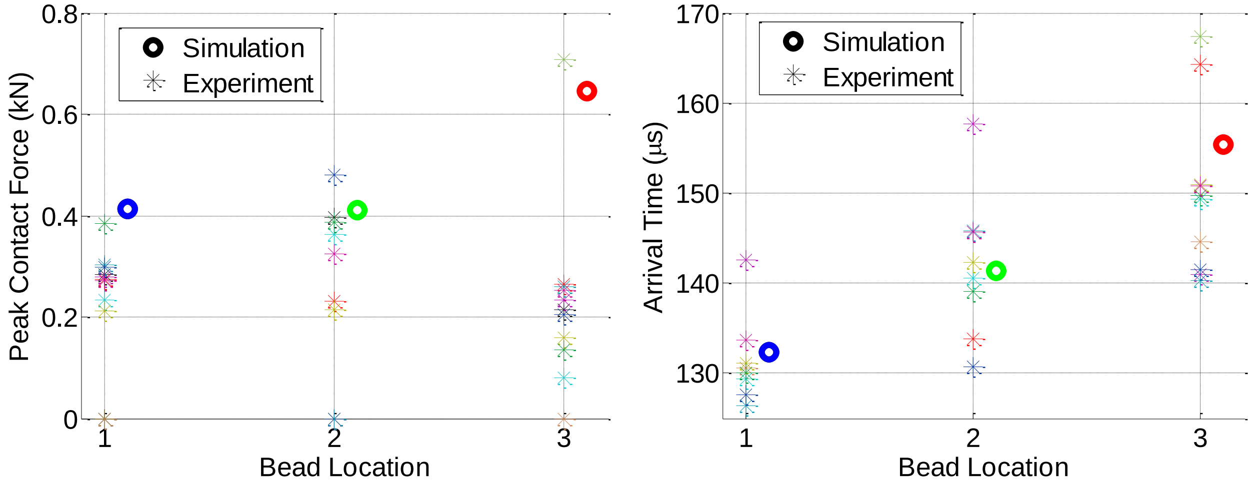

(a) (b)

Figure 5.8: Summary of the (a) peak contact forces and (b) arrival times at each location.

Ultimately, these results provide some validity to the constitutive models used to simulate the brass-brass and brass-cylinder interactions and demonstrate the extent to which the experimental and numerical results can be compared. Additionally, when compared to the square packing with no intruders discussed in Chapter 4, the results show that elasto-plastic stress waves can be redirected by placing cylinders at the interstitial locations and thus introducing coupling. The momentum values from the simulation were several times larger than the corresponding experimental values. It is difficult to ascertain whether the optimal conditions have occurred by testing alternate configurations since the momentum optimization involved optimizing both force and time. Next, we study force optimization only and contrast several different configurations to determine if a supposedly non-optimal state outperforms an optimal one.

5.4 Force Optimization Results from 14x13 Array

In this Section we explore several optimization schemes using the 14x13 array that also employs the WC adapter bar for loading. An attempt is made to determine if a given optimization configuration is truly optimal by comparing it to two baseline configurations – the case of no intruders and the case of full intruders.

Since the results for the momentum optimization shown above demonstrate that a direct comparison between simulation and experiments is limited due in part to the scatter in the experimental data, as detailed in Chapter 4, we will instead use the experiments to (a) suggest refinements in the choice of initial conditions (i.e., initial intruder placement) to achieve better optimization results, and (b) use the experimental results to investigate trends seen in the optimization studies rather than a deterministic comparison in a one-to-one manner.

5.4.1 Baseline configurations

Two baseline configurations were considered since they represented the extremes with respect to the quantity of cylinders located within the packing. The case of no cylinders was the simplest to construct and its elasto-plastic response has been investigated in detail in Chapter 4. Here we repeated the experiments with the particular array shown in Figure 5.9a, which also shows three instrumented beads of interest and the sensor orientations at each of those three locations. The simulated contact forces experienced at the top left (black) and right (blue) corner and the two bottom beads (magenta) are shown in Figure 5.9b and experimentally in Figure 5.9c and the same propagation pattern is seen as for the square packing in Chapter 4. We note for reference that the peak simulated force at the bottom sensor was 2.5 kN. The contact forces in the simulations were much larger than in the experiments, possibly indicating that the model under predicts dissipation.

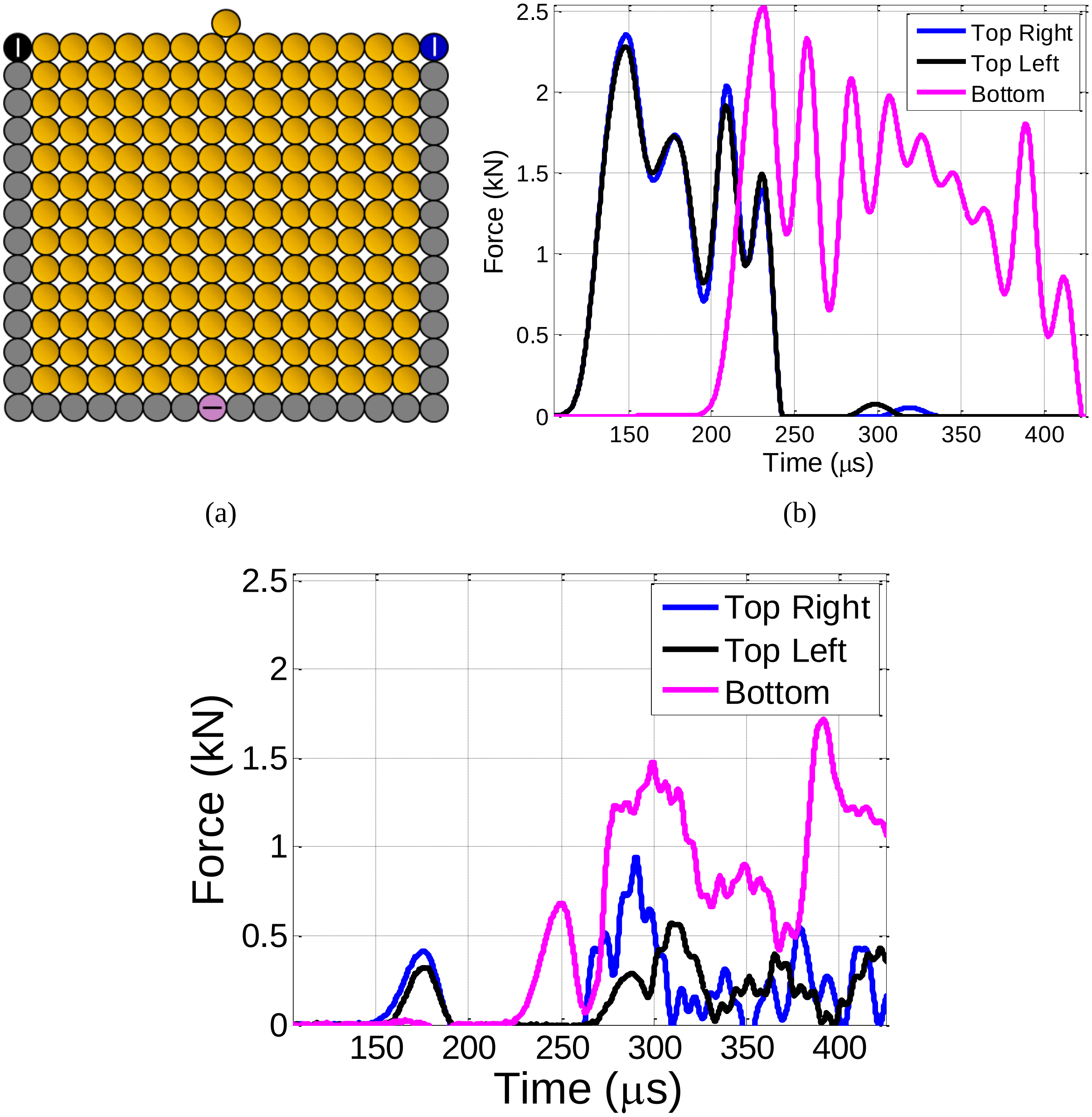

(a)

(b)

(c)

Figure 5.9: (a) Sensor locations in 14x13 brass array setup with no intruders. (b) Simulated and (c) experimental contact forces at the indicated locations.

The other baseline configuration was the case where intruders were present at all 156 interstitial locations. A schematic of this configuration and the simulated contact force profiles under an input loading of 15 kN (typical input signals for the force optimization experiments are in Figure 5.4) at 5 selected locations are shown in Figure 5.10a-b, and the corresponding experimentally measured contact forces at Beads 1-5 are shown in Figure 5.10c. Beads 4 and 5 were symmetric with respect to the impact and their profiles overlap exactly in Figure 5.10b. Useful reference values are the simulated peak contact force from the three beads on the lateral side, 200 N at Location 1 (red), and the peak contact force at Beads 4 and 5, which is 365 N.

We see similar trends between the experiments and simulations with respect to peak force and arrival times. The contact forces at the lateral beads decreased with distance from impact, while the force experienced at the bottom of the packing was symmetric. In both the experiments and the simulations, the largest force was experienced is at Beads 4 and 5.

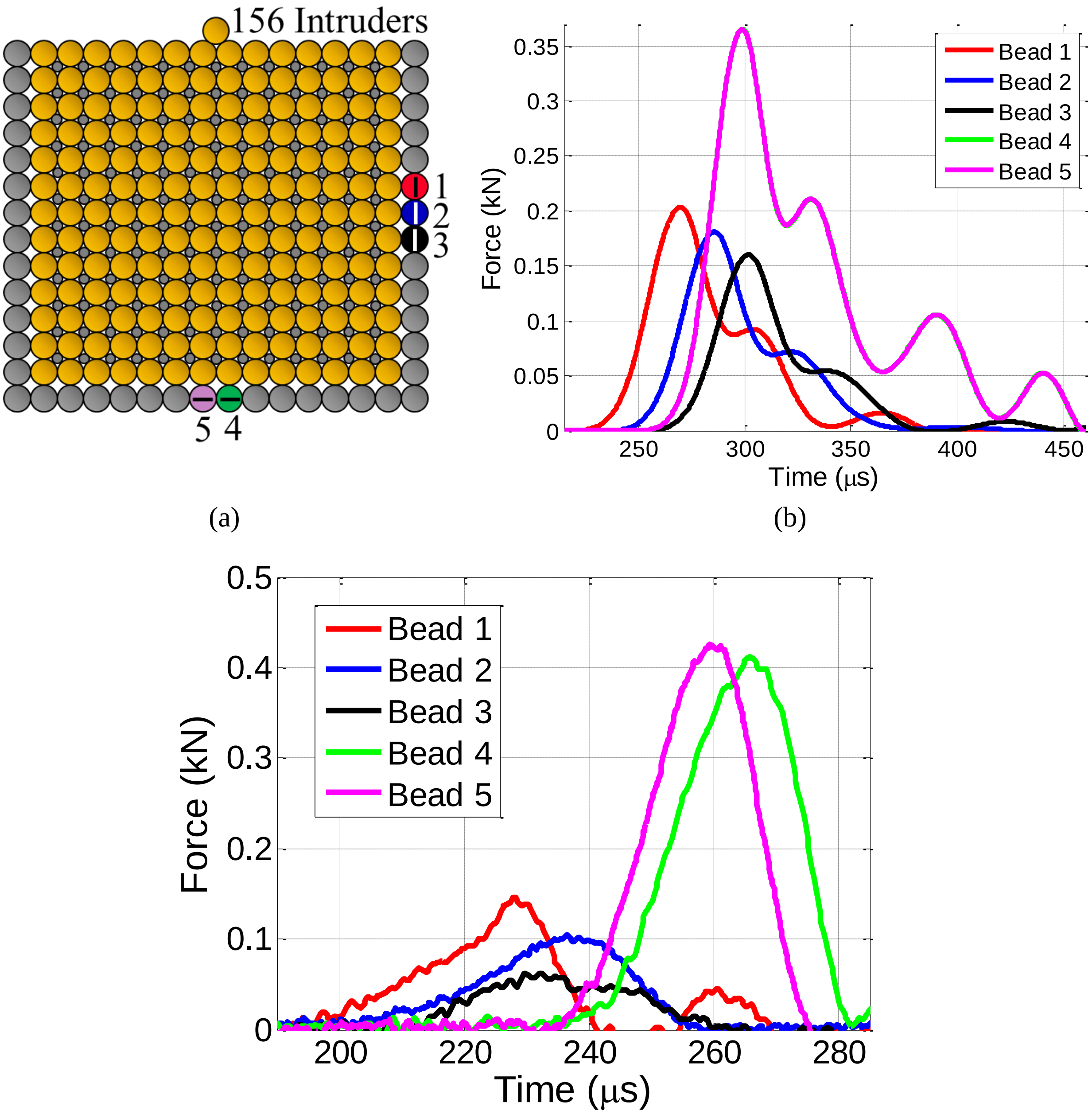

(a)

(b)

(c)

Figure 5.10: (a) Baseline scenario where all interstitials are filled with intruders. (b) Simulated and (c) experimental contact forces at the indicated locations. Note that in (b) the simulated force profile for Bead 4 is obscured by the Bead 5 profile since they overlap (they are identical due to symmetry).

5.4.2 Lateral force maximization

First, we investigated a proposed configuration of intruders that numerically maximizes the contact force at the three beads labeled 1, 2, and 3 in Figure 5.11a. Note that the force optimization as not symmetric; that is, it did not maximize the force at the symmetric counterparts of Beads 1, 2, and 3 along the left side of the packing (unlike the momentum optimization studied in Section 5.3). Figure 5.11a also shows the locations of the six intruders that satisfy the optimization (gray circles), as well as the locations of the instrumented beads (numbered) with the orientations of the piezoelectric disk within each instrumented bead (solid black or white line). Figure 5.11b-c displays the contact forces from the simulation and experiment, respectively, and both show that, in the region of interest, only Bead 1 experienced a contact force. The peak simulated contact force at Bead 1 was 310 N, which was greater than the peak simulated contact force in the full intruders baseline case (200 N), so the two results were consistent in that the optimized result had a higher peak force than a non-optimized one. We note this consistency here as it will not always be the case in the other configurations. As will be seen, 310 N was higher than any of the other contact forces seen at Beads 1, 2, and 3 in the remaining configurations, strengthening the argument that this arrangement of cylinders maximizes the peak contact force in the prescribed region. Note that the opposite case to maximizing the lateral force at a particular location(s), i.e., the configuration that *minimizes* the lateral force, is actually the baseline case of the cardinal square brass beads with no intruders since in that case no force is experienced at Beads 1, 2, and 3 due to the lack of lateral coupling in the system. We note that the lateral force minimization configuration was only verified experimentally and not numerically. Furthermore, there could be other arrangements of cylinders that produce no force at the beads of interest as there is no guarantee of uniqueness in the optimized solutions.

The result of the optimization is the layout of intruders that maximizes the peak force experienced at any one bead in the region of interest (i.e., the optimization does not maximize the sum of the three contact forces). As such, it is reasonable that the contact force was maximized at the location closest to impact since there were the fewest number of contacts to dissipate the wave, and, additionally, that the force was only present at one bead since more interstitial cylinders would be needed to spread the wave to Beads 2 and 3, and consequently reduce the amplitude by further spreading. Indeed, if the optimization had been to maximize the force at just Bead 1, the resulting layout of intruders would be the same.

The trends were similar between the experiments and the simulations. The simulations predicted larger contact forces, which was in part due to the lack of friction. Additionally, the wave arrived at Bead 1 before Beads 4 and 5 in the experiments, but slightly after Beads 4 and 5 in the simulations, although this may have to do with relative amplitudes since the primary force peaks recorded at Beads 4 and 5 experimentally were much less proportionally, and this affects wave speeds. Note, however, that the presence of the intruders siphoned energy from the right-center chain (vertical chain of beads between the loading bead and the Bead 4) and therefore a corresponding decrease in force was seen at Bead 4 compared to Bead 5 – a clear example of high-amplitude wave redirection – both in the simulations and in the experiments. It was precisely this energy diversion from the right-center chain that leads to the increased force recorded at Bead 1.

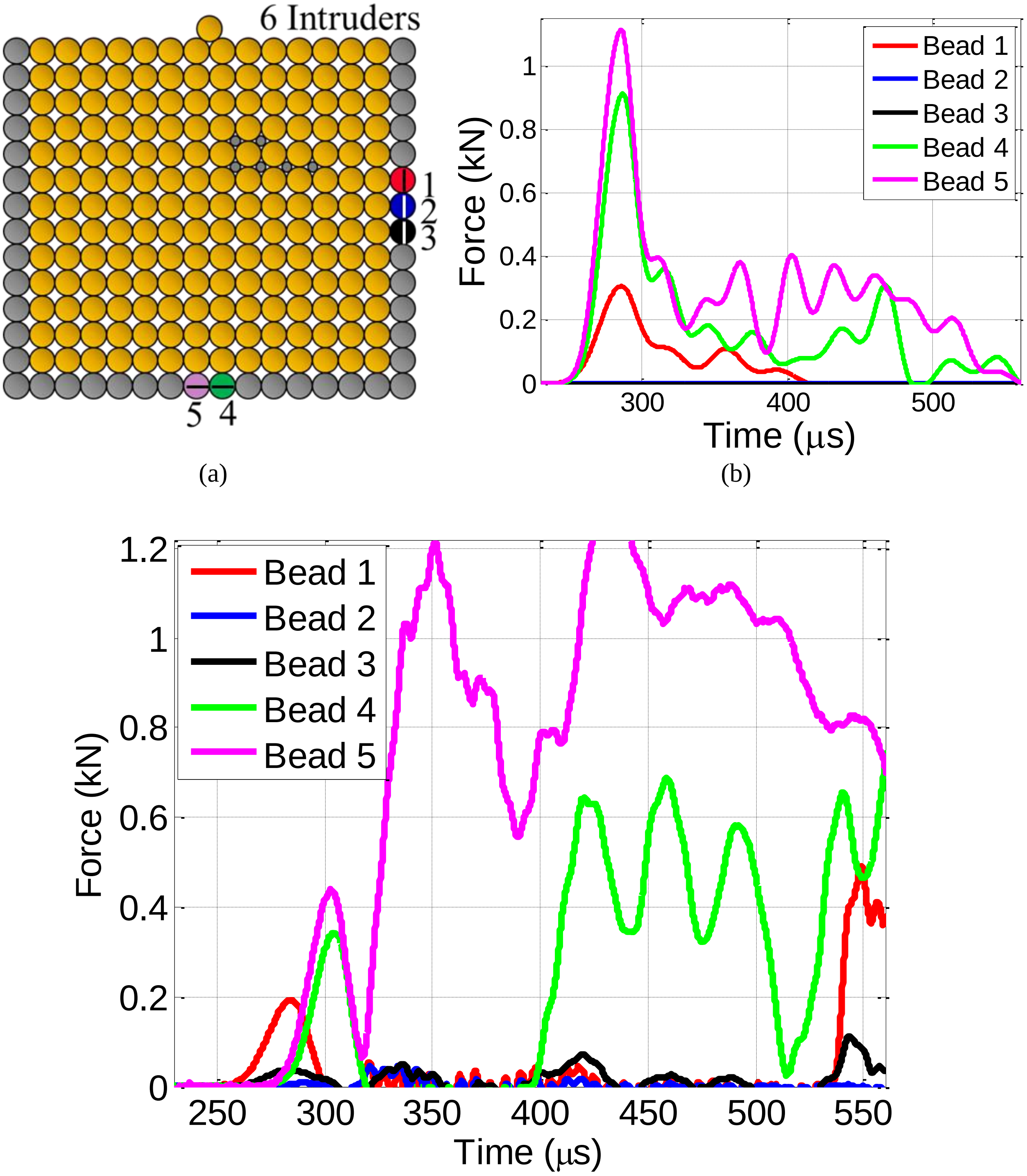

(a) (b)

(c)

Figure 5.11: (a) Schematic of the cylinder placement that maximizes the contact force at beads 1, 2, and 3. (b) Simulated and (b) experimental contact forces.

5.4.3 Bottom force minimization

An alternate, and perhaps equivalent, problem to maximizing lateral force that was considered was to *minimize* the peak contact force that was experienced at Beads 4 and 5, i.e., directly across from the loading point. The optimization scheme sought the arrangement of cylinders that minimizes the peak force at *one* of the beads (i.e., it does not minimize the sum of the peak contact forces). The resulting numerically predicted optimal intruder arrangement for minimum peak force in Beads 4 and 5 is presented in Figure 5.12a, where the same details apply as in previous figures for the instrumented bead locations and piezoelectric disk orientations. Figure 5.12b-c shows the contact forces at the 5 beads as determined by the simulation and experiment, respectively. There was good agreement between the two sets of results at all locations except Bead 4, which would ideally be similar to Bead 5 since the intruder arrangement is symmetric. As was the case for the lateral force maximization, the simulations generally provided larger peak forces than recorded in the experiments, and predicted the wave to reach Beads 4 and 5 prior to Bead 1 (again, perhaps due to the relative difference in the amplitude of the wave at Beads 4 and 5 between the simulation and the experiments).

Note that the simulated peak force at Beads 4 and 5 was 471 N in the simulation. This load value was actually *higher* than what was observed at the same locations in the baseline configuration of full intruder packing (365 N), although the current configuration was meant to *minimize* the peak force there. Therefore in this case, the optimization clearly did not provide a global minimum and we can conclude that it has converged to a local minimum. The optimization scheme was attempting to solve a highly nonlinear problem and it had no means of verifying if it had reached the global minimum. Here we demonstrably confirmed that the optimized state for the bottom load minimization was a local minimum that permitted a contact force that was 29% greater than the baseline case of full intruders but also reduced the load by 81% from the baseline case of no intruders (the configuration that maximizes the peak contact force at the bottom).

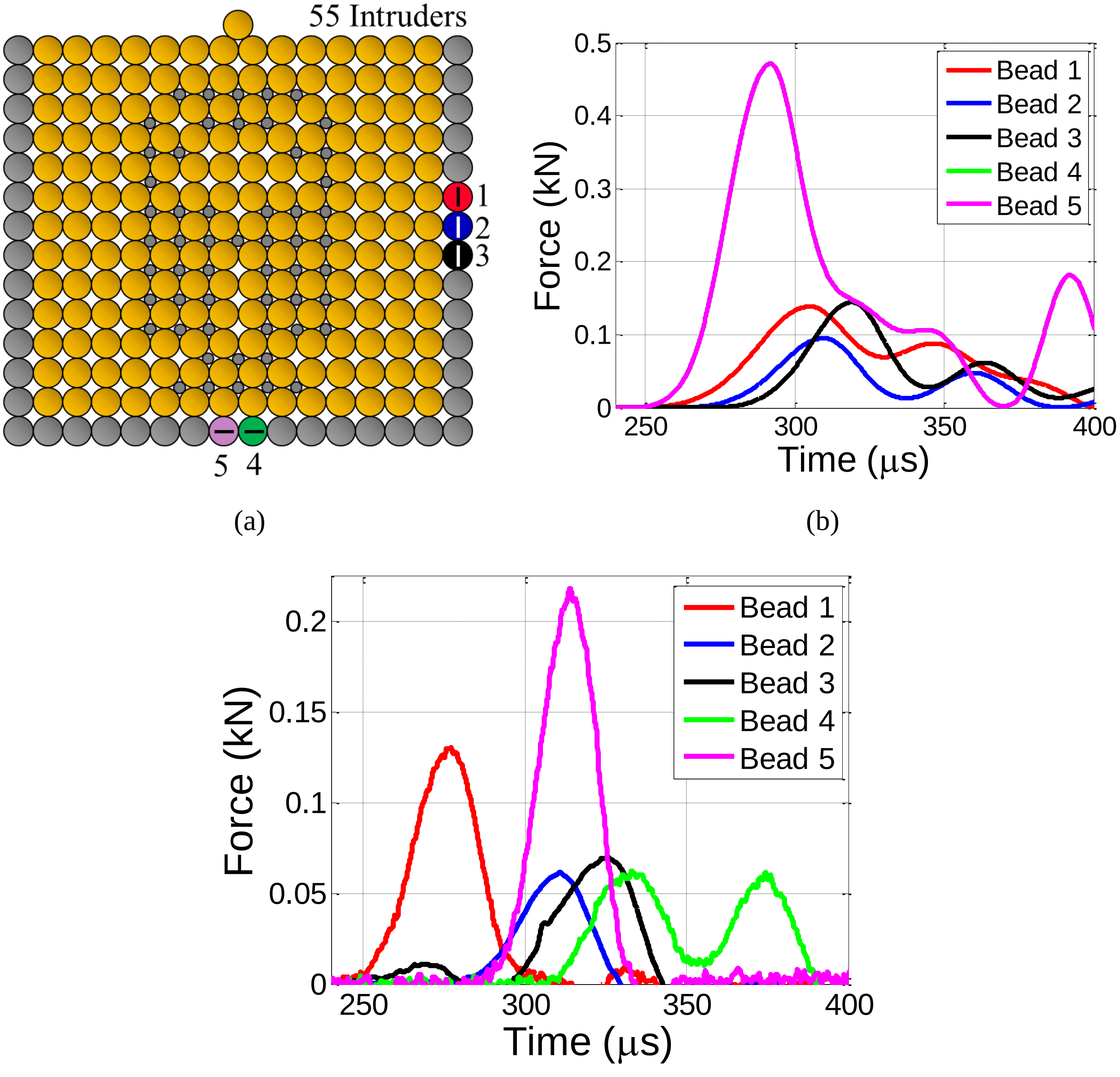

(a)

(b)

(c)

Figure 5.12: (a) Schematic of the cylinder placement that minimizes the contact force Beads 4 and 5. (b) Simulated and (b) experimental contact forces.

5.4.4 Lateral force maximization and bottom force minimization

Of greater practical interest may be the ability of the scheme to simultaneously perform two optimizations, namely to determine the configuration that maximizes the contact force in Beads 1, 2, and 3 while *at the same time* minimizing the contact force in Beads 4 and 5. In this case, the optimization scheme returned a configuration with 23 intruders arranged as shown in Figure 5.13a. Figure 5.13b plots the simulated contact forces while the results from two separate nominally identical corresponding experiments are presented in Figure 5.13c-d. The two sets of experiments were consistent with each other (with the exception of the arrival time at Bead 3) and were comparable to the numerical results in terms of peak force amplitudes and arrival times at the lateral beads.

The simulated peak forces were 430 N (minimized) at the bottom two and 180 N (maximized) at the lateral three beads of interest. The lateral peak force of 180 N was lower than both the baseline case of full intruders (200 N) and the solely laterally optimized case (310 N). Meanwhile the contact force at the bottom (430 N) was greater than the full intruder case (365 N) but lower than the solely bottom minimization case (471 N). The case of full intruders was demonstrably a better solution so this lateral maximization/bottom minimization solution was another local minimum. As there was no constraint on the quantity of intruders in the optimization scheme, it is unclear why the optimization did not choose to place more beads in the bottom half of the packing to further dissipate the wave. However the fact that the two baseline cases form the two extreme limits of the optimization space may have some significance.

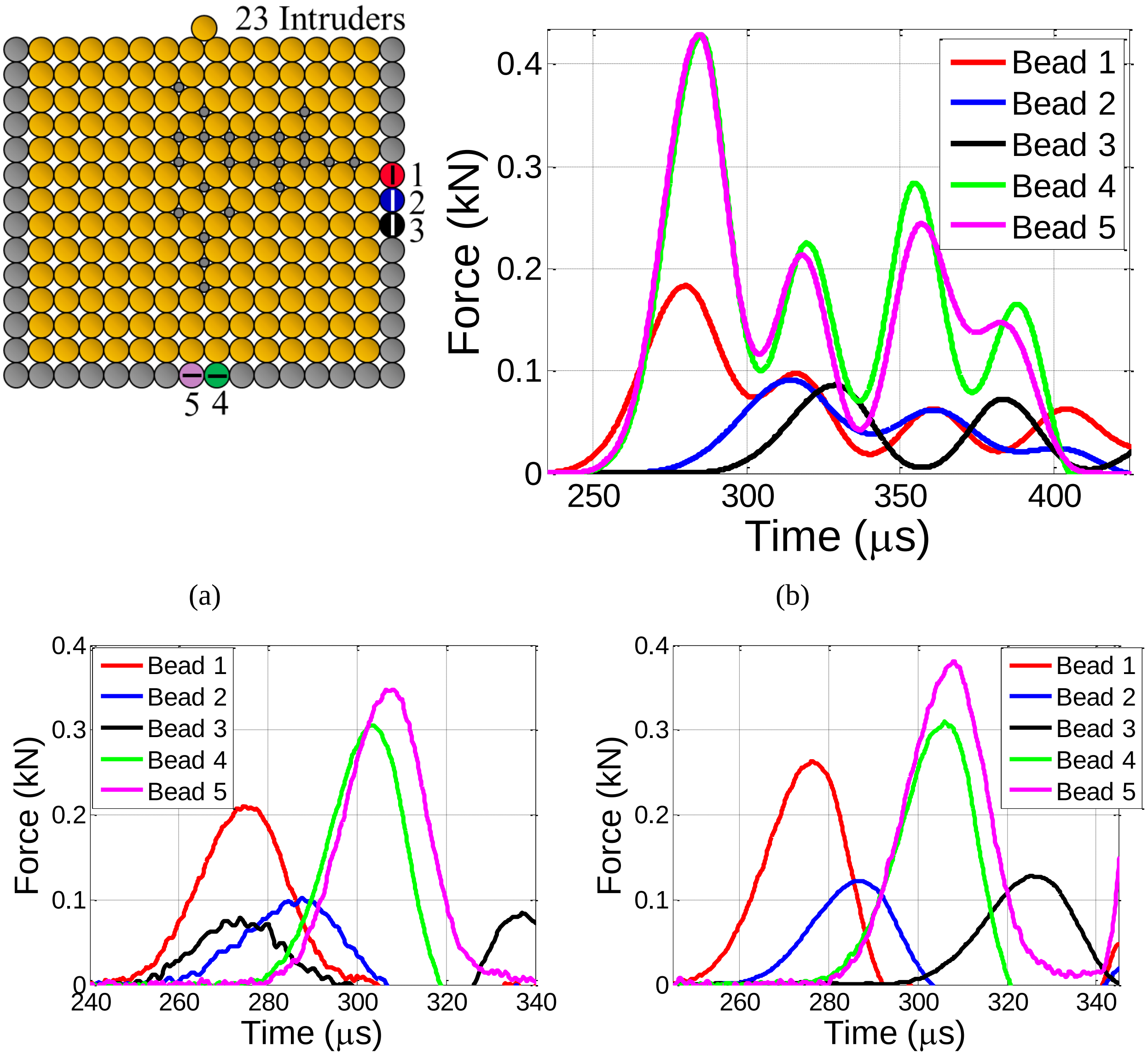

(a) (b)

(c) (d)

Figure 5.13: Simultaneous force maximization at Beads 1, 2, and 3 and force minimization at Beads 4 and 5. (a) Intruder and instrumented bead locations. (a) Simulated contact force histories. (c) and (d) The results from two nominally identical experiments.

5.4.5 Force maximization at three non-adjacent beads

The final optimization of interest here was the case of *maximizing* the contact forces at three specific beads along the bottom of the packing. In this case, the multi-objective optimization scheme attempted to maximize the contact force at all three locations. Thus we lost our relatively intuitive approach of checking if a solution was globally optimized by comparing the relevant peak contact forces in a given region between configurations. In fact, there was not a way to easily interpret the problem physically, so we introduce the cost function that was to be minimized:

$$\Psi_0(\boldsymbol{p}) = -\sum_{j=1}^{3}\left(\int_{\mathrm{T}}\left(F_{jw}(t,\boldsymbol{p})\right)^{P}\,\mathrm{dt}\right)^{1/P}. \tag{5.1}$$

The goal of the optimization was to minimize the optimization number Ψ_0 for some configuration of intruders $\boldsymbol{p}$. The contact force is denoted by F_{jw} where the subscript denotes the contact between the j^{th} bead and the wall (w). The time domain is denoted by T and each time point by t. Finally, the exponent P is associated with the p-norm operation which is differentiable, a condition required for the optimization scheme and not satisfied by a simple sum.

Thus the optimization was seeking to maximize the sum of the p-norms at the three beads of interest. In other words, the optimal solution was not the case without any intruders because the scheme in this case was not trying to maximize just one contact force in a region. Thus when comparing outcomes for the asymmetric force maximization, we must compare the values of the minimized cost functions. We note that values of Ψ_0 could have been calculated for the previous cases, but they did not provide any further information regarding the relative optimal states of the configurations since each of the prior cases had a physically intuitive method for comparison.

The contact forces at the three beads along the bottom row in Figure 5.14a labeled (and colored) 1 (black), 2 (blue), and 3 (red) were to be maximized simultaneously. The predicted interstitial cylinder placement arrangement that accomplished this optimization is also presented in Figure 5.14a and the resulting simulated contact forces are shown in Figure 5.14b. Three nominally identical experiments were performed for this configuration. The results for each experiment (and the simulation) are compared by bead number in Figure 5.14c (i.e., the left-most pane in Figure 5.14c shows the results at Bead 1 for the three experiments and the simulation). The experimental results were generally consistent across the three experiments. The peak contact forces diminished with distance from the impact in all cases such that Bead 2 experienced the highest contact forces, followed by Bead 3, and then Bead 1.

We recognized that the intruders on the left and right of the packing were necessary to allow the stress waves travelling along the top row to be redirected towards Beads 1 and 3. However, the intruders that were placed in the central column of interstitials seemed at ends with the goal of maximizing the contact forces since they dissipate the energy that reaches Bead 2. At this point we proposed an iterative approach to retrieve improved results from the optimization scheme.

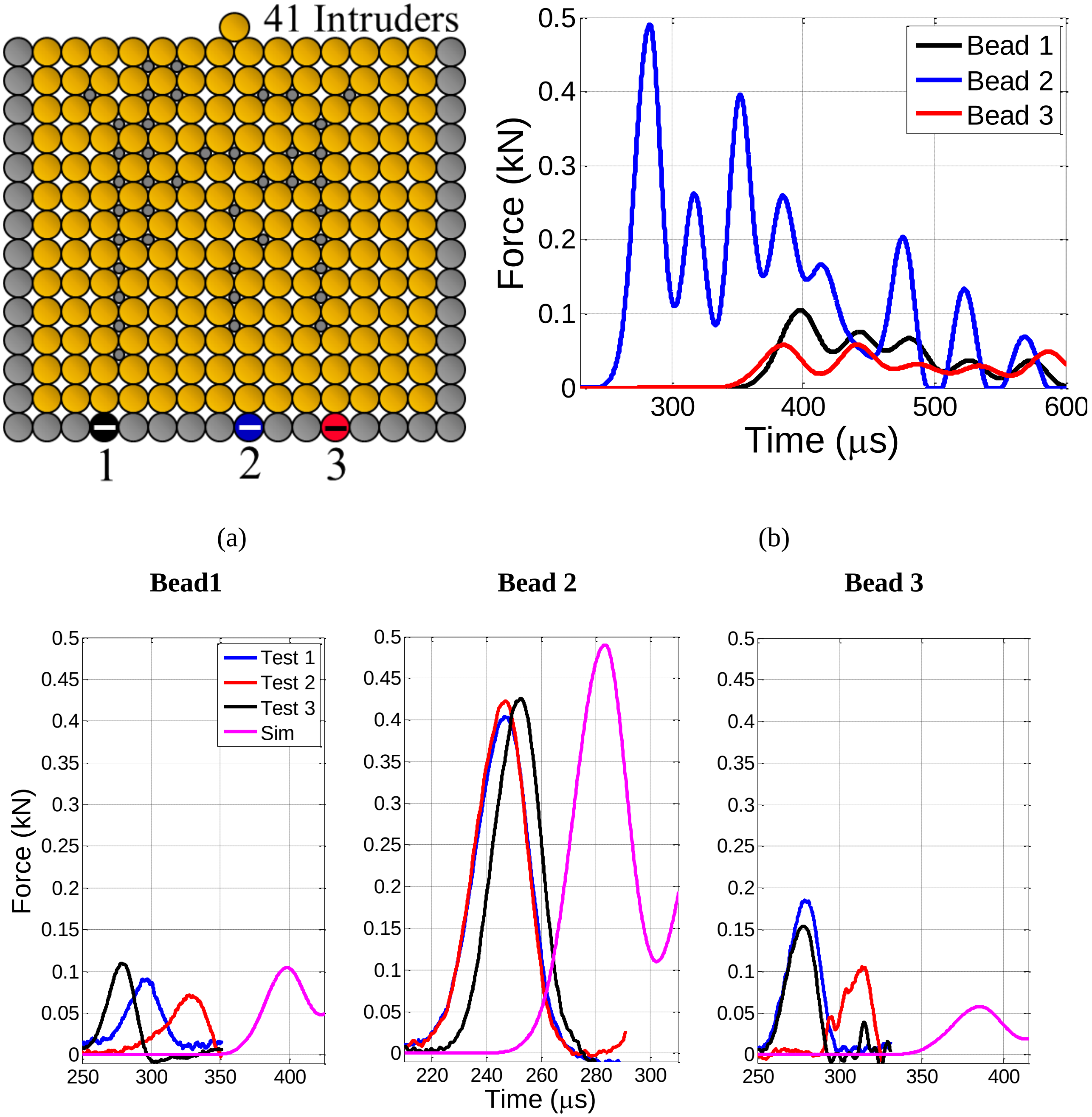

(a)

(b)

(c)

Figure 5.14: Asymmetric force maximization. (a) Intruder placement and location of the contacts to be optimized. (b) Simulated force results. (c) Force measurements from three nominally identical experiments ("Test") and the simulated contact force plotted at each bead location.

Iterative approach

At the beginning of the optimization scheme, every interstitial has the potential to include an intruder. We sought to improve upon the optimization by suggesting that the central column of interstitials forbid the presence of intruders, as intruders in those locations would likely hamper the wave that arrives at Bead 2. In order to compare the resulting setups, we needed to calculate the cost function for the asymmetric bottom force maximization, Eq. 5.1.

At this point we compared the existing optimization result (Figure 5.14a) with the proposed improved result, shown in Figure 5.15a, where the central intruders have been removed. Performing another optimization using the configuration in Figure 5.15a as the initial guess (and forbidding the presence of intruders along the central column), resulted in the configuration in Figure 5.15b. Table 5.1 shows the optimization number Ψ_0 for the listed asymmetric force maximization configurations, where a more negative number indicates a better optimization. We see that the original optimization result was worse than both baseline configurations. The optimization was indeed improved by our intuitive approach of removing the intruders along the central column and the additional optimization using Figure 5.15a as an initial guess further improves upon the results, reaching perhaps the true global minimum.

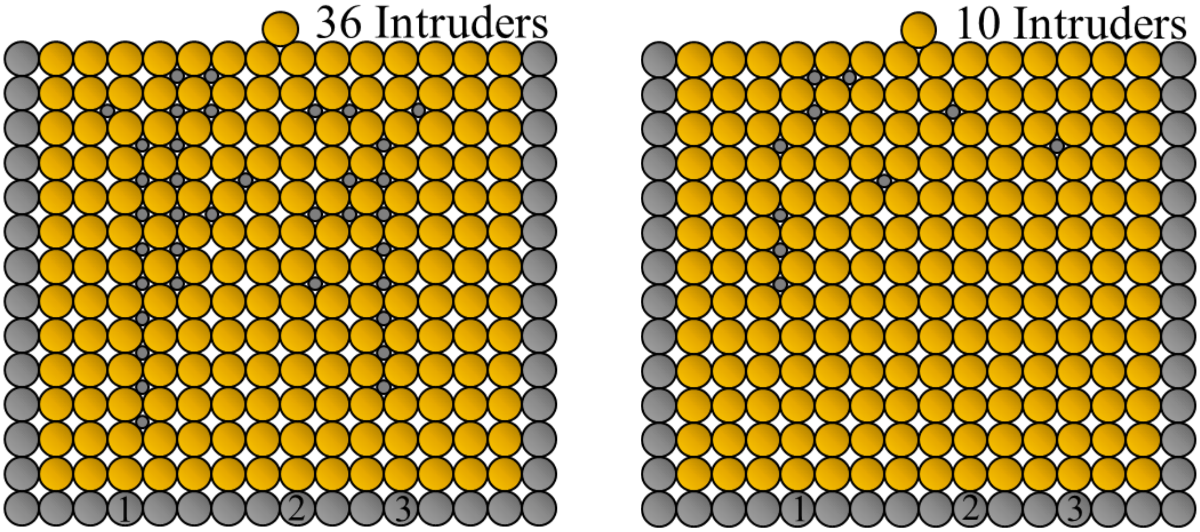

(a) (b)

Figure 5.15: (a) Intruders along the central column have been removed from the initial optimized result in Figure 5.14a. (b) Cylindrical placement after a new optimization is performed using the configuration in Figure 5.15a as the initial condition.

Table 5.1: Optimization number, Ψ_0, for the asymmetric force maximization configurations.

Configuration	Ψ_0	**Reference Image**
No intruders (Baseline)	-2.68	Figure 5.9a
Full intruder (Baseline)	-1.42	Figure 5.10a
Original optimization	-0.69	Figure 5.14a
Simulation with cylinders along the central column removed	-2.85	Figure 5.15a
Optimization using above simulation as initial guess (and prohibiting intruders in the central column)	-2.88	Figure 5.15b

5.5 Conclusions

The optimization scheme sought to solve a nonlinear objective function using a gradient based approach. Thus a frequent occurrence was that the optimization converged to a local minimum. Indeed, the optimization scheme had no means of verifying if it had reached the global minimum (i.e., the ideal cylinder placement for a given problem). An iterative scheme was proposed that fine-tuned the optimization by making informed choices about which interstitials should have or not have intruders rather than initiating each interstitial as a possible location for an intruder. An additional optimization can then be performed to see if the "informed packing" proved to be a better result. For one case study, the initial guesses of the quantity and location of the interstitial intruders significantly improved the optimization. Utilizing this informed packing approach may also reduce the number of cylinders (and thus cost and weight of a system) required to achieve a goal. For instance, the maximum momentum configuration proposed in Figure 5.6a may be equally valid if the eight cylinders located along the bottom row were removed. Similarly, it may be possible to minimize the peak contact force at the bottom of the packing in Figure 5.10 by placing intruders along the central three columns instead of all 13.

In keeping with our overall objective of elasto-plastic wave management in granular systems, we note that the cylinders were successfully utilized to redirect the incoming wave. Multiple experiments in a given configuration confirmed the repeatability of this method of wave tailoring. Furthermore, the simulations and experimental results were generally comparable, thus validating in part an important numerical model that can be used to construct even more complicated systems for wave management and mitigation.

6. WAVE TAILORING IN A HEXAGONAL SYSTEM BY PRECONDITIONED CONTACTS

In this Chapter we continue to pursue our objective of constructing a material system that can directionally manage, in addition to mitigate, an elasto-plastic wave such that it can be guided away from sensitive components. In addition to using intruders at interstitial locations to tailor wave propagation within a granular packing, it is also possible to selectively tailor wave propagation using preconditioned contacts. In this way, an ordered granular system containing a mix of non-preconditioned (i.e., unaltered) and preconditioned contacts can be tailored to exhibit faster wave speeds and higher amplitude wave propagation in certain regions, while promoting plastic dissipation in other regions. A drawback of such a combined system is that since the preconditioned spheres are geometrically different from the non-preconditioned ones, there are geometric constraints as to how the two can be fit together into one ordered system. Therefore by necessity, our investigations were limited to only a few 2D configurations that did not produce gaps between beads. However this is a technological challenge rather than a scientific one that may be overcome in the future by having different ways of preparing the preconditioned beads.

6.1 Horizontal Preconditioning

6.1.1 Comparison with a non-preconditioned system

We begin by studying the hexagonal system first introduced in Chapter 4, namely a hexagonal packing containing 11 rows in which the first row (the row closest to impact) contained 10 beads and subsequent rows alternated between 9 and 10 beads with a loading bead placed symmetrically in contact with the 5th and 6th beads of the first row as seen in the photograph in Figure 6.1 (or schematically in Figure 4.1b). The load frame and mechanism used are described in Sections 2.1-2.2, with the stainless steel adapter bar initially in use. All of the brass beads were uniformly preconditioned to 9 kN (i.e., two diametrically opposite contacts on each sphere were preloaded to 9 kN) using the technique described in Section 3.2.2. In each row, the preconditioned contacts were arranged such that a line passing through them was perpendicular to the direction of the input load – a configuration dubbed “horizontal preconditioning”. Note that in the horizontally preconditioned configuration there were also contacts that were not preconditioned, namely the ones diagonally across each bead. Figure 6.1 shows a photograph of a horizontally preconditioned system and close-ups between the contact of two non-preconditioned spheres and the relatively larger contact area of two preconditioned spheres.

Figure 6.2 shows the force histories measured experimentally at three locations in a horizontally preconditioned system (top plot, peak input load ~6 kN) and a hexagonal system with no preconditioned contacts (bottom plot, peak input load ~10 kN). The force histories were obtained from the instrumented beads which are shown in the inset of Figure 6.2 as a red, green, and blue circle, with the solid lines indicating the piezoceramic disk orientation, and hence the direction of the force component measured was perpendicular to this orientation. As before, when analyzing the force histories, we focused our attention on the primary pulse peak and the arrival time.

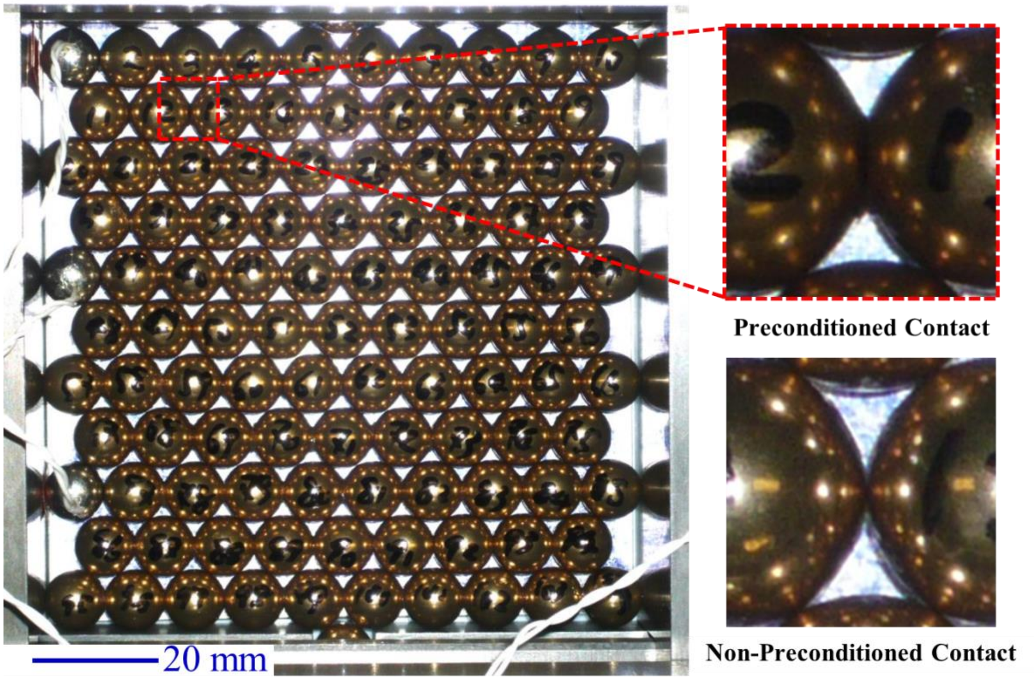

Figure 6.1: Photograph of the horizontally preconditioned packing with close-ups of a preconditioned contact and a non-preconditioned contact.

Relative to the input load, the peak amplitude of the primary wave that was detected by Sensor 1 was greater in the horizontally preconditioned configuration (18% of peak input load) than the non-preconditioned system (8% of peak input load), suggesting that less dissipation occurred along the preconditioned row. We also observed that the higher amplitude wave in the preconditioned system arrived earlier than the lower amplitude wave in the non-preconditioned system, a result of the force-dependent wave speed. (The initial time, $t = 0$, corresponded in both cases to the triggering of the data acquisition system by the same threshold voltage detected in a strain gage on the Hopkinson bar.) At Sensor 2, located at the end of a diagonal chain directly in contact with the loading bead, the peak force amplitude of the primary peak relative to the input load was about 3% for the preconditioned system and 5% for the non-preconditioned system. Note that the contact points along this diagonal were not preconditioned in both these systems. Therefore it was reasonable to expect similar wave mitigation responses. However, as we will see, a larger portion of the input load was consistently experienced at the terminus of the diagonal in the non-preconditioned packing than the horizontally preconditioned packing. The disparity in peak forces that reached the end of the diagonal indicated that, for an elasto-plastic wave travelling along the diagonal, the preconditioned contacts enabled more energy to be diverted from the diagonal than the non-preconditioned contacts.

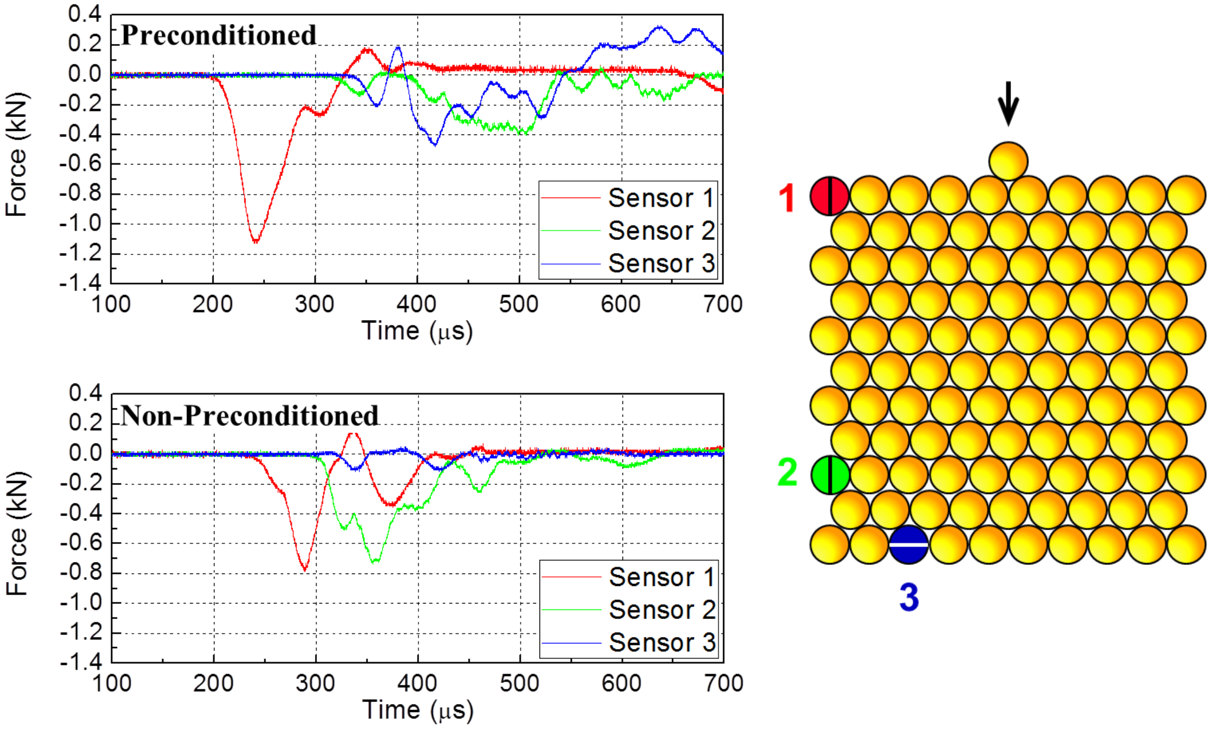

Figure 6.2: Comparison of signals between a preconditioned and non-preconditioned setup.

Figure 6.3 shows the yield maps of both configurations. The yield map was constructed by identifying which contacts yielded by examining each bead under an optical microscope post-mortem (the bead locations were indicated by a felt-tip marker prior to loading, as seen in Figure 6.1). A bead that had visibly yielded is shaded blue and the specific contact that had yielded is denoted by a red box. Figure 6.3b compares the calculated contact forces along the diagonal chains in the preconditioned and non-preconditioned systems. The contact forces were initially much higher than in the non-preconditioned system and remained higher along most of the length of the chain, although to a lesser extent as the distance from impact increased. As mentioned earlier, it was possible for a bead to have yielded and not have a visible yield area since the bead may have yielded internally. Therefore the yield maps shown in Figure 6.3b are potentially underestimates. The horizontally preconditioned system exhibited a different behavior when compared to the non-preconditioned system in that plasticity was concentrated in the chains of spheres that were diagonally in contact with the impact point, rather than being more widely dispersed throughout the impact region. Figure 6.2 and Figure 6.3 suggest that in the horizontally preconditioned system, the elasto-plastic waves primarily travelled down the two 60° chains and preferred to travel away from the center of the packing using the preconditioned contacts. Previous experimental and numerical works state that a load travelling along one of the 60° chains cannot be transferred to a contact that is at angle greater than 90° relative to a line passing through the 60° chain [106,107]. Thus, it was not expected that an elasto-plastic wave travelling along a 60° chain was deflected toward the center of the packing via the preconditioned contacts. We term the ability of controlling the regions that experience plasticity, in this case by use of preconditioned contacts, "directional plasticity" and it will be explored further in the subsequent configurations.

Numerical work has shown that an ordered granular medium is more efficient at dissipating energy than an equivalent continuum medium because the stress concentrations at the contacts cause the granular medium to yield at loads that would pass through a continuum medium elastically [86]. Preconditioning enables us to tailor which contacts will yield, thus maximizing the plastic dissipation. Conversely, we can choose which contacts will not yield, maximizing the passage of an elastic wave.

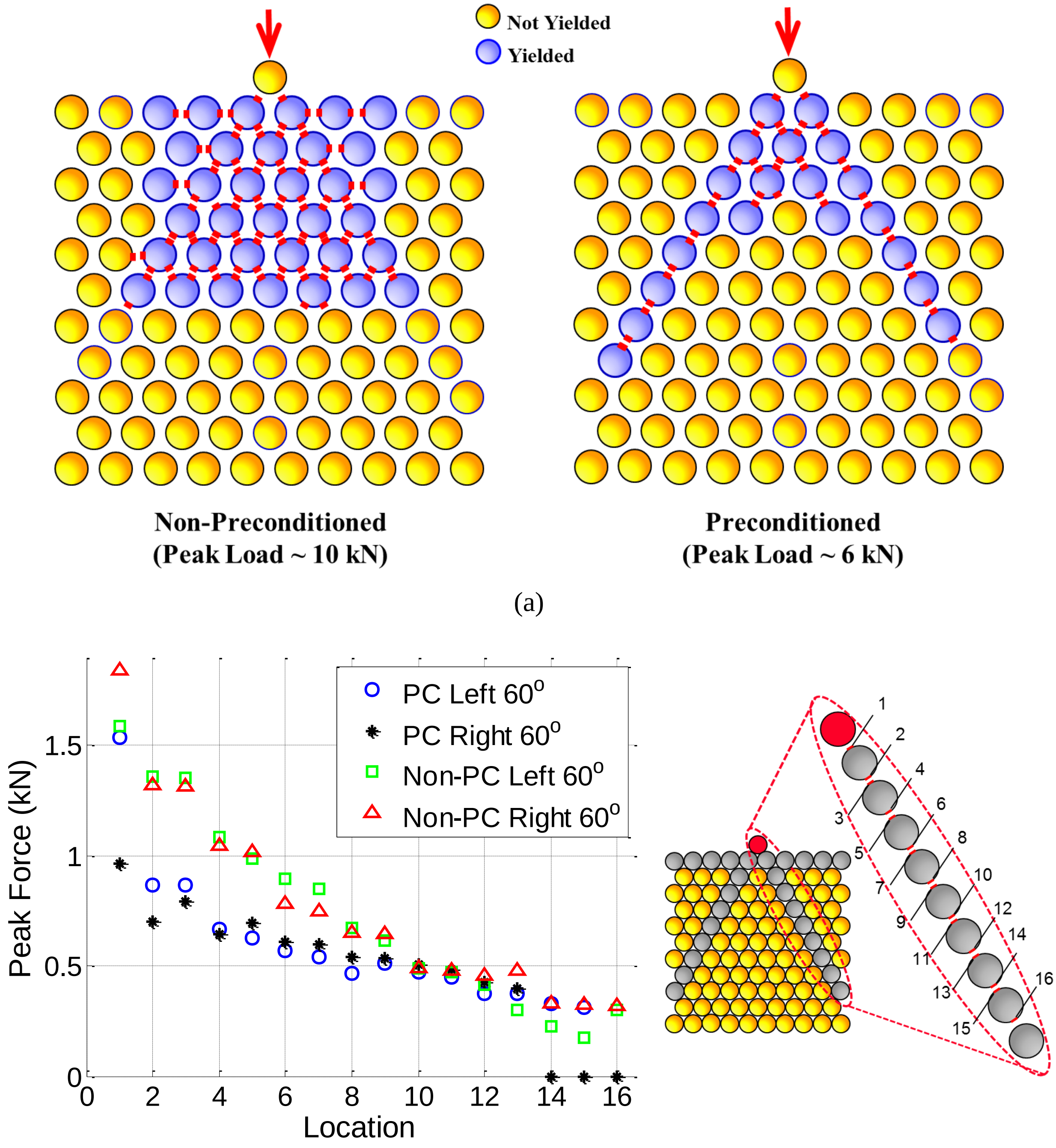

(a)

(b)

Figure 6.3: (a) Comparison of yield pattern between non-preconditioned system and horizontally preconditioned system (denoted “PC”). (b) Comparison of contact forces along the diagonal in the horizontally preconditioned and non-preconditioned systems.

6.1.2 Preconditioned interfacial packing

We created a hexagonal configuration of spheres in which one half side of the packing was not preconditioned and the other half side was preconditioned by introducing an “interfacial” bead that was not uniformly preconditioned. Non-uniform preconditioning, in which one side of the bead was preconditioned to a different level than its diametrically opposite counterpart was accomplished by using a custom-made bowl-shape holder that had a hole cut into the bottom. The bead was placed in the holder and then the bead-holder combination was compressed in a quasi-static load frame, as illustrated schematically in Figure 6.4. When compressed, the top contact was preconditioned to the desired load because it was subjected to a concentrated load, while the bottom of the sphere did not yield because load was distributed along the bowl-shaped support so that no yielding occurred along the bottom surface. Note that with other such configurations it would be possible to create beads with different types and amounts of preconditioning and thus address some issues with the geometric incompatibility of more complex designs that combine preconditioned and non-preconditioned beads. However this is beyond the scope of the present effort.

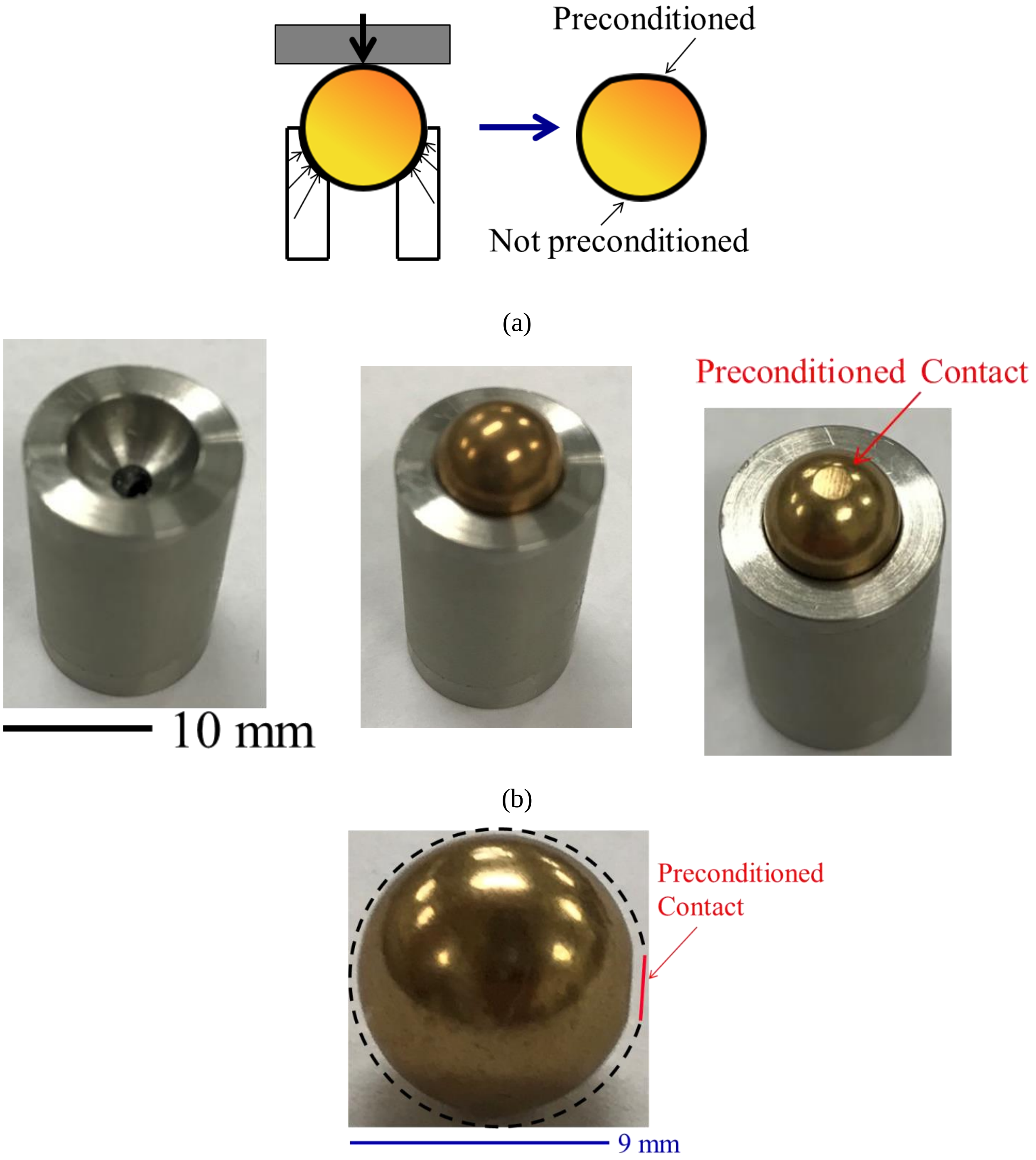

(a)

(b)

(c)

Figure 6.4: (a) Schematic of the process of non-uniformly preconditioning a bead. (b) Photographs of the empty bead holder, the holder with a bead, and the end result where the top contact has been preconditioned. (c) Profile image of the non-uniformly preconditioned bead. The dashed contour emphasizes that the bead remains round, except at the solid line, where the preconditioned contact is located.

Figure 6.5a shows a photograph of the interfacial configuration where one half of the packing contains 9 kN-preconditioned spheres (left side) and the other half contains non-preconditioned spheres (right side). The brass bead packing was surrounded by stainless steel spheres to better compare with a boundary condition to be used in a future numerical simulation, and their presence did not interfere with the experiment. Figure 6.5b shows a schematic of the packing and the purple dashed box indicates where the interfacial beads – the transition between horizontally preconditioned and non-preconditioned – were in each row. The preconditioned beads have a thicker outline than the non-preconditioned beads in Figure 6.5a. Note that without the interfacial bead, the hexagonal packing would become distorted since each row of 9 beads would be too short or too long to fit snugly with the rows of 10 beads, depending on if a uniformly preconditioned or non-preconditioned bead was placed at the central location (5th bead). Two instrumented beads were located at opposite sides of the top row (red and blue circles) and two more instrumented beads were located at the end of the diagonal chains that were in contact with the loading bead (green and black circles). The piezoelectric disk orientation is indicated by the solid black or white line.

Figure 6.5c shows the force histories measured at each sensor bead for a loading of 35 kN, where the color of the signal in the plot corresponds to the color of the bead in Figure 6.5b and the "(PC)" in the legend indicates that the sensor was on the preconditioned side of the packing. In this figure and subsequent figures in this Chapter, the signals have been truncated shortly after the completion of the primary pulse for clarity of presentation. Also, row identifiers such as "top" and "bottom" indicate relative positions to the loading bead since the actual packing was situated in a plane parallel to the ground. From Figure 6.5c, it is apparent that a higher amplitude wave arrived faster at the end of the preconditioned half of the top row than the non-preconditioned half (red vs. blue curves respectively). The non-preconditioned half of the top row dissipated energy at each contact since the yield strength of the brass beads was exceeded, whereas the preconditioned contacts allowed the wave to pass through elastically as a solitary wave if the wave amplitude was below the preconditioning level (9 kN). The two force histories at the end of the diagonal chains (green and black curves in Figure 6.5c) were relatively similar. The bottom left (green) experienced a slightly lower amplitude and slower wave speed, perhaps indicating that more energy was transferred to the preconditioned chains from the left diagonal than transferred to the non-preconditioned chains from the right diagonal.

Note that it was not necessary that one half of the interface be non-preconditioned – it could have been preconditioned to any level, say 5 kN, so long as the interfacial bead was appropriately preconditioned on both sides. In this way, you could further modify the wave speed and force amplitudes in both halves of the packing as desired based on preconditioning level. The 9 kN-no preconditioned interface illustrated here was chosen simply to provide a larger contrast in sensor readings between the two halves.

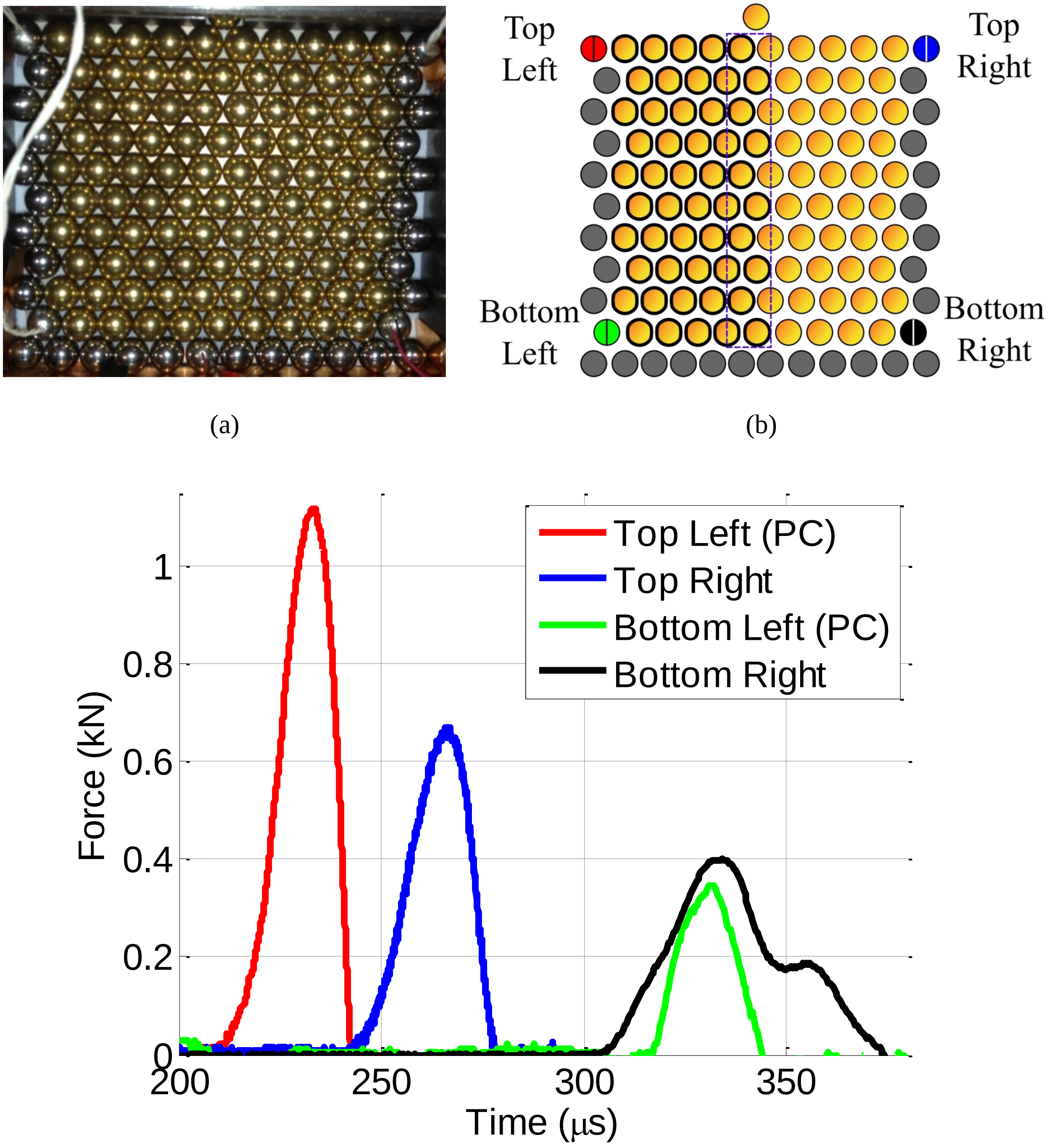

(a) (b)

(c)

Figure 6.5: Interfacial setup with horizontally preconditioned beads on one half and non-preconditioned beads on the other half. (a) Photograph of the experimental setup. (b) Schematic of the setup showing the locations of the interface (purple dashed box) and the instrumented beads (colored circles with solid line indicating piezoelectric disk orientation). (c) Force signals at each instrumented bead.

6.1.3 Preconditioned interfacial packing with improved load frame

After the experiments described above (and those conducted in Chapter 4), a few improvements were made to the steel load frame. First, a tungsten carbide adapter bar was installed that was impedance matched to the incident bar, allowing for a more accurate measurement of the load input into the system. The calculation of the input force remained the same as the method detailed in Section 2.2 and two typical strain gage signals (converted from voltage to force) are shown in Figure 6.6a-b for the non-preconditioned hexagonal array and the interface array respectively, and the calculated input forces are shown in the insets. Second, longer walls were manufactured which enabled a larger packing consisting of 16 rows in which the first row (the row closest to impact) contained 16 beads and subsequent rows alternated between 15 and 16 beads with a loading bead placed symmetrically in contact with the 8th and 9th beads of the first row, shown in the photograph in Figure 6.7a. The reasons for the larger packing are identical to those given for the larger packing in Chapter 5, i.e., allows the waves to more fully develop and also reduces any signal disturbances that may arise from multiple hits from the Hopkinson bar.

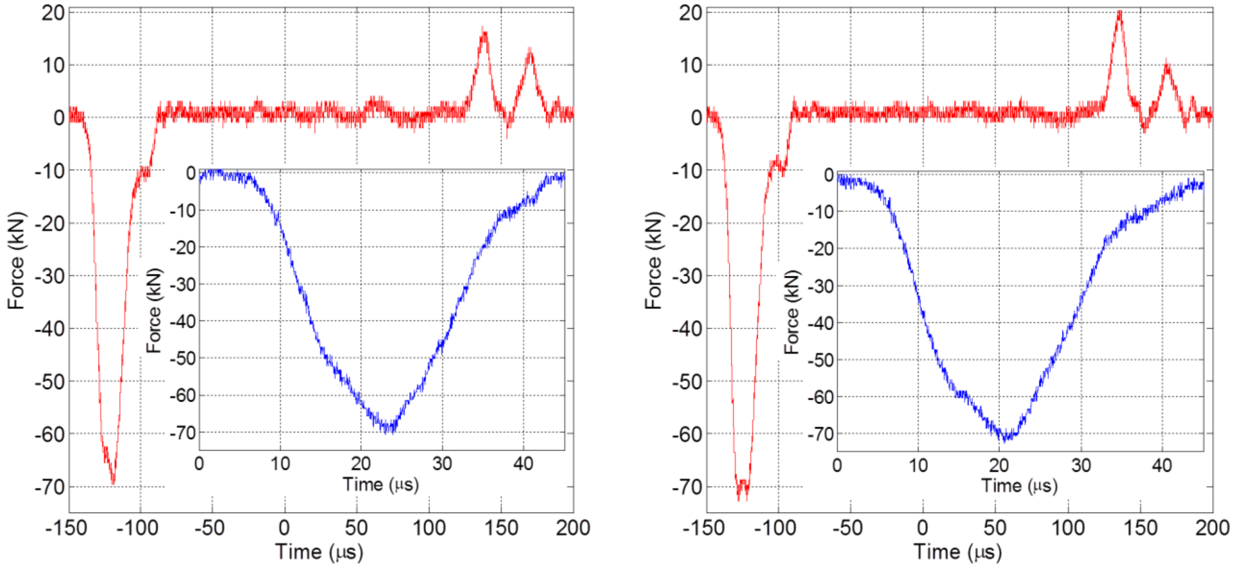

(a) (b)

Figure 6.6: Typical strain gage signals converted to force (red) and calculated input profiles (blue, inset) from the updated experimental setup. (a) Non-preconditioned hexagonal array. (b) Interface array.

The hexagonal packing (no preconditioning) photographed in Figure 6.7a was impacted with the input load shown in Figure 6.6a. The force was recorded at the five locations indicated in Figure 6.7b and is plotted in Figure 6.7c. Figure 6.7c provides a baseline for the symmetry expected in these experiments and shows that good symmetry was achieved between the two beads in the top row (red and blue beads) in terms of arrival time and peak force. Additionally, the bottom left (green) and bottom right (black) beads had similar peak forces. The bottom left sensor had been rotated ~60° counterclockwise (CCW) and the bottom right sensor ~60° clockwise (CW) to increase the signal at those sensors from the wave that travelled along the diagonals. The angle was verified by taking a close-up photograph of the sensor and comparing a line that runs parallel to the impact direction with a line that runs parallel to the seam between the two hemisphere halves using the program ImageJ, as shown in Figure 6.8.

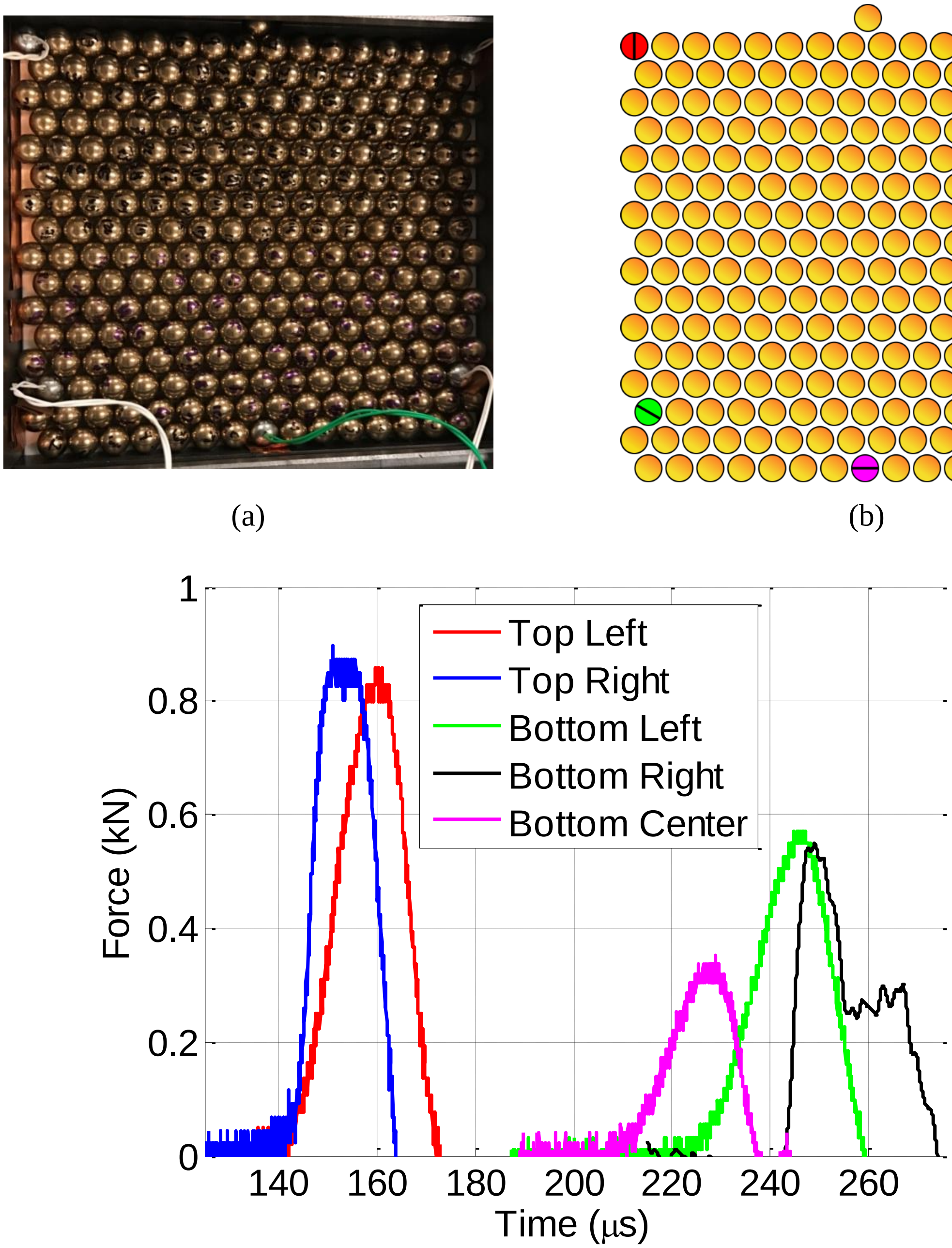

(a) (b)

(c)

Figure 6.7: (a) Photograph of larger bead packing. (b) Schematic of packing with sensor locations and orientations. The bottom left sensor has been rotated 60° counterclockwise and the bottom right sensor 60° clockwise. (c) Plot of forces at each instrumented bead location.

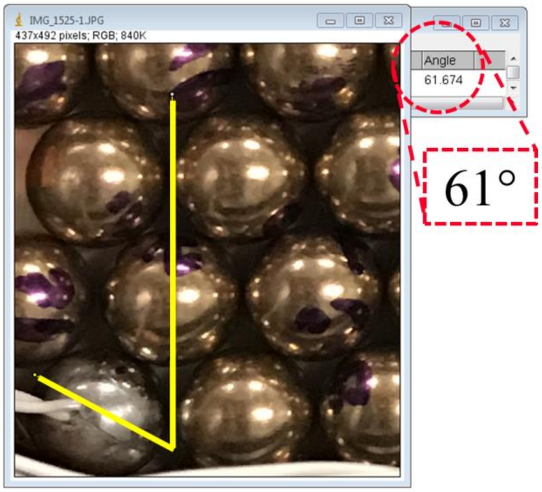

Figure 6.8: Determination of off-axis angle. An angle measurement is taken from a photograph of the sensor with the program ImageJ.

Figure 6.9a shows a schematic of an interfacial setup in this larger packing, where the left side of the packing was horizontally preconditioned at 9 kN and the right side was not preconditioned. As before, a non-uniformly preconditioned bead transitioned each row between the two preconditioning levels (9 kN and 0 kN) and they were located within the purple dashed box in Figure 6.9a. This interfacial packing was impacted with the input load in Figure 6.6b and the yield map of the interfacial setup is presented in Figure 6.9b in which blue circles indicate beads that yielded and the red squares denote the specific yielded contacts, as determined by optical microscopy. On the preconditioned side, only beads in the diagonal chain in contact with the loading bead and an adjacent diagonal chain yielded. Beyond four layers, the yielded contacts were aligned with a line that passed through all of the diagonal beads signifying that the elasto-plastic wave propagation occurred along the diagonal direction only and did not penetrate toward the center of the packing. On the non-preconditioned side, the elasto-plastic wave was more widely dispersed as evidenced by the quantity and location of yielded beads and contacts. The yield map in Figure 6.9b is a hybrid of the two yield maps in Figure 6.3a since the interfacial packing captured the yield characteristics of both the horizontally preconditioned packing and the non-preconditioned packing.

Figure 6.9c plots the resulting force at each instrumented bead, where the color of the signal on the plot corresponds with the color of the bead in Figure 6.9a. Again, the bottom left sensor was rotated ~60° counterclockwise (CCW) and the bottom right sensor ~60° clockwise (CW). Once more, the most apparent result of the interface occurred in the top row where the preconditioned side of the row received a faster, higher-amplitude wave than the non-preconditioned side. The bottom right sensor (black) recorded a higher force than the bottom left sensor (green), again indicating that the preconditioned rows laterally divert energy away from the bottom row. Figure 6.6 shows that the input loads were similar between the non-preconditioned hexagonal packing above (Figure 6.7) and the interfacial packing. We can thus make a comparison between the forces that reach the bottom center of the packing (magenta signals in Figure 6.7c and Figure 6.9b) and note that less force reached the sensor in the interfacial case (210 N) than the non-preconditioned case (320 N), again pointing to the fact that the preconditioned contacts laterally deflected energy. The interfacial packing demonstrated the ability to tailor the wave propagation using preconditioned contacts.

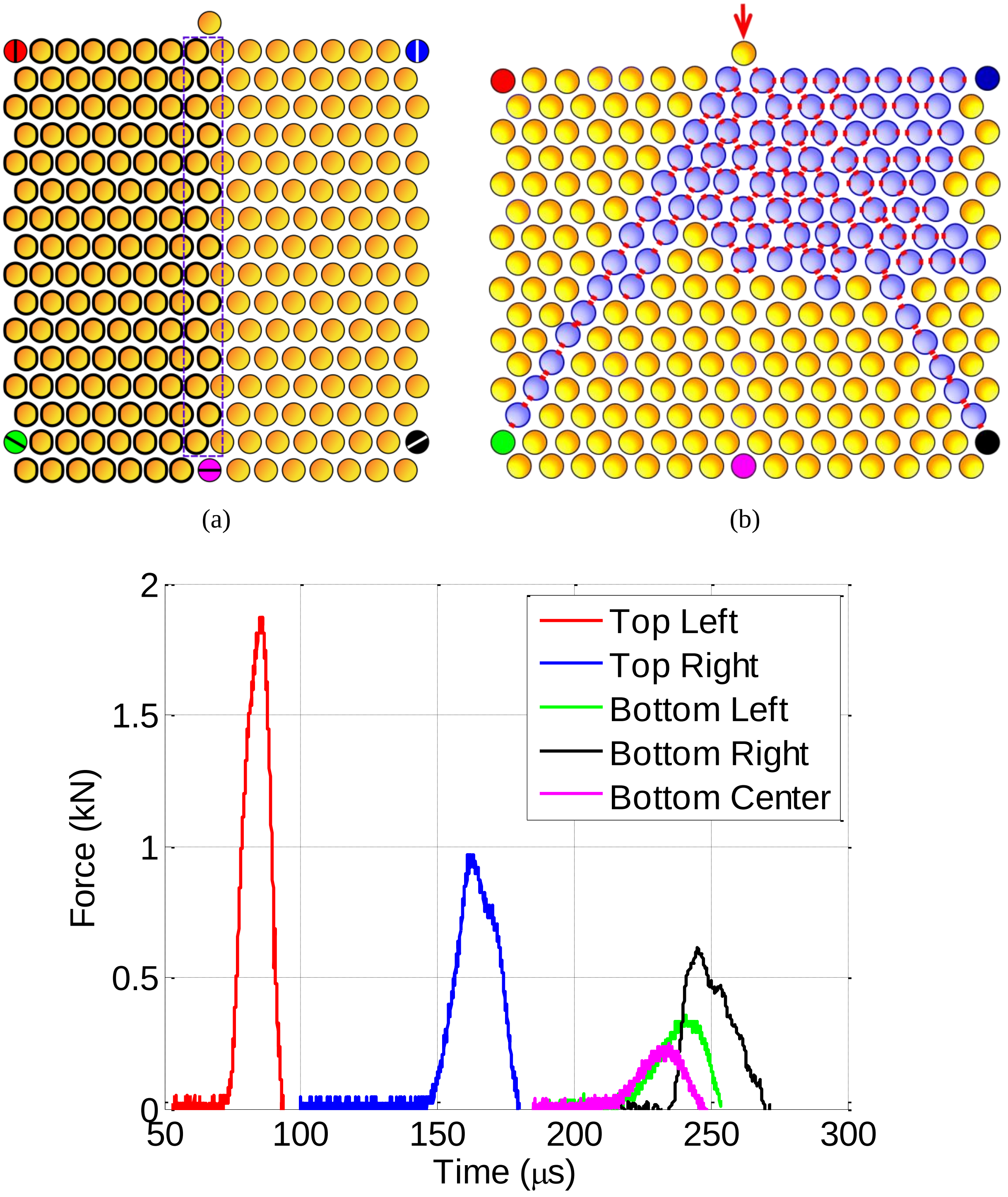

(a) (b)

(c)

Figure 6.9: Horizontally preconditioned with interface. (a) Schematic of setup with interface enclosed by purple dashed box and sensor locations and piezoelectric disk orientations. The preconditioned beads have a bold outline. (b) Yield map. (c) Force histories from instrumented beads.

6.2 Vertical Preconditioning

Next we investigated wave tailoring in a vertically preconditioned hexagonal packing in which the preconditioned contacts were arranged such that if a line was passing through them, that line would be parallel to the loading direction. Alternatively, the vertically preconditioned system can be thought of as the horizontally preconditioned system rotated 90°, as seen in Figure 6.10a. The corresponding force signals for this configuration (loaded to 70 kN) are shown in Figure 6.10b. Of the sensor locations along the bottom row (Sensor 1, 2, and 3), Sensor 1 recorded the highest load, as was expected since Sensor 1 is located directly opposite the impact and all of the contacts between the impact and Sensor 1 were preconditioned. In fact, Sensor 1 received an elastic solitary wave and the blue curve was not truncated in Figure 6.10b. The next wave to arrive was at Sensor 2, which was two rows away from Sensor 1, and the last wave to arrive at the bottom row was at Sensor 3 which was even further away from Sensor 1. The relative arrival times and force amplitudes were reasonable considering each sensor's location.

Sensor 4 was located along the sides of the packing and rotated 30° CW to again maximize the signal from a wave travelling along the diagonal. The first wave detected in the entire packing was a (relatively) low amplitude wave at Sensor 4 which was reasonable since the sensor is located at the end of a diagonal chain directly in contact with the loading bead with only six beads between the loading bead and Sensor 4. In contrast, the next wave to arrive, at Sensor 1, had 14 beads separating it from the loading bead.

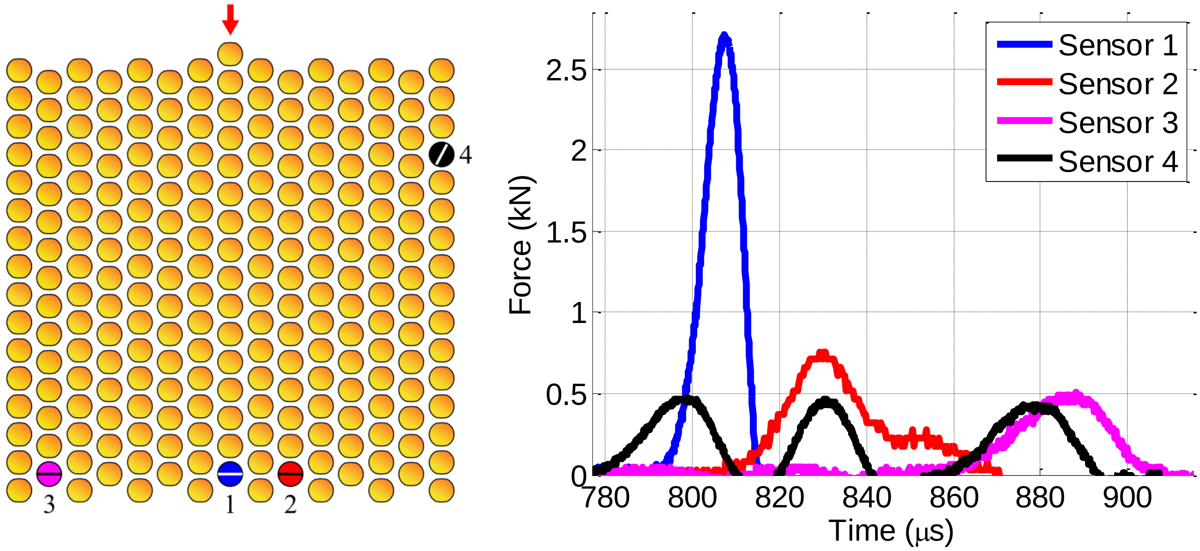

(a) (b)

Figure 6.10: Point loading of vertically preconditioned system. (a) Setup and sensor locations. (b) Force signals.

Next, we introduced an interface in the system such that the top half of the system was vertically preconditioned and the bottom half consisted of non-preconditioned beads, as shown in Figure 6.11a. This configuration now contained an interface perpendicular to the loading direction, unlike the configuration studied in Section 6.1 where the interface was parallel to the loading direction. The interfacial system was loaded at nearly the same input force as the vertically preconditioned system. Figure 6.11b plots the forces at the Sensor 1 location (black) and Sensor 2 location (cyan) and compares them with the signals from the same locations in the totally preconditioned system (replicated from Figure 6.10b). The presence of non-preconditioned spheres lowered the amplitude of the force that reaches Sensor 1 and consequently delayed the arrival time. The amplitudes of the signals at the Sensor 2 location were similar between the two configurations, another unexpected result as the introduction of non-preconditioned contacts should reduce the force amplitude at the locations along the bottom row. However, the presence of additional non-preconditioned contacts delayed the arrival of the wave when compared with the totally preconditioned case.

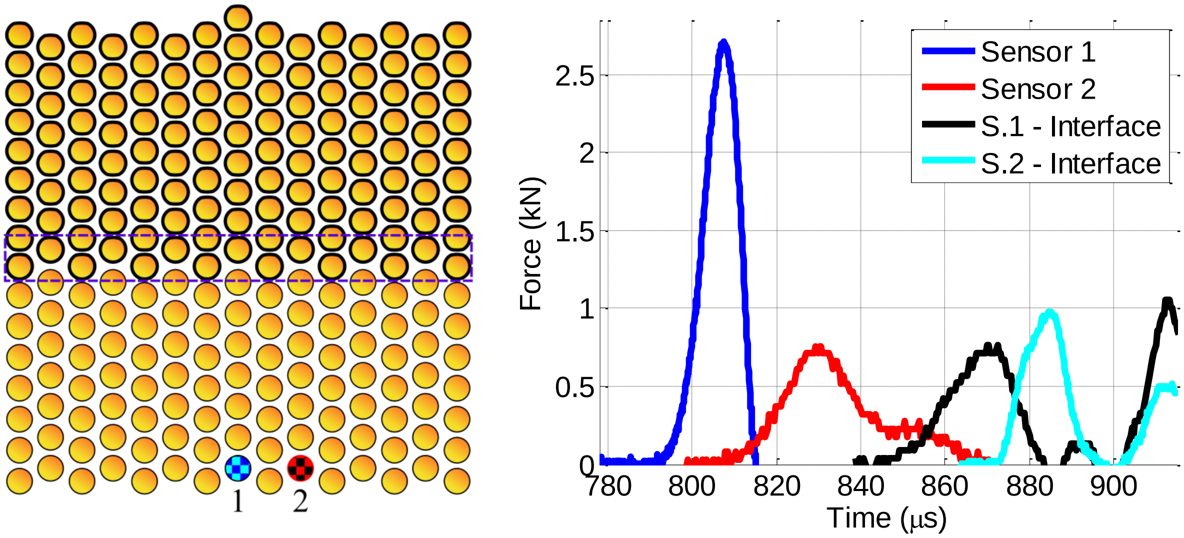

(a) (b)

Figure 6.11: (a) Vertically preconditioned system with interface (enclosed in purple dashed box) and sensor locations. (b) Comparison of force signals at Sensor 1 and 2 locations for between the total vertically preconditioned system and the vertically preconditioned with interface system.

Whereas the horizontally preconditioned system was thought to laterally deflect waves away from the "bottom" of the packing relative to the non-preconditioned system, the vertically preconditioned enabled higher-amplitude waves to pass through to the bottom. The amplitude of the waves that propagated across the packing could be controlled by changing the preconditioning levels on either side of the interface or by changing the location of the interface itself. In Figure 6.11, the interface is centrally located. Higher-amplitude waves could propagate across the packing by moving the interface closer to the bottom of the packing and, conversely, the wave amplitude that reaches the bottom of the packing could be reduced by moving the interface closer to the impact site.

6.3 Line Loading in Horizontally and Vertically Preconditioned Systems

All of the configurations previously studied were point-loaded in that the load transmitted by the adapter bar was applied onto one bead, the loading bead. In many cases the applied loading may be spread over an area (i.e., several granules) instead of acting on just one. Here we modify the experimental arrangement to introduce a line loading which will simultaneously load several beads in the granular assembly. Line loading was accomplished by placing a custom-made aluminum triangular plate, described in Chapter 2, between the incident bar and the granular system. The triangular piece allowed for all of the beads in the first row (the row closest to impact) of the horizontally preconditioned system to be about equally loaded, as discussed in Chapter 2.

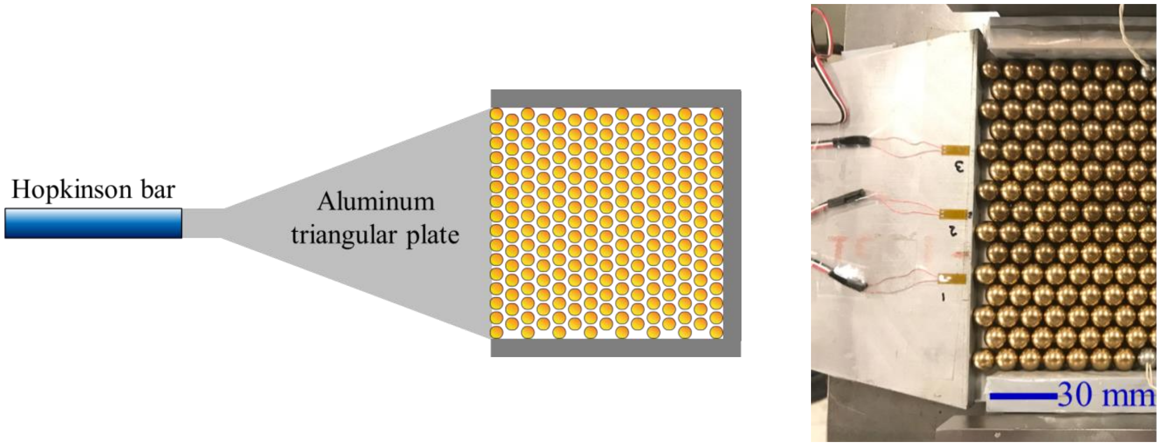

(a) (b)

Figure 6.12: Schematic (a) and image (b) of setup for line loading the 2D ordered granular media.

Figure 6.13a schematically shows a horizontally preconditioned system subject to planar loading and the sensor locations within the packing. Figure 6.13b displays the yield map and Figure 6.13c while plots the force results, where the sensor numbers correspond to the numbers in Figure 6.13a. The yield map indicates a large amount of yielding within the first three rows. Since the triangular plate loaded the entire top row, several more contacts were compressed in the entire top region of the packing as compared with the point-loaded case. The contacts rapidly yielded and dissipated the energy such that the elasto-plastic wave was mostly eliminated past the third row. The readings from Sensors 1, 2 (rotated 60° CCW), and 4 were almost negligible and indicated only an elastic wave reaching those locations, which supported the conclusion from the yield map that no plasticity occurred beyond the fourth row. Only Sensor 3 records a significant force, which is reasonable since it was the closest sensor to the impact and located three beads away from a yielded contact. Thus Sensor 3 could be detecting a load that yielded the intervening contacts but below the contact surface (thus not detectable by the optical microscope), where yield initiates according to Hertz contact theory and von Mises criterion [13]. Another experiment of non-preconditioned beads would be necessary to determine if the load at Sensor 3 was in fact due to the horizontally preconditioned contacts. However, yielding would still be expected at some contact between the fourth row (the farthest row from impact with yielded contacts) and the seventh row (the row containing Sensor 3) for the load to then be transmitted via preconditioned contact to Sensor 3.

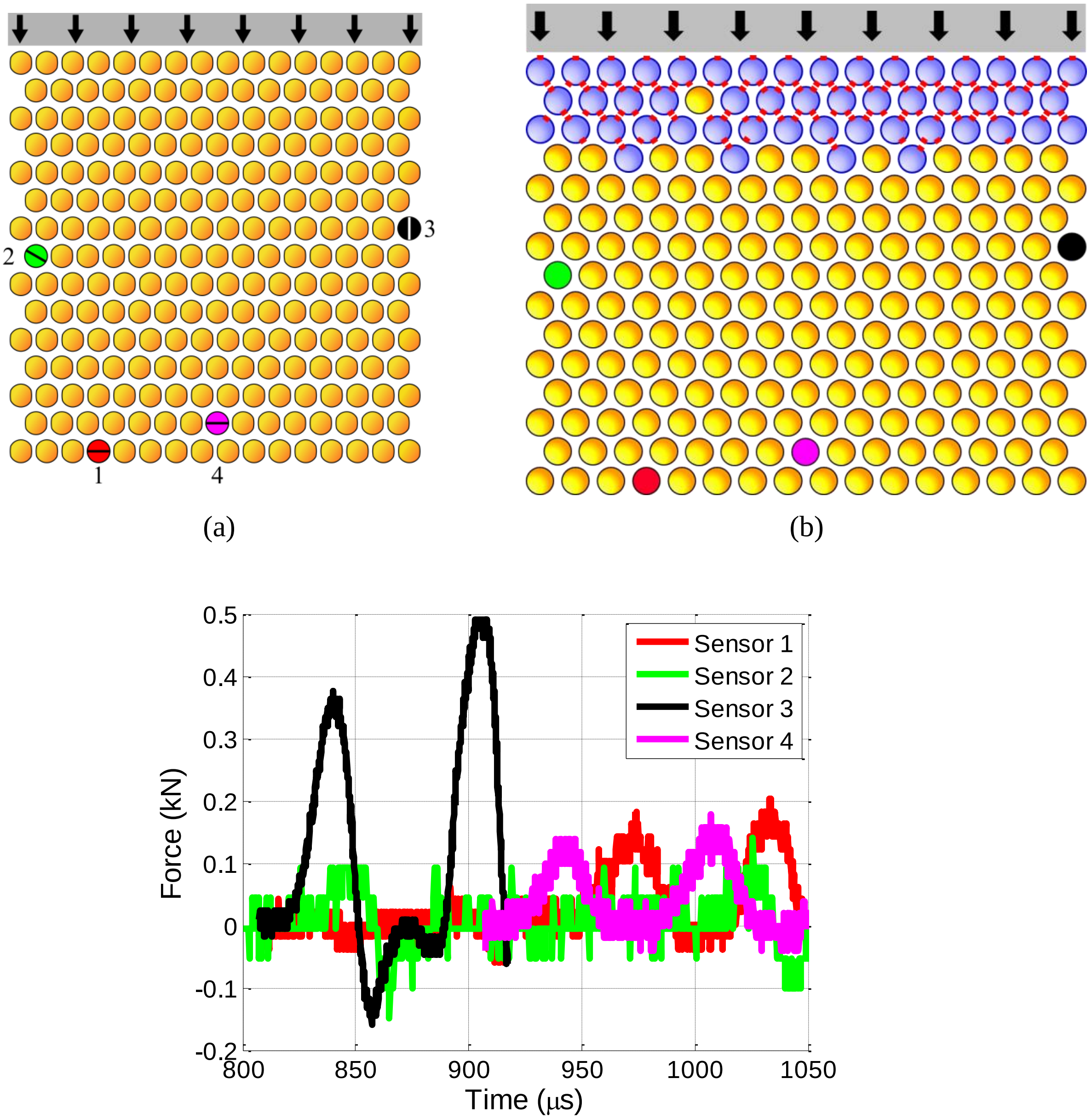

Figure 6.13: (a) Schematic of horizontally preconditioned array subjected to line loading. Enumerated circles with solid lines through them indicate locations of the piezoelectric sensors and the orientation of the sensor disk. (b) Yield map where each blue bead has been yielded and the yielded contact is indicated by a small red rectangle. (c) Force signals from the instrumented beads, where the color of the trace and sensor number corresponds to the color and number of the bead location in (a).

Next, we line loaded the vertically preconditioned system in which, due to the system's geometry, only every other sphere in the first row was in contact with the loading equipment. A schematic of the system with sensor locations is shown in Figure 6.14a. The accompanying yield map is in Figure 6.14b and the signals from the sensors are plotted in Figure 6.14c. Fewer contacts yielded in the vertically preconditioned case than the horizontally preconditioned case due to the load primarily travelling along the preconditioned contacts which were in the vertical direction here. Indeed, Sensors 1-3 recorded large amplitude elastic wave trains whereas the horizontal packing only experienced low-amplitude elastic waves at similar locations. Sensors 2 and 3 should have ideally recorded similar magnitudes if the system had been symmetrically loaded, although the variability in bead size discussed in Chapter 4 may have also contributed to the signal discrepancy. Sensor 4 showed no load and was located along a chain that was not in contact with the impacting plate. Thus it appears that the high amplitude waves travelled primarily along the preconditioned contacts and transferred little energy via the non-preconditioned contacts.

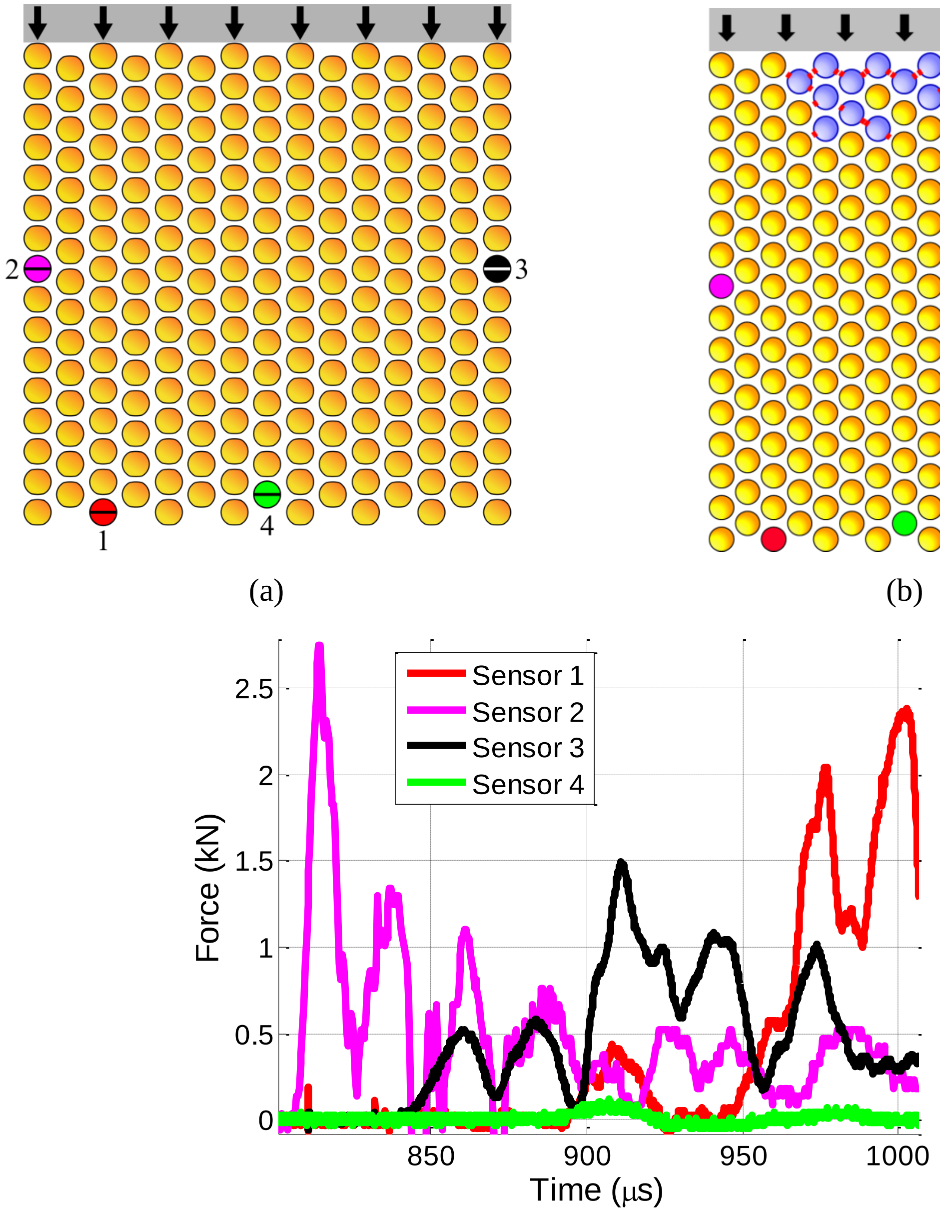

(a)

(b)

(c)

Figure 6.14: (a) Schematic of the array showing the preconditioned contacts aligned vertically (parallel with the loading direction) in the line loading setup. Enumerated circles with solid lines through them indicate locations of the piezoelectric sensors and the orientation of the sensor disk. (b) Yield map where each blue bead has been yielded and the yielded contact is indicated by a small red rectangle. (c) Force signals from the instrumented beads, where the color of the trace and sensor number corresponds to the color and number of the bead location in (a).

Chapter 6 investigated preconditioned contacts as a means of wave tailoring. The interfacial setups have shown the clearest evidence of the effect of preconditioned contacts on wave propagation and the potential for wave tailoring. Additionally, the interfacial setups indicated we can control regions of plasticity in these materials. The wave behavior in an interfacial packing can be further altered by changing the location of the interface or by preconditioning both sides of the interface to different levels.

Whereas horizontal preconditioning seemed to laterally deflect the wave, vertical preconditioning enabled more load to reach the opposite side of a packing, relative to impact. In the event of line loading, the horizontally preconditioned system rapidly attenuated the elasto-plastic wave via dissipation at the non-preconditioned contacts. Conversely, for a line-loaded system, vertical preconditioning allowed the incoming wave to pass through and transferred plastic loads across far fewer contacts than the horizontally preconditioned system.

7. CONCLUSIONS AND FUTURE WORK

7.1 Conclusions

7.1.1 Designs in 1D chains

The work presented in this thesis focused on managing stress wave propagation in ordered granular materials consisting of ductile metallic granules, generally at amplitudes sufficient to induce extensive yielding. Two 1D arrangements were studied as acoustic equivalents to electro-optical systems. The first system managed elastic solitary waves and could be switched between allowing or hindering solitary wave propagation. The same system could also be considered a diode since it allows solitary wave propagation to pass in one direction and hinders it in the opposite direction. Side spheres, the parameter that tuned the wave propagation, are relatively simple to place along any 1D chain. As such, networks of granular chains could be constructed with each chain having different solitary wave properties by controlling the number of side spheres along a given branch.

The second arrangement served as a low-pass filter for high-amplitude waves by utilizing preconditioned contacts and plasticity. The low-pass filter is the first design that utilizes preconditioned beads and illustrates the potential to manage high amplitude waves. Such a design can take an arbitrarily high input load, and for a sufficiently long chain, reduce it to some desired load level.

7.1.2 Designs in 2D granular arrays

We also extended our study of elasto-plastic waves to 2D square and hexagonal systems. Basic studies of these systems (i.e., without attempting to tailor the wave propagation) revealed that the wave propagation patterns are similar to their purely elastic counterparts, although they exhibit significant differences in dissipation. The plastically loaded packings demonstrated an incredible ability to mitigate high-amplitude waves, frequently diminishing input loads from kilo-Newtons to a few hundred Newtons within a few contacts, as measured by instrumented beads along the boundary. However, significant scatter was observed in the experimental results of nominally identical tests, which was attributed, in part, to the inherent (i.e., manufacturer created) size tolerance of the beads. A simulation that incorporated the bead diameter tolerance corroborated the size variability as a source of scatter in the peak forces and wave arrival times in the 2D square configuration.

Granular materials offer the ability to tailor wave propagation, a task which cannot be achieved in traditional materials. We demonstrated the ability to laterally tailor elasto-plastic waves in a square packing by placing intruders at interstitial locations. The intruder placement was guided by a numerical optimization scheme, provided by our collaborators, that sought to achieve various objectives such as maximizing or minimizing momentum and force at certain regions within the packing. Similar trends were observed between the simulations and experiments, validating the ability to accurately model elasto-plastic propagation in the bead-cylinder system. An iterative scheme was proposed to improve the results of solutions that converged to local minima by prohibiting or mandating cylinders at certain locations, effectively changing the initial condition of the optimization procedure.

In addition to controlling plasticity in a system, as was accomplished with the cylindrical intruders, we could manage elastic high-amplitude waves in a system through preconditioned contacts, which was accomplished for the first time in this work. Various preconditioning setups demonstrated the concept of “directional plasticity” in which the location of yielded contacts could be altered relative to the packing with no preconditioning. We will term the ability of controlling the regions that experience plasticity by tailoring the propagation of high-amplitude waves. An interfacial system, containing un-yielded and preconditioned beads was tailored to exhibit faster wave speeds and higher amplitude wave propagation in certain regions, while promoting plastic dissipation in other regions, clearly illustrating the ability of preconditioned contacts to tailor wave propagation.

Intruders and preconditioned contacts can simultaneously be employed to tailor a system with desirable wave propagation characteristics. Indeed, the optimization scheme presented here has the capability of solving for optimal preconditioned contacts, such that a system with could be design with optimal load paths (via preconditioned contacts) and optimal dissipation paths (via interstitial intruders).

7.2 Future Work

The wave tailoring techniques employed in this work can be used to design several other 1D and 2D structures. For instance, a high amplitude acoustic lens could be created from several 1D chains where the tuning parameter is the preconditioning level. Additionally, the optimization scheme could solve for some combination of intruders, preconditioned contacts, and material properties of the beads to satisfy some complicated design goal, such as the ability to cloak an object, discussed in Chapter 1.

Of course, the ultimate goal of these designs is to create useful engineering materials, so it is necessary to extend this work into three-dimensions (3D). Some preliminary work regarding 3D structures has been conducted and will be presented here as examples of the types of tests that need to be more broadly conducted to investigate 3D structures. The beads tested are 5 mm diameter magnetic neodymium beads ($Nd_2Fe_{14}B$) and are capable of maintaining their structure without any additional support (e.g., a polymer matrix).

First, we investigated force transmission through two basic 3D structures – a simple cubic packing and a packing where each tetrad is rotated 90° relative to the layer below it, both shown in Figure 7.1 – using a split Hopkinson pressure bar (SHPB). Figure 7.2 shows that increasing the layers in a packing decreased the transmitted force. Note that a higher pressure (PSI) generally corresponded to a higher input force. The cubic pattern was seen to be more effective at transmitting force than the tetrad packing.

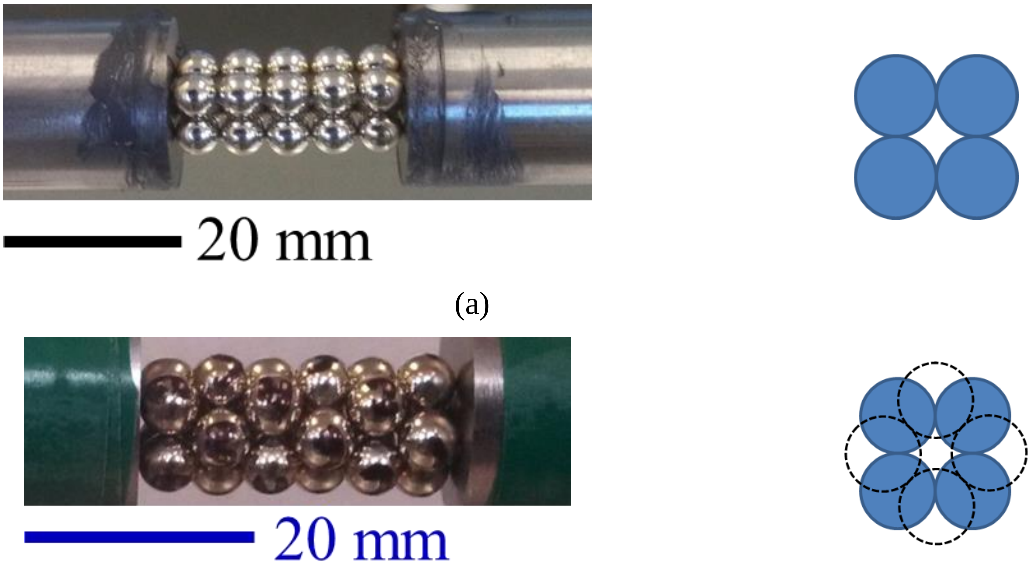

(a)

(b)

Figure 7.1: SHPB tests on (a) Arrangements on a cubic packing and (b) tetrad packing.

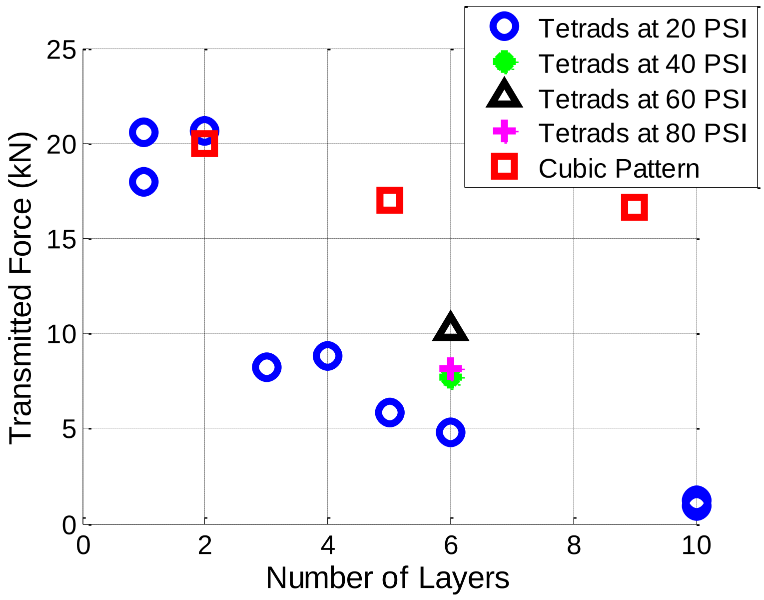

Figure 7.2: Transmitted force as a function of number of layers.

Next, 9x9 simple cubic packings of varying layers were tested in a plate-impact apparatus, a device capable of significantly higher input loads than the SHPB. Figure 7.3a shows the magnetic cubic packing, which was sufficiently attracted to the anvil that no additional support was required. Four packings of various layers were impacted by a flyer plate on the side of the packing that is opposite of the anvil. During the impact, the particle velocity was recorded at the rear of the anvil using either a velocity interferometer system of any reflector (VISAR) or photon Doppler velocimetry (PDV). Since the anvil remains elastic and uniaxial conditions apply, the particle velocity, u, is related to the normal stress in the anvil, σ, through the equation $\sigma = \rho c_l u$, where ρ and c_l are the density and the longitudinal wave speed of the anvil. It can be seen in Figure 7.3b as the quantity of layers increases, the particle velocity (and stress) in the anvil decrease.

Granular materials dissipate input energy at lower loads and at a much higher rate than comparable continuum materials [86]. The rate at which energy dissipates is predicted to plateau at higher input energies. Plate impact experiments could verify this trend since they provide a greater input energy than other impact devices such as a drop weight tower or SHPB. Lastly, the plate impact experiment could be adjusted by tilting the flyer plate and anvil and allowing for the study of shear waves in the granular packing.

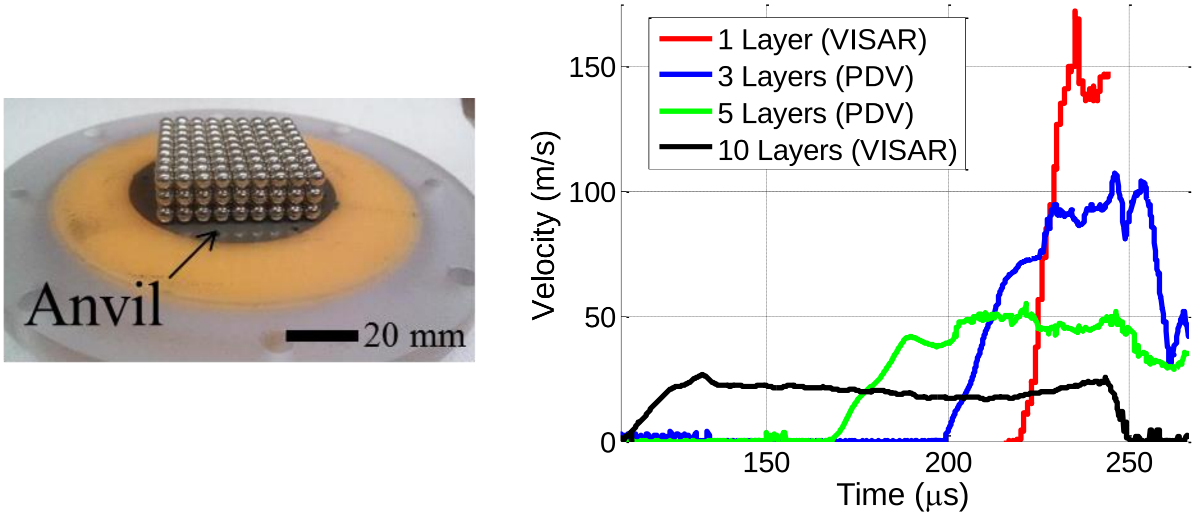

(a) (b)

Figure 7.3: (a) Simple cubic 9x9 packing on an anvil to be tested. (b) Velocity recorded at the rear of the anvil during impact.

These 3D tests will lead to a greater understanding of the dynamic elasto-plastic behavior of granular systems and aide in the development of technologies for stress wave mitigation and control.

REFERENCES

[1] Duran, J., 2000, *Sands, Powders, and Grains: An Introduction to the Physics of Granular Materials*, Springer Science & Business Media, New York.

[2] Jaeger, H. M., Nagel, S. R., and Behringer, R. P., 1996, "Granular Solids, Liquids, and Gases," Rev. Mod. Phys., **68**(4), pp. 1259–1273.

[3] Liu, A. J., and Nagel, S. R., 1998, "Nonlinear Dynamics: Jamming Is Not Just Cool Any More," Nature, **396**(6706), pp. 21–22.

[4] Trappe, V., Prasad, V., Cipelletti, L., Segre, P. N., and Weitz, D. A., 2001, "Jamming Phase Diagram for Attractive Particles," Nature, **411**(6839), pp. 772–775.

[5] Saadatfar, M., Sheppard, A. P., Senden, T. J., and Kabla, A. J., 2012, "Mapping Forces in a 3D Elastic Assembly of Grains," J. Mech. Phys. Solids, **60**(1), pp. 55–66.

[6] Beladjine, D., Ammi, M., Oger, L., and Valance, A., 2007, "Collision Process between an Incident Bead and a Three-Dimensional Granular Packing," Phys. Rev. E, **75**(6).

[7] Ammi, M., Oger, L., Beladjine, D., and Valance, A., 2009, "Three-Dimensional Analysis of the Collision Process of a Bead on a Granular Packing," Phys. Rev. E, **79**(2).

[8] Bless, S., Cooper, W., Watanabe, K., and Peden, R., 2012, "Deceleration of Projectiles in Sand," pp. 45–47.

[9] Allen, W. A., Mayfield, E. B., and Morrison, H. L., 1957, "Dynamics of a Projectile Penetrating Sand," J. Appl. Phys., **28**(3), pp. 370–376.

[10] Coste, C., Falcon, E., and Fauve, S., 1997, "Solitary Waves in a Chain of Beads under Hertz Contact," Phys. Rev. E, **56**(5), p. 6104.

[11] Jia, X., Caroli, C., and Velicky, B., 1999, "Ultrasound Propagation in Externally Stressed Granular Media," Phys. Rev. Lett., **82**(9), p. 1863.

[12] Tournat, V., and Gusev, V. E., 2010, "Acoustics of Unconsolidated 'Model' Granular Media: An Overview of Recent Results and Several Open Problems," Acta Acust. United Acust., **96**(2), pp. 208–224.

[13] Johnson, K. L., 1985, *Contact Mechanics*, Cambridge University Press, Cambridge, U.K.

[14] Meyers, M. A., 1994, *Dynamic Behavior of Materials*, John Wiley & Sons, Inc.

[15] Nesterenko, V. F., 2001, "Nonlinear Impulses in Particulate Materials," *Dynamics of Heterogeneous Materials*, Springer Science & Business Media, New York, pp. 1–126.

[16] Nesterenko, V. F., 1983, "Propagation of Nonlinear Compression Pulses in Granular Media," J. Appl. Mech. Tech. Phys., **24**(5), pp. 733–743.

[17] Lazaridi, A. N., and Nesterenko, V. F., 1985, "Observation of a New Type of Solitary Waves in a One-Dimensional Granular Medium," J. Appl. Mech. Tech. Phys., **26**(3), pp. 405–408.

[18] Daraio, C., Nesterenko, V. F., Herbold, E. B., and Jin, S., 2005, "Strongly Nonlinear Waves in a Chain of Teflon Beads," Phys. Rev. E, **72**(1).

[19] Lide, D. R., ed., 2004, *CRC Handbook of Chemistry and Physics*, CRC Press LLC, Boca Raton, FL.

[20] Sen, S., Manciu, M., Sinkovits, R. S., and Hurd, A. J., 2001, "Nonlinear Acoustics in Granular Assemblies," Granul. Matter, **3**(1), pp. 33–39.

[21] Sen, S., Hong, J., Bang, J., Avalos, E., and Doney, R., 2008, "Solitary Waves in the Granular Chain," Phys. Rep., **462**(2), pp. 21–66.

[22] Kevrekidis, P. G., 2011, "Non-Linear Waves in Lattices: Past, Present, Future," IMA J. Appl. Math., **76**(3), pp. 389–423.

[23] Daraio, C., Nesterenko, V. F., Herbold, E. B., and Jin, S., 2006, “Tunability of Solitary Wave Properties in One-Dimensional Strongly Nonlinear Phononic Crystals,” Phys. Rev. E, **73**(2), p. 026610.

[24] Porter, M. A., Daraio, C., Herbold, E. B., Szelengowicz, I., and Kevrekidis, P. G., 2008, “Highly Nonlinear Solitary Waves in Periodic Dimer Granular Chains,” Phys. Rev. E, **77**(1).

[25] Porter, M. A., Daraio, C., Szelengowicz, I., Herbold, E. B., and Kevrekidis, P. G., 2009, “Highly Nonlinear Solitary Waves in Heterogeneous Periodic Granular Media,” Phys. Nonlinear Phenom., **238**(6), pp. 666–676.

[26] Herbold, E. B., Kim, J., Nesterenko, V. F., Wang, S. Y., and Daraio, C., 2009, “Pulse Propagation in a Linear and Nonlinear Diatomic Periodic Chain: Effects of Acoustic Frequency Band-Gap,” Acta Mech., **205**(1–4), pp. 85–103.

[27] Boechler, N., Daraio, C., Narisetti, R. K., Ruzzene, M., and Leamy, M. J., 2010, “Analytical and Experimental Analysis of Bandgaps in Nonlinear One Dimensional Periodic Structures,” *IUTAM Symposium on Recent Advances of Acoustic Waves in Solids*, T.-T. Wu, and C.-C. Ma, eds., Springer Netherlands, Dordrecht, pp. 209–219.

[28] Boechler, N., Yang, J., Theocharis, G., Kevrekidis, P. G., and Daraio, C., 2011, “Tunable Vibrational Band Gaps in One-Dimensional Diatomic Granular Crystals with Three-Particle Unit Cells,” J. Appl. Phys., **109**(7), p. 074906.

[29] Boechler, N., Theocharis, G., Job, S., Kevrekidis, P. G., Porter, M. A., and Daraio, C., 2010, “Discrete Breathers in One-Dimensional Diatomic Granular Crystals,” Phys. Rev. Lett., **104**(24).

[30] Theocharis, G., Boechler, N., Kevrekidis, P. G., Job, S., Porter, M. A., and Daraio, C., 2010, “Intrinsic Energy Localization through Discrete Gap Breathers in One-Dimensional Diatomic Granular Crystals,” Phys. Rev. E, **82**(5).

[31] Jayaprakash, K. R., Starosvetsky, Y., and Vakakis, A. F., 2011, “New Family of Solitary Waves in Granular Dimer Chains with No Precompression,” Phys. Rev. E, **83**(3).

[32] Potekin, R., Jayaprakash, K. R., McFarland, D. M., Remick, K., Bergman, L. A., and Vakakis, A. F., 2013, “Experimental Study of Strongly Nonlinear Resonances and Anti-Resonances in Granular Dimer Chains,” Exp. Mech., **53**(5), pp. 861–870.

[33] Nakagawa, M., Agui, J. H., Wu, D. T., and Extramiana, D. V., 2003, “Impulse Dispersion in a Tapered Granular Chain,” Granul. Matter, **4**(4), pp. 167–174.

[34] Melo, F., Job, S., Santibanez, F., and Tapia, F., 2006, “Experimental Evidence of Shock Mitigation in a Hertzian Tapered Chain,” Phys. Rev. E, **73**(4).

[35] Rosas, A., and Lindenberg, K., 2004, “Pulse Velocity in a Granular Chain,” Phys. Rev. E, **69**(3).

[36] Harbola, U., Rosas, A., Esposito, M., and Lindenberg, K., 2009, “Pulse Propagation in Tapered Granular Chains: An Analytic Study,” Phys. Rev. E, **80**(3), p. 031303.

[37] Machado, L. P., Rosas, A., and Lindenberg, K., 2013, “Momentum and Energy Propagation in Tapered Granular Chains,” Granul. Matter, **15**(6), pp. 735–746.

[38] Doney, R., and Sen, S., 2006, “Decorated, Tapered, and Highly Nonlinear Granular Chain,” Phys. Rev. Lett., **97**(15).

[39] Daraio, C., Ngo, D., Nesterenko, V. F., and Fraternali, F., 2010, “Highly Nonlinear Pulse Splitting and Recombination in a Two-Dimensional Granular Network,” Phys. Rev. E, **82**(3), p. 036603.

[40] Ngo, D., Fraternali, F., and Daraio, C., 2010, "Angular Dependence of Highly Nonlinear Pulse Splitting in a Two Dimensional Granular Network," *Proceedings of the ASME 2010 International Mechanical Engineering Congress & Exposition, IMECE2010-39699, Vancouver Canada*.

[41] Ngo, D., Fraternali, F., and Daraio, C., 2012, "Highly Nonlinear Solitary Wave Propagation in Y-Shaped Granular Crystals with Variable Branch Angles," Phys. Rev. E, **85**(3), p. 036602.

[42] Leonard, A., Ponson, L., and Daraio, C., 2014, "Wave Mitigation in Ordered Networks of Granular Chains," J. Mech. Phys. Solids, **73**, pp. 103–117.

[43] Daraio, C., Nesterenko, V. F., Herbold, E. B., and Jin, S., 2006, "Energy Trapping and Shock Disintegration in a Composite Granular Medium," Phys. Rev. Lett., **96**(5), p. 058002.

[44] Leng, D., Wang, X., Liu, G., and Sun, L., 2016, "Impulse Absorption by Horizontal Magnetic Granular Chain," AIP Adv., **6**(2), p. 025321.

[45] Fraternali, F., Porter, M. A., and Daraio, C., 2009, "Optimal Design of Composite Granular Protectors," Mech. Adv. Mater. Struct., **17**(1), pp. 1–19.

[46] Bek, M., Oseli, A., Saprunov, I., Zhumagulov, B. T., Mian, S. M., Gusev, B. V., Žarnić, R., von Bernstorff, B., Holeček, N., and Emri, I., 2013, "High Pressure Dissipative Granular Materials for Earthquake Protection of Houses," Anali Pazu, **3**(2), pp. 79–86.

[47] Barras, C., 2009, "Invisibility Cloak Could Hide Buildings from Quakes," New Sci.

[48] Brun, M., Guenneau, S., and Movchan, A. B., 2009, "Achieving Control of in-Plane Elastic Waves," Appl. Phys. Lett., **94**(6), p. 061903.

[49] Boechler, N., Theocharis, G., and Daraio, C., 2011, "Bifurcation-Based Acoustic Switching and Rectification," Nat. Mater., **10**(9), pp. 665–668.

[50] Li, F., Anzel, P., Yang, J., Kevrekidis, P. G., and Daraio, C., 2014, "Granular Acoustic Switches and Logic Elements," Nat. Commun., **5**, p. 5311.

[51] Pal, R. K., and Geubelle, P. H., 2014, "Wave Tailoring by Precompression in Confined Granular Systems," Phys. Rev. E, **90**(4), p. 042204.

[52] Pal, R. K., Waymel, R. F., Geubelle, P. H., and Lambros, J., 2017, "Tunable Wave Propagation in Granular Crystals by Altering Lattice Network Topology," J. Eng. Mater. Technol., **139**(1), p. 011005.

[53] Hasan, M. A., Cho, S., Remick, K., Vakakis, A. F., McFarland, D. M., and Kriven, W. M., 2015, "Experimental Study of Nonlinear Acoustic Bands and Propagating Breathers in Ordered Granular Media Embedded in Matrix," Granul. Matter, **17**(1), pp. 49–72.

[54] Spadoni, A., and Daraio, C., 2010, "Generation and Control of Sound Bullets with a Nonlinear Acoustic Lens," Proc. Natl. Acad. Sci., **107**(16), pp. 7230–7234.

[55] Li, K., and Rizzo, P., 2015, "Energy Harvesting Using Arrays of Granular Chains and Solid Rods," J. Appl. Phys., **117**(21), p. 215101.

[56] Yang, J., Silvestro, C., Sangiorgio, S. N., Borkowski, S. L., Ebramzadeh, E., Nardo, L. D., and Daraio, C., 2012, "Nondestructive Evaluation of Orthopaedic Implant Stability in THA Using Highly Nonlinear Solitary Waves," Smart Mater. Struct., **21**(1), p. 012002.

[57] Ni, X., Rizzo, P., Yang, J., Katri, D., and Daraio, C., 2012, "Monitoring the Hydration of Cement Using Highly Nonlinear Solitary Waves," NDT E Int., **52**, pp. 76–85.

[58] Kim, E., Restuccia, F., Yang, J., and Daraio, C., 2015, "Solitary Wave-Based Delamination Detection in Composite Plates Using a Combined Granular Crystal Sensor and Actuator," Smart Mater. Struct., **24**(12), p. 125004.

[59] Bagheri, A., La Malfa Ribolla, E., Rizzo, P., Al-Nazer, L., and Giambanco, G., 2015, “On the Use of L-Shaped Granular Chains for the Assessment of Thermal Stress in Slender Structures,” Exp. Mech., **55**(3), pp. 543–558.

[60] Leonard, A., Fraternali, F., and Daraio, C., 2011, “Directional Wave Propagation in a Highly Nonlinear Square Packing of Spheres,” Exp. Mech., **53**(3), pp. 327–337.

[61] Awasthi, A. P., Smith, K. J., Geubelle, P. H., and Lambros, J., 2012, “Propagation of Solitary Waves in 2D Granular Media: A Numerical Study,” Mech. Mater., **54**, pp. 100–112.

[62] Leonard, A., and Daraio, C., 2012, “Stress Wave Anisotropy in Centered Square Highly Nonlinear Granular Systems,” Phys. Rev. Lett., **108**(21).

[63] Leonard, A., Daraio, C., Awasthi, A., and Geubelle, P., 2012, “Effects of Weak Disorder on Stress-Wave Anisotropy in Centered Square Nonlinear Granular Crystals,” Phys. Rev. E, **86**(3).

[64] Szelengowicz, I., Kevrekidis, P. G., and Daraio, C., 2012, “Wave Propagation in Square Granular Crystals with Spherical Interstitial Intruders,” Phys. Rev. E, **86**(6).

[65] Szelengowicz, I., Hasan, M. A., Starosvetsky, Y., Vakakis, A., and Daraio, C., 2013, “Energy Equipartition in Two-Dimensional Granular Systems with Spherical Intruders,” Phys. Rev. E, **87**(3).

[66] Leonard, A., Chong, C., Kevrekidis, P. G., and Daraio, C., 2014, “Traveling Waves in 2D Hexagonal Granular Crystal Lattices,” Granul. Matter, **16**(4), pp. 531–542.

[67] Nishida, M., and Tanaka, Y., 2010, “DEM Simulations and Experiments for Projectile Impacting Two-Dimensional Particle Packings Including Dissimilar Material Layers,” Granul. Matter, **12**(4), pp. 357–368.

[68] Manjunath, M., Awasthi, A. P., and Geubelle, P. H., 2014, “Plane Wave Propagation in 2D and 3D Monodisperse Periodic Granular Media,” Granul. Matter, **16**(1), pp. 141–150.

[69] Coste, C., and Gilles, B., 2008, “Sound Propagation in a Constrained Lattice of Beads: High-Frequency Behavior and Dispersion Relation,” Phys. Rev. E, **77**(2), p. 021302.

[70] O’Donovan, J., O’Sullivan, C., and Marketos, G., 2012, “Two-Dimensional Discrete Element Modelling of Bender Element Tests on an Idealised Granular Material,” Granul. Matter, **14**(6), pp. 733–747.

[71] Marketos, G., and O’Sullivan, C., 2013, “A Micromechanics-Based Analytical Method for Wave Propagation through a Granular Material,” Soil Dyn. Earthq. Eng., **45**, pp. 25–34.

[72] Donahue, C. M., Anzel, P. W. J., Bonanomi, L., Keller, T. A., and Daraio, C., 2014, “Experimental Realization of a Nonlinear Acoustic Lens with a Tunable Focus,” Appl. Phys. Lett., **104**(1), p. 014103.

[73] Torrent, D., and Sanchez-Dehesa, J., 2007, “Acoustic Metamaterials for New Two-Dimensional Sonic Devices,” New J. Phys., **9**(9), p. 323.

[74] Sánchez-Dehesa, J., Torrent, D., and Cai, L.-W., 2009, “Acoustic Transparency in Two-Dimensional Sonic Crystals,” New J. Phys., **11**(1), p. 013039.

[75] Parnell, W. J., and Shearer, T., 2013, “Antiplane Elastic Wave Cloaking Using Metamaterials, Homogenization and Hyperelasticity,” Wave Motion, **50**(7), pp. 1140–1152.

[76] Wang, E., Geubelle, P., and Lambros, J., 2013, “An Experimental Study of the Dynamic Elasto-Plastic Contact Behavior of Metallic Granules,” J. Appl. Mech., **80**(2), p. 021009.

[77] Thornton, C., 1997, “Coefficient of Restitution for Collinear Collisions of Elasti-Perfectly Plastic Spheres,” J. Appl. Mech., **64**, pp. 383–386.

[78] Stevens, A. B., and Hrenya, C. M., 2005, "Comparison of Soft-Sphere Models to Measurements of Collision Properties during Normal Impacts," Powder Technol., **154**(2–3), pp. 99–109.

[79] Wang, E., On, T., and Lambros, J., 2013, "An Experimental Study of the Dynamic Elasto-Plastic Contact Behavior of Dimer Metallic Granules," Exp. Mech., **53**(5), pp. 883–892.

[80] Pal, R. K., Awasthi, A. P., and Geubelle, P. H., 2013, "Wave Propagation in Elasto-Plastic Granular Systems," Granul. Matter, **15**(6), pp. 747–758.

[81] Pal, R. K., Morton, J., Wang, E., Lambros, J., and Geubelle, P. H., 2015, "Impact Response of Elasto-Plastic Granular Chains Containing an Intruder Particle," J. Appl. Mech., **82**(1), p. 011002.

[82] On, T., LaVigne, P. A., and Lambros, J., 2014, "Development of Plastic Nonlinear Waves in One-Dimensional Ductile Granular Chains under Impact Loading," Mech. Mater., **68**, pp. 29–37.

[83] On, T., Wang, E., and Lambros, J., 2015, "Plastic Waves in One-Dimensional Heterogeneous Granular Chains under Impact Loading: Single Intruders and Dimer Chains," Int. J. Solids Struct., **62**, pp. 81–90.

[84] Burgoyne, H. A., and Daraio, C., 2014, "Strain-Rate-Dependent Model for the Dynamic Compression of Elastoplastic Spheres," Phys. Rev. E, **89**(3).

[85] Burgoyne, H. A., and Daraio, C., 2015, "Elastic–plastic Wave Propagation in Uniform and Periodic Granular Chains," J. Appl. Mech., **82**(8), p. 081002.

[86] Pal, R. K., and Geubelle, P. H., 2014, "Impact Response of Elasto-Plastic Granular and Continuum Media: A Comparative Study," Mech. Mater., **73**, pp. 38–50.

[87] Burgoyne, H. A., Newman, J. A., Jackson, W. C., and Daraio, C., 2015, "Guided Impact Mitigation in 2D and 3D Granular Crystals," Procedia Eng., **103**, pp. 52–59.

[88] Waymel, R. F., Wang, E., Awashti, A., Geubelle, P. H., and Lambros, J., 2017, "Propagation and Dissipation of Elasto-Plastic Stress Waves in Two-Dimensional Ordered Granular Media," J. Mech. Phys. Solids, In Press. https://doi.org/10.1016/j.jmps.2017.11.007

[89] Salazar de Troya, M., 2015, "Design Optimization for 2D Granular Media with Dissipation," M.S., University of Illinois at Urbana-Champaign.

[90] Wang, E., Manjunath, M., Awasthi, A. P., Pal, R. K., Geubelle, P. H., and Lambros, J., 2014, "High-Amplitude Elastic Solitary Wave Propagation in 1-D Granular Chains with Preconditioned Beads: Experiments and Theoretical Analysis," J. Mech. Phys. Solids, **72**, pp. 161–173.

[91] Shukla, A., and Dally, J. W., 2010, "Strain Gage Circuits and Instrumentation," *Experimental Solid Mechanics*, College House Enterprises, LLC, Knoxville, TN, pp. 195–229.

[92] Subhash, G., and Ravichandran, G., 2000, "Split Hopkinson Pressure Bar Testing of Ceramics," *ASM Handbook on Mechanical Testing and Evaluation*, ASM International, pp. 497–504.

[93] Nesterenko, V. F., Daraio, C., Herbold, E. B., and Jin, S., 2005, "Anomalous Wave Reflection at the Interface of Two Strongly Nonlinear Granular Media," Phys. Rev. Lett., **95**(15).

[94] Job, S., Melo, F., Sokolow, A., and Sen, S., 2005, "How Hertzian Solitary Waves Interact with Boundaries in a 1D Granular Medium," Phys. Rev. Lett., **94**(17).

[95] Daraio, C., and Nesterenko, V. F., 2006, “Strongly Nonlinear Wave Dynamics in a Chain of Polymer Coated Beads,” Phys. Rev. E, **73**(2).

[96] 1999, “Piezo Film Sensors Technical Manual,” Measurement Specialties. http://emerald.tufts.edu/programs/mma/emid/piezo.pdf

[97] 2011, “Introduction to Piezoelectricity,” Piezo Systems, Inc. http://www.piezo.com/tech2intropiezotrans.html

[98] Sirohi, J., and Chopra, I., 2000, “Fundamental Understanding of Piezoelectric Strain Sensors,” J. Intell. Mater. Syst. Struct., **11**(4), pp. 246–257.

[99] “Technical Resource Paper - An Overview of the Properties of Different Piezoceramic Materials,” Piezo Technologies. http://www.piezotechnologies.com/knowledge-desk/overview-piezo-materials

[100] Szelengowicz, I. M. N., 2013, *Analysis and Optimization of Stress Wave Propagation in Two-Dimensional Granular Crystals with Defects*, California Institute of Technology.

[101] Boechler, N. S., 2011, *Granular Crystals: Controlling Mechanical Energy with Nonlinearity and Discreteness*, California Institute of Technology.

[102] Khatri, D., 2012, *Non-Destructive Evaluation of Material System Using Highly Nonlinear Acoustic Waves*, California Institute of Technology.

[103] Manjunath, M., Awasthi, A. P., and Geubelle, P. H., 2014, “Family of Plane Solitary Waves in Dimer Granular Crystals,” Phys. Rev. E, **90**(3).

[104] Nemat-Nasser, S., Isaacs, J. B., and Starrett, 1991, “Hopkinson Techniques for Dynamic Recovery Experiments,” Proc. R. Soc. Lond. A, **435**, pp. 371–391.

[105] Plimpton, S., 1995, “Fast Parallel Algorithms for Short-Range Molecular Dynamics,” J. Comput. Phys., **117**, pp. 1–19.

[106] Shukla, A., Zhu, C. Y., and Sadd, M., 1988, “Angular Dependence of Dynamic Load Transfer due to Explosive Loading in Granular Aggregate Chains,” J. Strain Anal. Eng. Des., **23**(3), pp. 121–127.

[107] Zhu, C. Y., Shukla, A., and Sadd, M. H., 1991, “Prediction of Dynamic Contact Loads in Granular Assemblies,” J. Appl. Mech., **58**, pp. 341–346.

APPENDIX: PIEZOELECTRIC SENSOR PROPERTIES

Table A.1: Properties of the piezoceramic sensor used in the experiments

Equivalence (Other names for the same sensor)			SM412
			PZT-5A
			Navy Type II
Property	Unit	Symbol	
Electromechanical Coupling Coefficient	-----	K_p	0.63
		K_t	0.42
		K_{31}	0.35
Frequency Constant	Hz · m	N_p	2080
		N_t	2080
		N_{31}	1560
Piezoelectric Charge Constant	× 10^{-12} m/V (or C/N)	d_{33}	450
		d_{31}	-190
Piezoelectric Voltage Constant	× 10^{-3} Vm/N (or m^2/C)	g_{33}	25.6
		g_{31}	-12.6
Elastic Constant	× 10^{10} N/m^2	Y_{33}	5.6
		Y_{11}	7.6
Mechanical Quality Factor	-----	Q_m	100
Dielectric Constant	@ 1 kHz	$\varepsilon^{T_{33}} / \varepsilon_0$	1850
Dissipation Factor	% @ 1 kHz	$\tan\delta$	1.2
Curie Temperature	°C	T_c	320
Density	g/cm^3	ρ	7.8
Resonant Frequency	kHz	f_r	300 ± 10
Electromechanical Coupling Coefficient	%	K_p	$\geq 55\%$
Resonant Impedance	Ω	Z_m	$\leq 10\ \Omega$
Static Capacitance	pF @ 1 kHz	C_s	$3000 \pm 15\ \%$